# IMAGING THE MANTLE STRUCTURE OF THE EARTH AND MOON FROM ARRAY BASED OBSERVATIONS

by

Yao Yao

A dissertation submitted to the faculty of
The University of Utah
in partial fulfillment of the requirements for the degree of

Doctor of Philosophy

in

Geophysics

Department of Geology and Geophysics

The University of Utah

August 2016

**The University of Utah Graduate School**

# STATEMENT OF DISSERTATION APPROVAL

The dissertation of **Yao Yao**

has been approved by the following supervisory committee members:

| | | |
|---|---|---|
| **Michael S. Thorne** | , Chair | **05/11/2016** Date Approved |
| **Lowell Masataka Miyagi** | , Member | **04/29/2016** Date Approved |
| **Keith David Koper** | , Member | **04/29/2016** Date Approved |
| **Fan-Chi Lin** | , Member | **04/29/2016** Date Approved |
| **Nicholas Schmerr** | , Member | **05/26/2016** Date Approved |

and by **John Bartley**, Chair/Dean of

the Department/College/School of **Geology and Geophysics**

and by David B. Kieda, Dean of The Graduate School.

# ABSTRACT

Studying the seismic structure of the interior of planets provides fundamental insights into the thermal and chemical evolution of the planets. The Moon is thus far the only terrestrial body outside of the Earth that humans have deployed a network of seismometers on to study the interior structure. Moonquakes are dominated by long-duration seismic coda due to its highly scattered and low-attenuation interior. To understand the origins of these coda waves and the behavior of seismic waves propagating in a highly scattered media such as on the Moon, we generate synthetic seismograms based on models with randomly distributed small scale inhomogeneities using 2.5-D axi-symmetric finite difference algorithm SHaxi. The smoothed envelope functions of the synthetic seismograms are used to compare with the observations to investigate the features of the scattering layer. Our results indicate a crustal scattering layer is crucial to the long duration risetime and coda of moonquakes, but is not sufficient to create the observed long risetime and coda.

An unprecedented densification of seismic stations in North America has recently been accomplished through deployment of the USArray. Using this newly available data set we investigate the velocity structure of the D" discontinuity beneath North Atlantic Ocean (45-60° N, 45-55° W) by applying fourth root Vespa processing to transverse and radial component recordings from the 2010 M6.3 southern Spain earthquake (depth=620 km) recorded on 370 broadband stations in North America. These observations are best fit with a +2-4% $S$-wave velocity increase at the top of the D" discontinuity at a height above the core-mantle boundary of 304 ± 14 km. We do not observe *Scd* arrivals at the eastern end of our study region which is consistent with the presence of the easternmost edge of the ancient Farallon plate. To further investigate large scale velocity heterogeneities in the lower mantle, we calculate the slowness from high signal-to-noise teleseismic $P$- and $S$-wave arrivals from earthquakes between January 2004 and June 2015 recorded by broadband seismic

stations in North America. We identify slowness anomalies with a lower mantle origin beneath the North Pacific (45° N $\sim$ 70° N, 135° W $\sim$ 160° W). The slowness anomalies indicate a gradationally changing low-velocity layer located from 1100 km depth to at least 2000 km, with a potential origin of the iron spin transition. Accurate mantle corrections based on higher resolution tomography models will be beneficial to future deep earth studies.

To Chaoxun Hang

# CONTENTS

# ACKNOWLEDGMENTS

I would like to express my greatest gratitude to my graduate advisor, Michael Thorne, for his continuous support and guidance in my research. He trained me step-by-step over the years, prompted me to learn, think, and explore independently as a scientist. His creative in-depth opinions of seismology studies have always changed my perspective on my own research. His passion for presenting seismic data in the most pleasant style has led me into scientific visualization. My sincere thanks to you for making my research work into a very pleasant process, for passing me your knowledge unselfishly, and for being so patient with my writing.

Thanks to my supervisory committee Keith Koper, Lowell Miyagi, FanChi Lin, and Nick Schmerr for their support and the numerous scientific and nonscientific discussions over the years. I thank Keith Koper for his career advice, American culture tips, and for always sharing his knowledge of the newest development in my research area with me. I thank Lowell Miyagi for being such a reliable source of knowledge in mineral physics. He is the one who navigated me through the sea of research papers to find the most important ones I need to read first. I owe thanks to FanChi Lin, for being insightful on some hidden problems of my research and for providing valuable help and ideas. I also thank Nick Schmerr for sharing his codes with me kindly and in a timely manner. The colorful ribbons he shared with me every year during the AGU conferences really added some joy to those intense weeks.

I would like to give thanks to the many people at University of Utah and University of Utah Seismograph Stations, including teachers, students, and staff, who made my five years in the U.S. enjoyable and full of excitement. Special thanks to Kristine Pankow and James C.Pechmann, who helped calm me down when I encountered a dead end in my research, and shared their experience of digging out. Thanks to Hsin-Hua Huang for sharing his travel time correction codes with me. It provided a light in the darkest days of my research. Thanks to J. Mark Hale for reminding

me of the expectations for a Ph.D candidate when I was feeling helpless. Thanks to Chase Batchelor and Brendon Quirk for being wonderful office mates with me. I will miss the windows and the cheerful conversations. Thanks to Lisa Linville for always feeding me with delicious snacks, bringing the cutest dog in the world to our office, and letting me join her workout group. Thanks to Jamie Farrell for helping me practice my defense. Special thanks go to Rule Burlac and Amir Allam, for offering their help so kindly and helping me correct my dissertation. Thanks Yue Zhu and Runfeng Liu for taking care of my cats while I was traveling. Special thanks to Oner Sufri, who provided countless helps during my first two years of graduate school. The job hunting tips and the experience he shared with me were of tremendous help. My sincere gratitude goes to Stefanie Whittaker, for helping me track down my advisor, for being sharp and honest when answering questions when I did not want comfortable answers, and for always being supportive and encouraging.

Finally I would like to give thanks to my parents for their continuous support and encouragement through my life. I would also like to acknowledge Chaoxun Hang, for his decision to transfer to Salt Lake City and end the long distance between us, for his countless efforts to help me settle down in a new country, and for his intense support of everything I do.

# CHAPTER 1

# INTRODUCTION

The Earth formed about 4.54 billion years ago by accretion from the solar nebula, which is made of remnant interstellar dust and gas after the formation of the proto-Sun [*Jacobsen*, 2003]. A leading hypothesis for the origin of the moon is that it formed from a giant impact between a Mars-size body and the proto-Earth about 30 million years after the formation of the Earth [e.g., *Canup and Asphaug*, 2001; *Touboul et al.*, 2007; *Young et al.*, 2016]. It is hypothesized that the high energy Moon-forming event led to large-scale melting in both the Earth's and Moon's mantle, which is referred as the "magma ocean" hypothesis. The first observational evidence of this hypothesis came from Lunar soil samples returned by the Apollo missions. The analysis of these samples indicated large-scale differentiation of the Moon, which has been interpreted as being due to the crystallization of the lunar magma ocean [*Wood*, 1975; *Warren*, 1985]. The giant impact may have also caused extensive melting and possible magma ocean formation on the Earth [*Tonks and Melosh*, 1993; *Solomatov*, 2007]. Crystallization and differentiation of the Earth's magma ocean may have also led to compositional discontinuities and heterogeneities in the Earth's mantle [*Labrosse et al.*, 2007; *Lee et al.*, 2010]. Studying the seismic structure of the Earth's and Moon's mantles provides important insights into the composition and geophysical processes at work in the mantle, and further provides constraint on the processes involved in the formation of both solar system objects.

## 1.1 Structure and Dynamics of the Earth's Lower Mantle

The first travel time table was proposed by Jeffreys and Bullen in 1939, which was subsequently used as the first 1-D global seismic velocity model [*Jeffreys and Bullen*, 1958]. As the availability of data from increasing numbers of seismic stations

increased, several refinements to 1-D global seismic models have been made, such as the Preliminary Reference Earth Model (PREM) [*Dziewonski and Anderson*, 1981], IASP91 [*Kennett and Engdahl*, 1991], and AK135 [*Kennett et al.*, 1995]. Primary features of these 1-D models are the globally observed seismic discontinuities including crust-mantle boundary, transition zone discontinuities located in the vicinity of 410 km and 660 km depth, core-mantle boundary, and inner-outer core boundary. These seismic discontinuities are caused by either compositional changes, phase transitions, or rheological changes. Significant efforts in Earth structure studies have been and are still devoted to investigating the velocity structures and the origins of these discontinuities.

However, variation in the structure of the Earth is beyond what is predicted by the average 1-D models. For example, large-scale (500 $\sim$ 1000 km) and small-scale (50 $\sim$ 500 km) lateral variations of the seismic velocities are observed, particularly in the upper mantle and lowermost mantle region referred as D". In the region between the 660 km discontinuity and the core mantle boundary, no global seismic discontinuity has been observed thus far. However, several important seismic heterogeneities such as Large Low Shear Velocity Provinces (LLSVPs), Ultra Low-Velocity Zones (ULVZs), and the D" discontinuity have been demonstrated to exist in the lowermost mantle since the 1980s. A schematic illustration of these heterogeneities is shown in Figure 1.1.

LLSVPs were initially imaged by seismic tomography models [*Li and Romanowicz*, 1996; *Su and Dziewonski*, 1997; *Ritsema et al.*, 2011]. This velocity heterogeneity is described by a roughly -3% to -5% shear wave reduction compared to PREM [*He and Wen*, 2009], with extensive coverage of the core-mantle boundary (CMB) region ($\sim$21% of the CMB surface area) [*Burke et al.*, 2008] and extended height above the CMB (at least $\sim$1000 km). Seismic observations have revealed one LLSVP beneath the central Pacific Ocean and a second beneath Africa. The origins and dynamics of LLSVPs are closely related to the Earth's large scale convective processes, yet the exact nature of these features still remains in question, with different scenarios favoring plume clusters [*Schubert et al.*, 2004], superplumes [e.g., *Su et al.*, 1994; *Davaille and Vatteville*, 2005], or piles [*Tan and Gurnis*, 2005].

Compared to the large scale anomalies of LLSVPs, ULVZs appear to be much smaller scale (on the order of 10's to 100's of km in lateral dimensions). ULVZs are velocity heterogeneities with heights of roughly 5-40 km above the CMB with $P$- and $S$-wave velocity reduction potentially as large as 24% and 45% [*Thorne et al.*, 2013; *Brown et al.*, 2015], respectively. Past studies have made links between ULVZs and hot spot volcanism [*Williams et al.*, 1998], and one recent study has shown the existence of especially large ULVZs directly beneath prominent hot spot volcanoes such as Hawaii, Iceland, and Samoa, indicating the ULVZs and hot spots may be linked by whole mantle plumes [*French and Romanowicz*, 2015]. The additional observation that ULVZs are often found near the edges of LLSVPs also provides insight into the origin of ULVZs with a potential link to whole mantle plumes [*McNamara et al.*, 2010]. Nevertheless, what ULVZs physically represent is still uncertain with some studies indicating a partial melt origin of ULVZs [*Rost et al.*, 2005], which could be caused by the fractional crystallization of primordial magma ocean [*Labrosse et al.*, 2007]. Yet a compositional origin of ULVZs is also possible [*Wicks et al.*, 2010; *Brown et al.*, 2015].

Besides ULVZs, seismic observations have also shown unequivocal evidence for a velocity discontinuity located on the mantle side of the core mantle boundary, referred as the D" discontinuity. Most of the observations indicate the height of the D" discontinuity is about 200 to 300 km above the CMB with -3% to +3% $P$- wave velocity perturbation and +1% to 3% $S$-wave velocity increase at the discontinuity. The origin of the D" discontinuity is often attributed to the phase transition from perovskite (pv) to post-perovskite (ppv) [e.g., *Murakami et al.*, 2004; *Oganov and Ono*, 2004]. Observations of the D" discontinuity have primarily been constrained to regions where deep earthquakes and receivers are separated by roughly 60° to 85° in epicentral distance in order to take advantage of triplicated seismic arrivals associated with the discontinuity [e.g., *Cobden and Thomas*, 2013]. As a result, the existence of the discontinuity has mostly been demonstrated beneath North Central Asia [e.g., *Kendall and Shearer*, 1994], Alaska and the Bering Sea [e.g., *Young and Lay*, 1990], the Arctic [e.g., *Weber and Davis*, 1990], and Central America [e.g., *Lay and Helmberger*, 1983]. However, its existence in low velocity areas, such as inside

the Pacific LLSVP, has also been demonstrated [*Avants et al.*, 2006; *Lay et al.*, 2006]. Recent efforts have adopted more sophisticated methods such as the Generalized Radon Transform (GRT) [*Wang et al.*, 2008] and noise correlation techniques [*Poli et al.*, 2015] which offer promise for expanding the areas where the discontinuity may be searched for.

Understanding the nature of these thermochemical structures and their dynamics can reveal important information about the style of mantle convection, as well as the thermal and dynamic history of the Earth's evolution. However, many distinct challenges confront efforts to image these heterogeneities in the deep Earth. First, the resolution of seismic waves diminishes as a result of increasing wavelength of the seismic wave and reduced ray-path spatial sampling of the medium of interest as the seismic waves travel deeper. Second, deep mantle studies typically use deep earthquakes to lessen the contamination of the seismic waves with upper mantle and crustal structure, as well as stations with large spatial separations which can cover relatively large regions in the deep Earth to study the velocity variations. However, earthquake locations are limited and are concentrated close to plate boundaries. There are also significant limitations on station locations because most of the stations are land-based and the development of ocean bottom seismometers is still in its early stage. Finally, seismic phases generated by interesting structures in the deep earth normally have low signal-to-noise ratio because of the low impedance of the deep mantle velocity heterogeneities.

Despite these limitations, recent expansion of seismic arrays and development of computational capabilities have resulted in increased use of more sophisticated data processing methodologies in deep earth studies. In Chapter 2, we apply array processing techniques to seismic data recorded by the USArray to investigate the structure of the D" discontinuity beneath the North Atlantic. We apply fourth root Vespa processing to enhance the low-amplitude *Scd* arrivals from transverse and radial component recordings from the 2010 M6.3 southern Spain earthquake (depth=620 km) recorded on 370 broadband stations in North America. Our observations are best fit with a +2-4% *S*-wave velocity increase at the top of the D" discontinuity at a height of 304 $\pm$ 14 km above the core-mantle boundary. The D" discontinuity is

present at the eastern end of our study region which is consistent with the presence of the easternmost edge of the ancient Farallon plate. This work was published in *Geophysical Research Letters* in 2015. In Chapter 3, we take advantage of the large amount of seismic data recorded by broadband seismic stations in North America to investigate the distribution of large-scale lower mantle velocity heterogeneities beneath the North Pacific. We calculate slowness from high signal-to-noise teleseismic $P$- and $S$-wave arrivals from earthquakes between January 2004 and June 2015 located along the North and West Pacific Rim. We are able to identify low velocity heterogeneities located from 1100 km to 2000 km beneath the North Pacific with maximum of -2% to -4% $P$- and $S$-wave velocity reduction. The origin of this heterogeneity may be related to the iron spin transition in the mantle.

## 1.2 Structure of the Lunar Mantle

Our current view and understanding of the lunar interior have been shaped to a large extent from the knowledge and data acquired from the Apollo mission. From 1969 to 1977, a network of four seismic stations was established and operated on the Moon as a part of the Apollo Lunar Surface Experiments Package (ALSEP) [*Latham et al.*, 1969]. As a part of ALSEP, the Passive Seismic Experiment (PSE) was designed to detect moonquakes to determine the structure of the Moon. Over 13,000 moonquakes have been identified through the 8 years of deployment. These data have been used to invert for a variety of 1-D seismic velocity models of the Moon [*Nakamura et al.*, 1976; *Goins et al.*, 1981; *Nakamura*, 1983; *Khan and Mosegaard*, 2002; *Lognonnè et al.*, 2003; *Gagnepain-Beyneix et al.*, 2006; *Garcia et al.*, 2011]. Because of the presence of long duration coda on the lunar seismograms, it is challenging to identify any deep reflected seismic phases, and thus determine the structure of the lunar interior. Whether or not deep mantle discontinuities exist on the Moon is still debated although some efforts have put forth evidence of mantle and deep mantle layering [*Nakamura*, 1983; *Garcia et al.*, 2011; *Weber et al.*, 2011].

Despite the challenges inherent in deciphering the mantle discontinuities based on our current dataset, the characteristic long coda observed from the lunar seismograms can still provide insights into the small scale velocity variations of the lunar interior.

In Chapter 4, we first introduce synthetic seismograms for simplified versions of the lunar interior and describe the seismic phases that are observed in these models. Then we introduce a series of models that include random seismic velocity perturbations in the lunar crust and mantle in order to assess the effect of incorporating scattering into the simulations. A schematic illustration of the scattering media in the lunar mantle is shown in Figure 1.2. The nature of the scattering effect of the lunar seismic waves is closely related to formation and evolution in the lunar history.

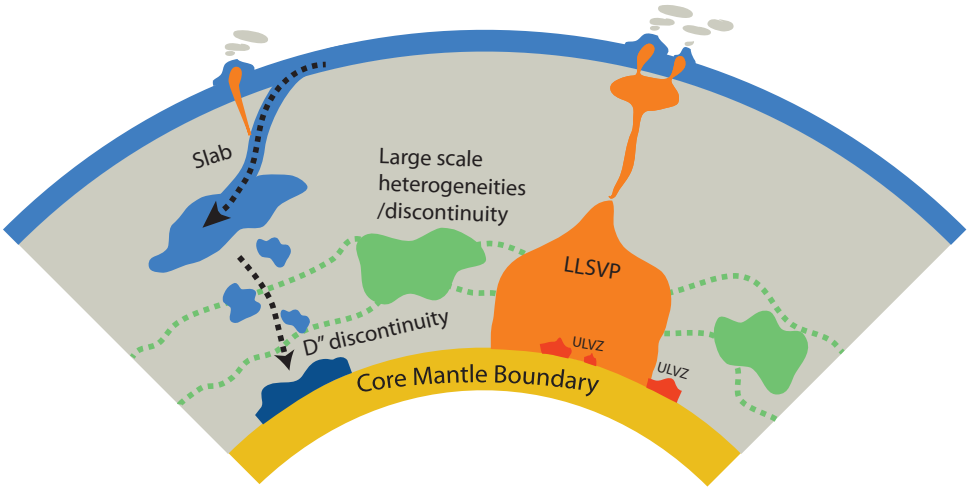


**Figure 1.1**. Schemetic illustration of the lower mantle heterogeneties in the Earth.

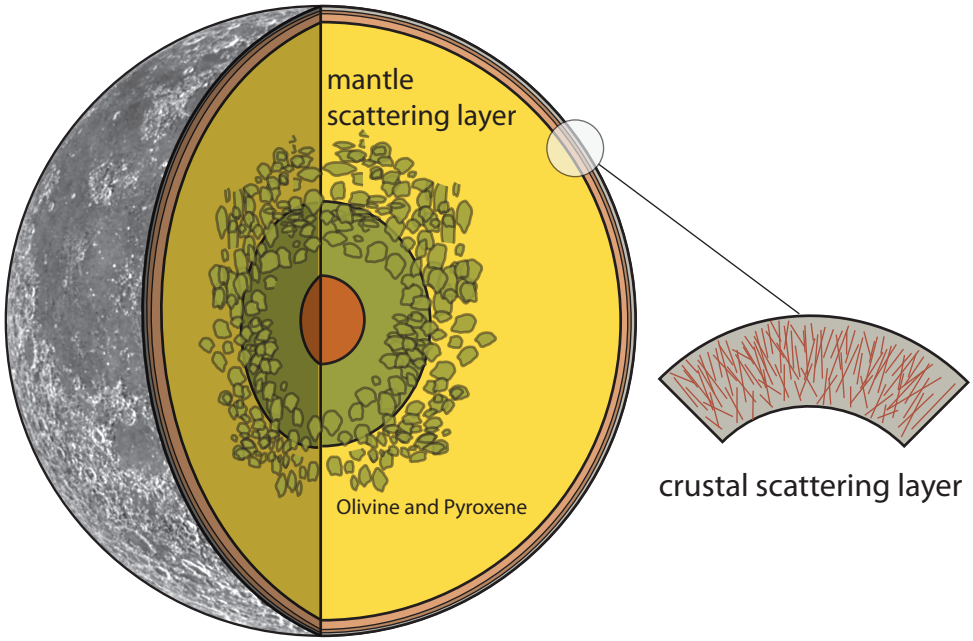


**Figure 1.2**. Schemetic illustration of the scattering media in the lunar mantle.

# CHAPTER 2

# THE D" DISCONTINUITY STRUCTURE BENEATH THE NORTH ATLANTIC FROM *SCD* OBSERVATIONS

## 2.1 Abstract

We analyzed transverse and radial component recordings from the 2010 M6.3 southern Spain earthquake (depth = 620 km) recorded on 370 broadband stations in North America. We grouped these seismograms into subarrays and applied 4th root Vespa processing (vespagram analysis) in order to enhance low amplitude arrivals. These vespagrams show clear *Scd* arrivals which indicate the existence of the D" discontinuity beneath the North Atlantic Ocean (45-60° N, 45-55° W). These observations are best fit with a +2-4% velocity increase at the top of the D" discontinuity at a height above the core-mantle boundary of 304 ± 14 km. We do not observe *Scd* arrivals at the eastern end of our study region which is consistent with the presence of the easternmost edge of the ancient Farallon plate.

## 2.2 Introduction

The D" discontinuity is a sharp change in *P*- and *S*-wave velocity of roughly -3 to +3% and +1 to +3% respectively ranging from about 100 - 400 km above the core-mantle boundary (CMB). A phase transition from perovskite (pv) to post-perovskite (ppv) at pressures and temperatures where the discontinuity is observed is a leading candidate for its origin [e.g., *Murakami et al.*, 2004; *Oganov and Ono*, 2004]. Nonetheless, some observations of the discontinuity are difficult to reconcile with a simple phase transition; a situation that is further complicated by lateral variations in lower mantle composition [see *Cobden and Thomas*, 2013, for a review]. In order to

understand the origins of the D" discontinuity, it is important to understand where it exists and what its physical properties are.

Only a handful of observations have been made beneath the North Atlantic (Figure 2.1a). *Weber and Körnig* [1992] first suggested the possibility of a lower mantle reflector beneath the North Atlantic ridge (labeled 1 in Figure 2.1a) with a height above the CMB of roughly 200 to 250 km by identifying secondary arrivals between $P$ and $PcP$. Several additional studies have provided evidence for D" discontinuity structure with $P$-waves (*Houard and Nataf*, 1992; *Krüger et al.*, 1995; *Braña and Helffrich*, 2004; labeled 2, 4, and 5, respectively in Figure 2.1a). Evidence for a $S$-wave discontinuity was first demonstrated by *Kendall and Shearer* [1994]. They estimated a D" height of 250 km above the CMB (labeled 3 in Figure 2.1a), yet their study was limited to a relatively small number ($< 10$) of seismograms. More recently, *Wallace and Thomas* [2005] showed a laterally varying D" discontinuity associated with a 1-3% $S$-wave velocity increase with heights ranging from 86 to 286 km above the CMB (labeled 6 in Figure 2.1a). However, this study did not unambiguously confirm the existence of triplicated $S$-wave arrivals.

In this chapter, we investigate the D" discontinuity beneath the North Atlantic Ocean using $S$-wave observations from the 2010 M6.3 southern Spain earthquake recorded on broadband stations in North America. We use a significantly larger dataset (370 seismograms for which we use both radial and transverse components) than used in previous studies, which allows us to sort our records into virtual arrays and apply array processing approaches to search for triplicated seismic arrivals in both transverse and radial component recordings. We demonstrate the existence of the discontinuity in a region of the North Atlantic (45 - 60° N, 45 - 55° W) that has not previously been investigated.

## 2.3 Data and Methods

We investigate D" discontinuity structure by searching for the *Scd* seismic phase on both transverse and radial component data. *Scd* is a part of the triplication that occurs as the down-going $S$-wave refracts below the D" discontinuity (Figure 2.2a-b). Example synthetic seismograms for transverse and radial components are shown in

Figures 2.2e and 2.2f, respectively. These synthetics were computed for a 620 km deep source and a D" discontinuity model with a 2% increase in $S$-wave velocity 250 km above the CMB. There is no change in density and for radial component synthetics we included an additional 1% increase in $P$-wave velocity. On the transverse component (Figure 2.2e) *Scd* is observed as a low-amplitude, positive polarity arrival, between the $S$ and *ScS* phases. The $Scd/S$ amplitude ratio increases with increasing epicentral distance. On the radial component (Figure 2.2f) the *Scd* phase may be obscured by the *SKS* arrival and possibly the *SP* arrival (Figure 2.2b) at the shortest epicentral distances.

We searched for earthquakes in the European region between January 2005 and June 2014 with Mw between 5.5 and 7.5, event depths greater than 75 km, recorded at broadband stations in North America within an epicentral distance window of 55° to 90°. For each record we removed the mean and trend, deconvolved the instrument response, and band-pass filtered the traces from 0.05 to 1 Hz. A total of five earthquakes with 2077 seismograms were originally collected. We inspected each transverse component trace manually and removed traces without detectable $S$ and *ScS* arrivals. This quality control step cut our data set down to 4 events with 833 seismograms.

For each event, we grouped our data into 3° radius geographic bins based on receiver location in order to apply array processing techniques on each subgroup of data. We restricted our bins to just those that contained a minimum of 10 traces, then aligned and normalized each trace to unity on the $S$-wave arrival. We applied 4th root Vespa processing [*Rost and Thomas*, 2009] on each subarray. Example vespagrams with labeled seismic phases for transverse and radial component synthetic seismograms are shown in Figures 2.2c and 2.2d, respectively. On the transverse component, the *Scd* arrival is readily observed with a slowness and travel time in-between $S$ and *ScS*. On the radial component, the *Scd* arrival is weaker in amplitude than on the transverse component and may potentially be obscured by the *SKS* arrival. Although, *SKS* arrives at a smaller slowness than *Scd*, the slowness resolution of real data is often much poorer than shown for synthetic seismograms. We next screened vespagrams based on signal-to-noise ratio and slowness resolution of $S$ and

*ScS*. If the *S* and *ScS* arrivals are clearly present in the vespagram with significantly larger amplitude than the background noise, and the energy of the *S* and *ScS* arrivals are relatively concentrated (the slowness resolution is less than 5 s/°), we retain the vespagram. Among these vespagrams we ultimately discarded the vespagrams for three of the events because either the event was too shallow and the *sS* arrival obscured potential *Scd* arrivals, or the *S* and *ScS* arrivals were too close together to unambiguously observe an *Scd* arrival. Only vespagrams from the 620 km deep M6.3 southern Spain event of 11 April 2010 were retained for further analysis. Our final data set consisted of 370 seismograms and 31 vespagrams (recorded on each component). In each vespagram we searched for the presence of the *Scd* arrival, and if it existed, we recorded the differential travel-times ($\delta T_{Scd-S}$ and $\delta T_{ScS-Scd}$) and differential slownesses ($\delta u_{Scd-S}$ and $\delta u_{ScS-Scd}$).

In order to model D" discontinuity characteristics we compared data recordings and vespagrams to synthetic seismograms and synthetic vespagrams. We calculated synthetic seismograms using the reflectivity technique [*Fuchs and Müller*, 1971], SHaxi [*Jahnke et al.*, 2008] and PSVaxi [*Thorne et al.*, 2013] methods. We generated synthetic seismograms based on three types of models which varied in the structure of their velocity profiles (Figure 2.3) using the Preliminary Reference Earth Model (PREM) as the background [*Dziewonski and Anderson*, 1981]. In total we computed synthetic seismograms for 58 unique models and the set of models are shown in Table 2.1. We used a sharp velocity contrast at the top of the discontinuity in our models, as gradational boundaries with thicknesses less than 100 km do not strongly affect our results (Figure 2.4).

We applied the same Vespa process to each of the synthetic traces as performed on the data traces. We picked the same differential travel-times and slownesses from the synthetic vespagrams as with the data. In order to determine the velocity profile of the D" discontinuity we compared data and synthetic predictions by minimizing the travel time and slowness misfits based on the following equations:

$$\delta T = \sqrt{\left(\frac{\delta T^{synth}_{Scd-S} - \delta T^{obs}_{Scd-S}}{\delta T^{obs}_{Scd-S}}\right)^2 + \left(\frac{\delta T^{synth}_{ScS-Scd} - \delta T^{obs}_{ScS-Scd}}{\delta T^{obs}_{ScS-Scd}}\right)^2} \tag{2.1}$$

$$\delta u = \sqrt{(\frac{\delta u^{synth}_{Scd-S} - \delta u^{obs}_{Scd-S}}{\delta u^{obs}_{Scd-S}})^2 + (\frac{\delta u^{synth}_{ScS-Scd} - \delta u^{obs}_{ScS-Scd}}{\delta u^{obs}_{ScS-Scd}})^2} \tag{2.2}$$

where $\delta T$ and $\delta u$ are the travel time and slowness misfits, respectively. We applied equal weights to both the travel time and slowness misfit, and calculated the final misfit as:

$$misfit = \frac{\delta T + \delta u}{2} \tag{2.3}$$

Mid-mantle seismic wave speed heterogeneity could bias our results if we do not have stable *ScS-S* differential travel-times across our study region. We computed synthetics for cross-sections through tomography model TXBW [*Grand*, 2002] and found small travel time variations (0.54 s average) across our study area. Thus we do not perform tomography based travel time corrections to these data (Figures 2.5, 2.6, and 2.7).

## 2.4 Results

*Scd* arrivals indicative of the D" discontinuity were identified on 20 of the 31 transverse component vespagrams. The remaining 11 vespagrams did not show evidence of an *Scd* arrival. Of the 20 vespagrams where we positively identified *Scd* arrivals, we further categorized these observations as either good cases (12) or borderline cases (8). We ranked the vespagram as good if the *Scd* arrival was clearly present and had a larger amplitude than the background noise, and the energy of the *Scd* arrival was relatively concentrated (the slowness resolution is $\leq 5$ s/°). Otherwise, if the potential *Scd* arrival had an amplitude similar to the background noise, and/or the slowness resolution was $\geq 5$ s/°, we ranked it as a borderline case. The locations of the central *ScS* bounce-points on the CMB for each bin based on the characterization of good, borderline, or no-*Scd* arrival are shown in Figure 2.1a-b. We were unable to clearly identify an *Scd* arrival on any of the radial component vespagrams.

Figure 2.8a-d shows example vespagrams and record sections for both the transverse and radial components of a good case (central bounce-point labeled I06 in Figure 2.1b). We see a *Scd* arrival located in between the *S* and *ScS* arrivals on both vespagram and record section of the transverse component, while no *Scd* arrival is definitively observed on the radial component. Nonetheless, there is some smearing

of the *SKS* arrival on the radial component vespagram that may interfere with a possible *Scd* arrival. Thus, we cannot rule out an *Scd* arrival in this case.

In order to estimate the velocity profile of the D" discontinuity, we computed synthetic vespagrams and calculated the misfit between observations and synthetics (Figure 2.9). Different synthetic model types that share the same discontinuity thickness naturally form into clusters sharing similar misfits (Figure 2.10, 2.11), suggesting that the model misfits are more sensitive to the depth variation of the D" discontinuity than model type or magnitude of the $S$-wave velocity increase at the top of the discontinuity, which is also demonstrated in *Wallace and Thomas* [2005]. Our results indicate a D" discontinuity located 225 to 350 km above the CMB with an average height of 304 $\pm$ 14 km ($\sigma$ = 48 km) above the CMB. The $S$-wave velocity contrast is more difficult to constrain, but our results are consistent with a +2% to +4% velocity increase at the top of the discontinuity. We obtain best fits for models that have a negative velocity gradient starting 200 km above the discontinuity and a negative velocity gradient below the discontinuity that ends at 1.0% above PREM at the CMB. Synthetic seismograms for the best-fit model (model 57, velocity profile shown in Figure 2.12) for bin I06 are shown in Figures 2.8b and 2.8d, and demonstrate the high coherence between the predictions and observations. The slightly lower amplitudes of $S$ and *ScS* arrivals in synthetics are due to the fixed radiation pattern in the SHaxi and PSVaxi algorithms. The increase in $S$-wave velocity at the top of the discontinuity is consistent with global observations and the negative velocity gradients above and below the D" discontinuity has been suggested by multiple previous studies [e.g., *Wysession et al.*, 1998; *Wallace and Thomas*, 2005]. The observed discontinuity height varies on sub-Fresnel zone (Fresnel zone radius is approximately between 5°and 10°) length scales which has also been noted in previous studies [*Kendall and Shearer*, 1994]. In our study, the negative velocity gradient above the discontinuity is necessary to provide the proper *Scd* travel time delay while still matching the *Scd* slowness.

The 12 good observations can be grouped into 2 clusters based on their spatial locations. Cluster A is centered at 54° N, 50° W with 5 bins (F01, F02, F03, G02, G03) and cluster B is centered at 47° N, 42° W with 7 bins (H06, I05, I06, I07,

J05, J06, J07) (Figure 2.1b). The observations in cluster A are concentrated in a small, 2° × 2° region while the observations in cluster B cover a larger 5° × 5° area. The velocity increases at the top of the discontinuity for both clusters are identical, ranging from +2% to +4%. Our discontinuity height estimates also suggest the depth distribution is similar in cluster A ($\sigma$=45 km) and cluster B ($\sigma$=52 km). In cluster A, the height estimation from the 5 bins show the D" discontinuity is likely located 275 to 325 km above the CMB with an average height of 295 ± 20 km. Only the observation at bin F03 shows a much deeper depth (225 km) of the discontinuity, yet it should be noted that this bin has relatively poor slowness resolution. If we were to remove bin F03 from the calculation, the average height increases to 312 km for cluster A. In cluster B, the height estimations of the northeastern bins (I05, I06, H06, J05, J06) are similar to the bins in cluster A, ranging from 325 to 350 km with a slightly greater average of 340 ± 6 km, while the depth to the D" discontinuity trends deeper to the southwest. The height estimations of the bin I07 and J07 located at the southwestern corner of the cluster B shows the D" discontinuity located 225 to 250 km above the CMB (Table 2.2). Our combined average of discontinuity height for cluster B is 310 ± 20 km.

The majority of our nonobservations are concentrated at the east edge of our study region (Figure 2.1b). In cluster A, the locations of the borderline cases fill in the gap between the good and non observation cases, with a thinner average height of 231 ± 28 km compared with good cases (295 ± 20 km). While in cluster B, the borderline cases have an average height of 250 ± 58 km as well but are located at the west boundary of our study area. The geographic correlation among the different types of observations (good, borderline, or non) may be explained by either: (1) differences in source-receiver distance of the observations, or (2) relationship to lower mantle structure. We explore these possibilities in the next section.

## 2.5 Discussion and Conclusions

No clear *Scd* arrivals were observed on these radial component data. Constructive and destructive interference effects from the *SKS* arrival may mask possible *Scd* arrivals, but previous studies have also speculated that transverse isotropy in the

D" layer may explain the lack of *Scd* observations on the radial component [e.g., *Matzel et al.*, 1996]. *Scd* arrivals on the radial component data may be present but it is difficult to confirm. There is a possible positive amplitude arrival that merges with the *SKS* leading downswing (Figure 2.8d). This arrival also appears separate from *SKS* on the vespagram (Figure 2.8b). However, if this is *Scd* on the radial component it arrives with slightly later arrival time and smaller slowness than *Scd* on the transverse component. A later *Scd* arrival on the radial component is consistent with anisotropy in post-perovskite where SH- is predicted to be faster than SV-waves [*Miyagi et al.*, 2010]. One previous study has demonstrated weak, or no anisotropy immediately south of our study area [*Garnero et al.*, 2004]. But, increased strain possibly induced by the subducting Farallon plate, as discussed below, could locally increase anisotropy in our study region which will be heavily dependent on lower mantle flow direction [e.g., *Moore et al.*, 2004; *Thomas et al.*, 2011].

Our estimate of D" discontinuity height above the CMB (average = 304 ± 14 km, ranging from 225 to 350 km) is similar but slightly greater to estimates from previous studies in the surrounding region (ranging from 200 to 286 km; Figure 2.1a). Our study area is located in a region where ancient subduction of the Farallon plate has been inferred [e.g., *Bunge and Grand*, 2000; *Conrad et al.*, 2004]. Previous $S$-wave tomography studies [e.g., *Mégnin and Romanowicz*, 2000; *Grand*, 2002; *Simmons et al.*, 2010; *Ritsema et al.*, 2011] also show that our study area is located at a boundary between fast and slow velocity regions at the CMB (Figure 2.1b), which could be the boundary between ancient Farallon plate and normal mantle. Therefore, the cold down-welling mantle, combined with an increase in mid-ocean ridge basalt composition of the Farallon plate could cause the discontinuity beneath our study region to occur at a greater height above the CMB [e.g., *Grocholski et al.*, 2012]. For cluster A, both our good and borderline observations are located within the fast $S$-wave velocity region, while most of our nonobservations are concentrated at the eastern edge of our study region closest to the slow $S$-wave velocities. Hence, our observations may be consistent with sampling the easternmost edge of the ancient Farallon plate.

Yet, our observations are potentially biased due to source-receiver epicentral distance. In general, the amplitude of the *Scd* arrival decreases with decreasing epicentral distance, which may lead to decreased detectability of the *Scd* arrivals. The epicentral distance range for our nonobservations ($\mathbf{\Delta}$=64°- 73°), borderline observations ($\mathbf{\Delta}$=68°- 74°), and good observations ($\mathbf{\Delta}$=70°- 76°) for cluster A tends to increase. The predicted $Scd/S$ amplitude ratio for a 1-D D" discontinuity model 300 km above the CMB with an $S$-wave velocity contrast of +2% ranges from: (1) 0.0662 - 0.1078 for epicentral distances where we have nonobservations, (2) 0.1078 - 0.1697 for the borderline observation distances, and (3) 0.1697 - 0.2132 for the good observation distances. These amplitude ratios are well above the average noise level (0.027) in our vespagrams. Thus, if the D" discontinuity extends laterally throughout our study region we should be able to observe the *Scd* arrivals on vespagrams. Yet because there is a relationship between epicentral distance and $Scd/S$ amplitude ratio, we cannot rule out the possibility that our nonobservations are solely due to decreased ability to detect the *Scd* arrival for these bins. But, we note that there is overlap in the epicentral distance range of nonobservations and borderline observations which suggests our nonobservations may be related to lower mantle structural effects.

The other possibility is that the D" discontinuity terminates near the eastern boundary of our study region. In order to assess this possibility, we computed synthetic seismograms for a series of 2.5-D models with a sharp eastern boundary on the D" discontinuity. The synthetics were computed for a discontinuity located 300 km above the CMB with a 2% $S$-wave velocity increase. For comparison, results for a 1-D continuous D" discontinuity model at the same height with the same velocity contrast are also shown in Figure 2.13a-b. We fixed the distance between the source and the center of the receiver array at 73° so that the *ScS* ray paths are centered at 35°. We allowed the position of the discontinuity edge to vary in angular distance from the source between 25° and 45° in 2° increments (±10° from the central *ScS* bounce-point); Figure 2.13a). We observe two important effects. First, as the edge position moves closer to the receiver array, the $Scd/S$ amplitude ratio decreases (Figure 2.14). When the edge reaches a position of +8° from the central *ScS* bounce-point, the $Scd/S$ amplitude ratio has decayed to 0.026, which is

below the average noise level (0.027) of our best data and would thus no longer be observable (Figure 2.13b). Even for an edge position of +4° the $Scd/S$ amplitude ratio has dropped enough to be within the range of noise observed in this study. This result suggests that the discontinuity edge can be located as far as +4° - +8° away (closer to the receivers) from the central $ScS$ bounce-point of the observations and still be detectable, yet if the edge is located greater than +4° from the boundary detectability will be challenging. Second, as the edge position increases this causes measurements of $\delta T_{Scd-S}$ to increase. This results in a decrease of our discontinuity height estimate (Figure 2.13c). For example, moving the edge position to +4° from the central $ScS$ bounce-points causes an increase in $\delta T_{Scd-S}$ of 1.3 sec, which in turn results in a decreased estimate of discontinuity height of roughly 20 km.

These two effects can be used to estimate the location of the discontinuity edge if it exists. For cluster A, the borderline cases are roughly located 2° to the east of the good cases and 3° west of the nonobservations (Figure 2.1b). They were previously not included in our average estimates of D" discontinuity structure because of their questionable $Scd$ arrivals with low amplitudes and poor slowness resolution. However, these characteristics are consistent with our synthetic predictions for a D" discontinuity model with a sharp edge (Figure 2.1b). If the edge is located 2° to 4° west of the central bounce-point of the good cases, the $Scd$ arrivals are still detectable for good and borderline observations (Figure 2.15). Additionally, the average height difference (64 km) of the D" discontinuity between the good (295 ± 20 km) and borderline cases (231 ± 28 km) suggests the edge should be located 4° to 6° west of the central bounce-point of the borderline cases. There is not a general pattern between the good and borderline observations in cluster B. We also tested models where the boundary edge has a shallower slope (Figure 2.16). Our results are consistent with a boundary that has a slope as shallow as 30°, yet $Scd$ amplitude considerations suggest the boundary is nearer to vertical (Figure 2.17). These synthetic analyses of a D" discontinuity with a sharp boundary suggests that the D" discontinuity may not extend across the North Atlantic Ocean; rather terminates abruptly between 45° and 50° W longitudes, which corresponds to the inferred position of the eastern most edge of the subducted Farallon plate.

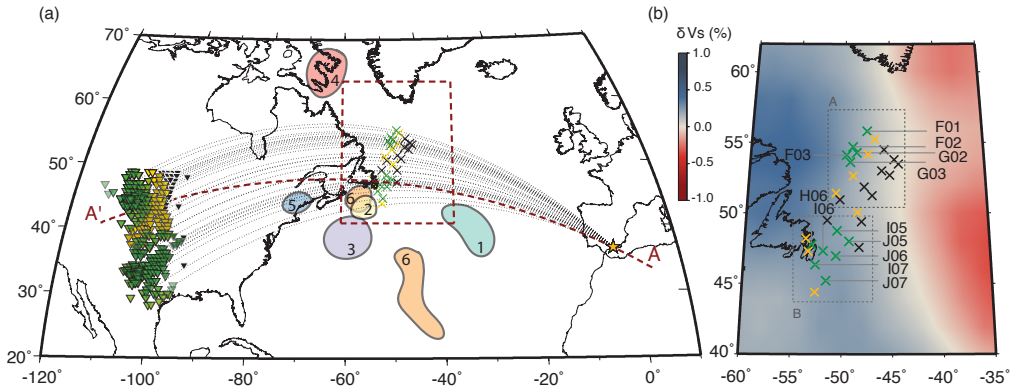


**Figure 2.1**. Summary of previous studies and our study. (a) Summary of previous studies of D" discontinuity structure beneath the North Atlantic and our study region (crosses). Previous studies are, 1: *Weber and Körnig*, 1992; 2: *Houard and Nataf*, 1992; 3: *Kendall and Shearer*, 1994; 4: *Krüger et al.*, 1995; 5: *Braña and Helffrich*, 2004; 6: *Wallace and Thomas*, 2005. The location of the M6.3 southern Spain event and broadband stations used in this study are shown as a yellow star and inverted triangles, respectively. The great circle ray paths are shown as black, dashed lines. The theoretical bounce points of *ScS* on the CMB as calculated by Taup [*Crotwell et al.*, 1999] are shown as green crosses (good cases), yellow crosses (borderline cases) and black crosses (no-*Scd* arrival). (b) Detailed view with labeled bins and two clusters of our study area displayed on top of *S*-wave tomography model TXBW [*Grand*, 2002] at the CMB.

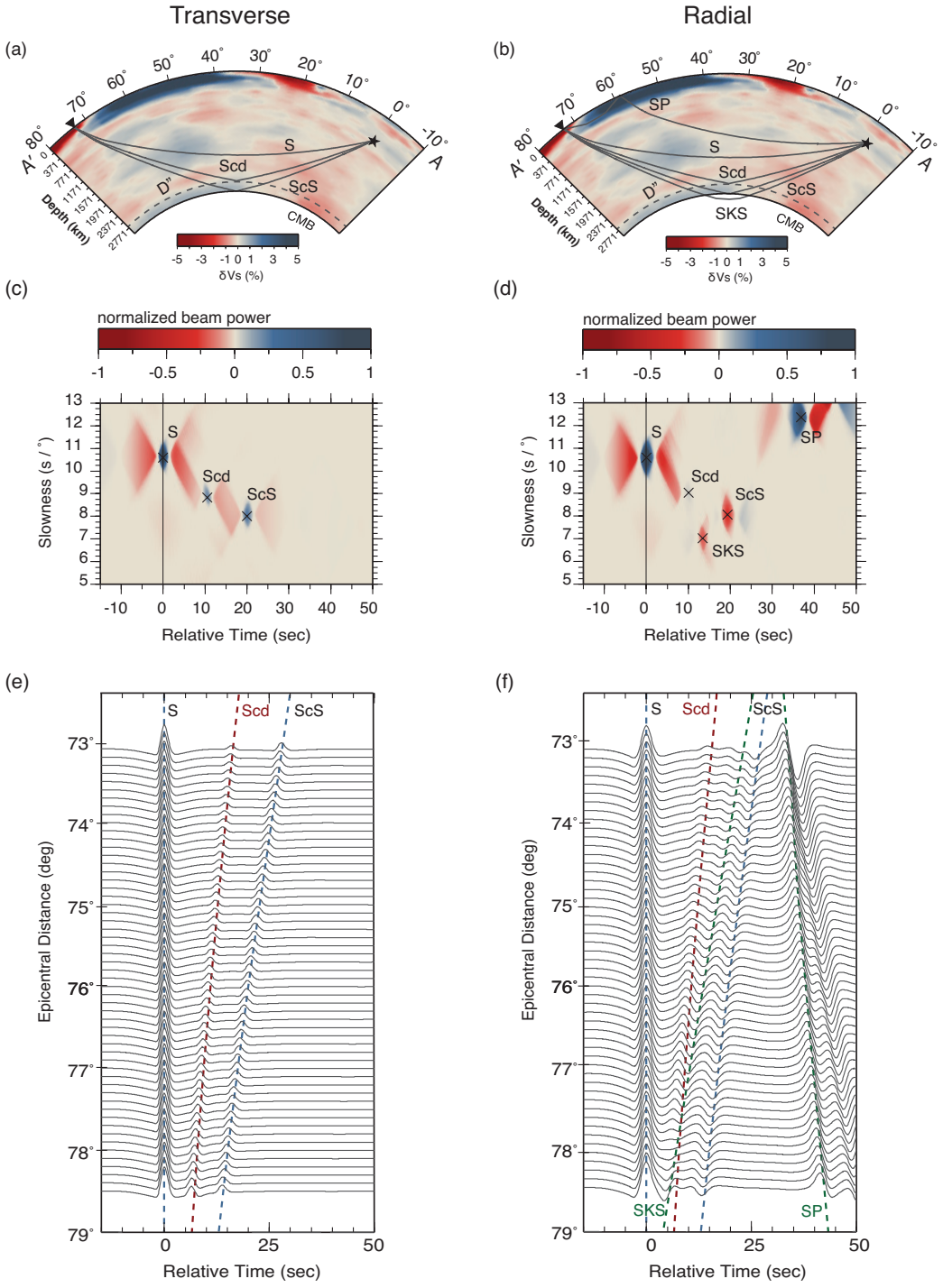


**Figure 2.2**. Ray paths observed in our study on top of a cross section through $S$-wave tomography model TXBW from event to station (AA' in Figure 2.1) of a) the transverse component and b) the radial component. Synthetic vespagrams and seismic record sections are aligned and normalized to unity on the direct $S$-wave, and labeled by the phase names.

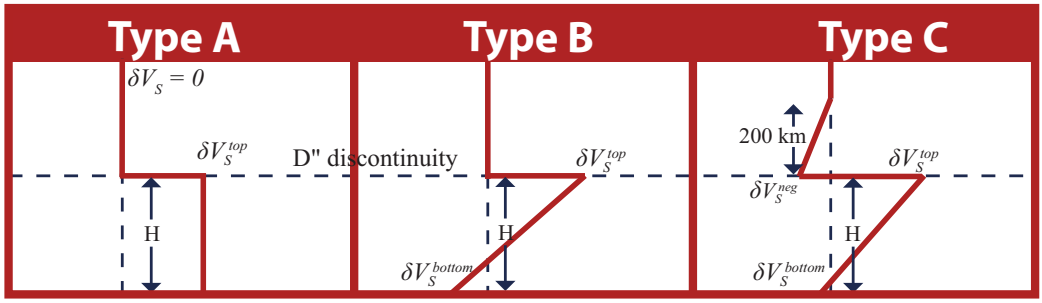


**Figure 2.3**. The three types of models are type a) A positive velocity increase at the top of the D" discontinuity which is continued down to the CMB; type b) A positive velocity increase at the top of the D" discontinuity followed by a negative velocity gradient down to the CMB; and type c) The same as type b, except this model also has a negative velocity gradient starting at 200 km above the D" discontinuity. For each model type, we changed the position of the D" discontinuity from 150 to 375 km above the CMB in 25 km increments and changed the $S$-wave velocity perturbation from 1% to 3% in 1% increments. We used reflectivity, SHaxi, and PSVaxi to generate the synthetic seismograms. The reflectivity method was used for generating synthetics for 58 1D model profiles, and the SHaxi technique was used for generating synthetics for both 1D profiles (for comparison to reflectivity technique) and also for more complicated 2D geometries which are described in the Discussion and Conclusions section. The PSVaxi technique was used for computing radial component synthetics.

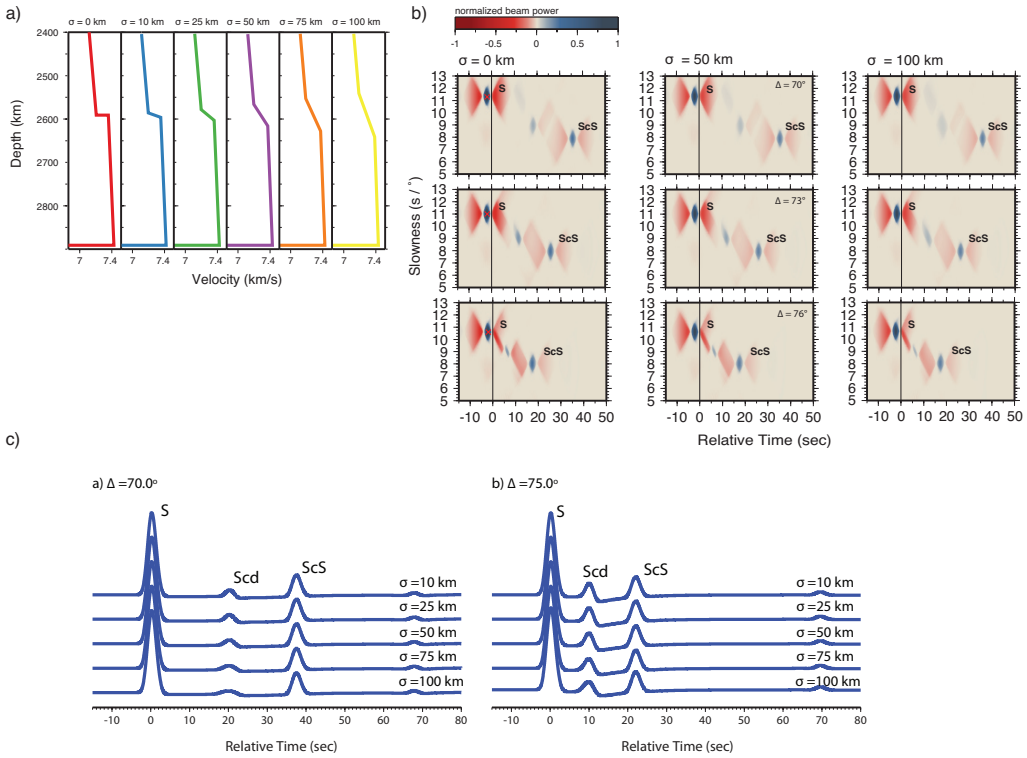


**Figure 2.4**. Velocity profiles, synthetic seismograms and vespagrams of a D" discontinuity with a "velocity transition zone". a) Velocity profiles of 1-D discontinuity models with the *S*-wave velocity changing from 0% to 2% continuously in a "velocity transition zone" ranging from 10 km to 100 km thick centered at 300 km above the CMB. b) Synthetic vespagrams of models with a sharp boundary, 50 km thick "velocity transition zone" and 100 km thick "velocity transition zone" at 70°, 73°, and 76°. c) Synthetic seismograms computed based on D" discontinuity models with "velocity transition zone" for receivers located at a) 70°and b) 75°. These models have a *S*-wave velocity increase from 0% to 2% in the "velocity transition zone" with the thickness of 10 km, 25 km, 50 km, 75 km, and 100 km, respectively, centered at 300 km above the CMB. Our results demonstrate that as the "velocity transition zone" becomes thicker, the energy of the *Scd* arrivals on the vespagrams become less concentrated, and the *Scd* arrivals become broader with lower amplitudes on synthetic traces. We also noticed that the pulse broadening is distance dependent: that is, it is relatively more significant for shorter distances (70°) than for longer distances (75°). We picked the travel times and slowness of *Scd* phase from these vespagrams and obtained identical results regardless of the thickness of the transition in velocity. The *Scd/S* amplitude ratio decreased as we increased the thickness of the "velocity transition zone", but even for the 100 km thick "velocity transition zone", the *Scd/S* amplitude ratio (0.049) for the shortest distance (70°) is still well above averaged noise level (0.027). Therefore, we can still resolve D" discontinuity for 7 sec dominant period waves at the shortest epicentral distance for a 100 km thick "velocity transition zone". In our study area, it is possible that the discontinuity is not a sharp discontinuity. If so, our depth estimations represent the central depth of the "velocity transition zone".

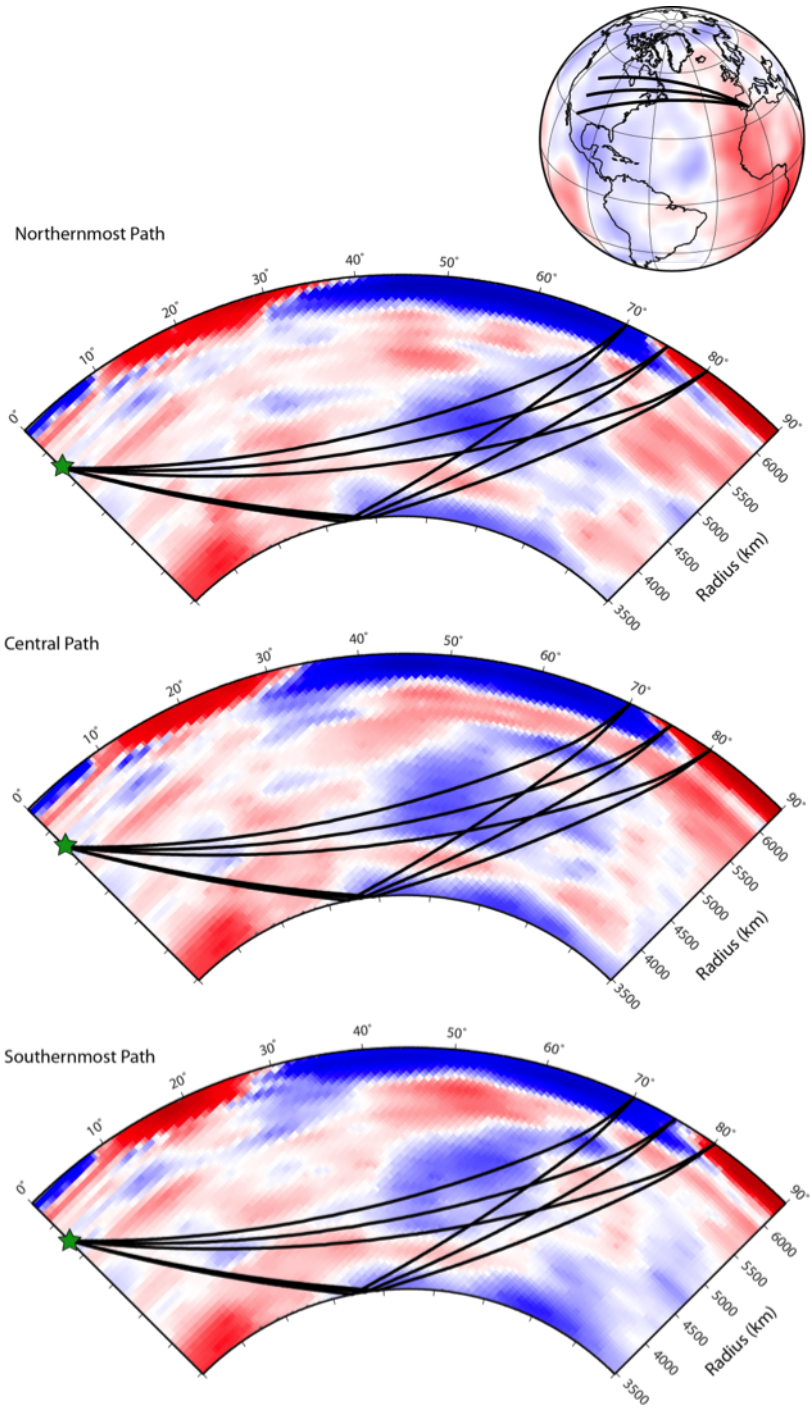


**Figure 2.5**. Mid-mantle seismic wave speed heterogeneity could bias our results if we do not have stable *ScS*-*S* differential travel-times across our study region. In order to assess this possibility we computed synthetic seismograms through three cross-sections of mantle tomography TXBW [*Grand*, 2002] for paths that sample the northernmost, center, and southernmost source-receiver combinations. The globe plot in the upper righthand corner is colored by tomography at the CMB. Ray paths for *S* and *ScS* at distances of 70°, 75°, and 80°are indicated.

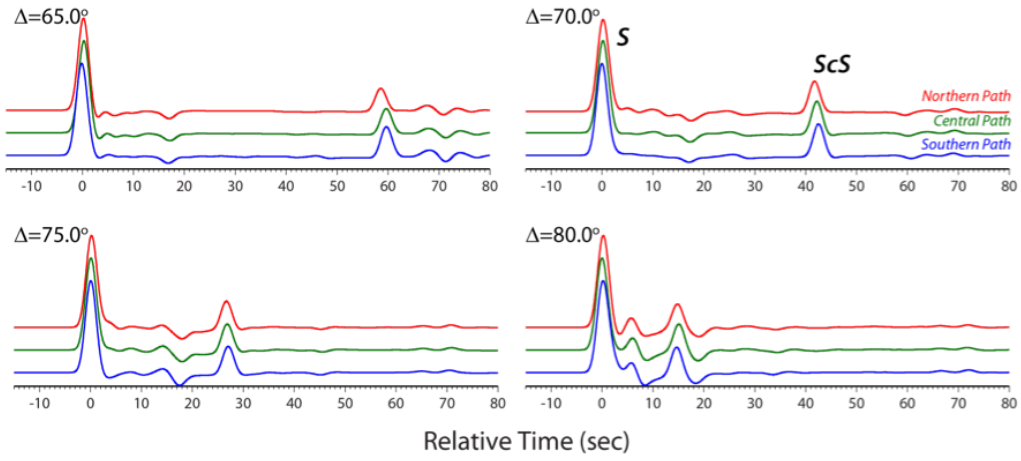


**Figure 2.6**. Synthetic seismograms through tomography cross-sections shown in Figure 2.5. Seismograms are shown at four different epicentral distances (65°, 70°, 75°, and 80°), for the northernmost cross-section (red traces), the central cross-section (green traces), and the southernmost cross-section (blue traces). All seismograms are aligned on the direct $S$-wave arrival.

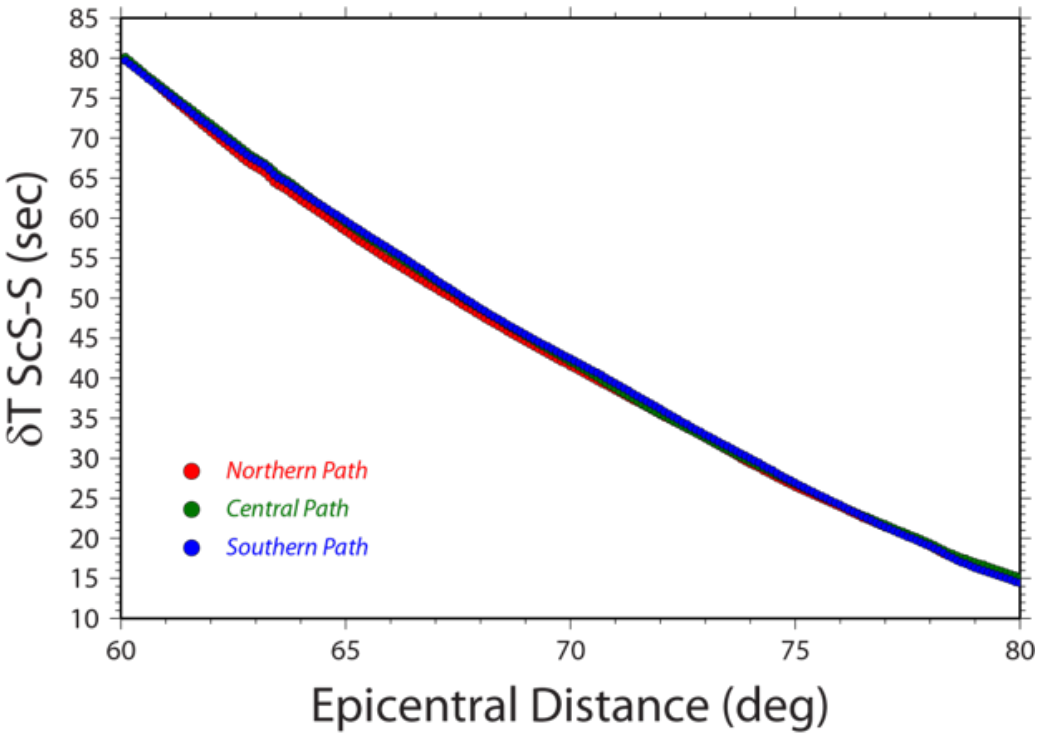


**Figure 2.7**. *ScS-S* differential travel times for the three tomography sections. Red circles are for the northernmost path, green circles are for the central path, and blue circles are for the southernmost path. Because of the limited geographical extent of our study region and the long wavelength nature of the mantle tomography model, for epicentral distances greater than 60° there is an average of 0.54 s difference in *ScS-S* differential travel-times with a maximum 1.4 s at a distance of 65°. These time differences will negligibly affect our discontinuity height estimates ($<$ 10 km) and we thus do not perform tomography based travel time corrections to these data.

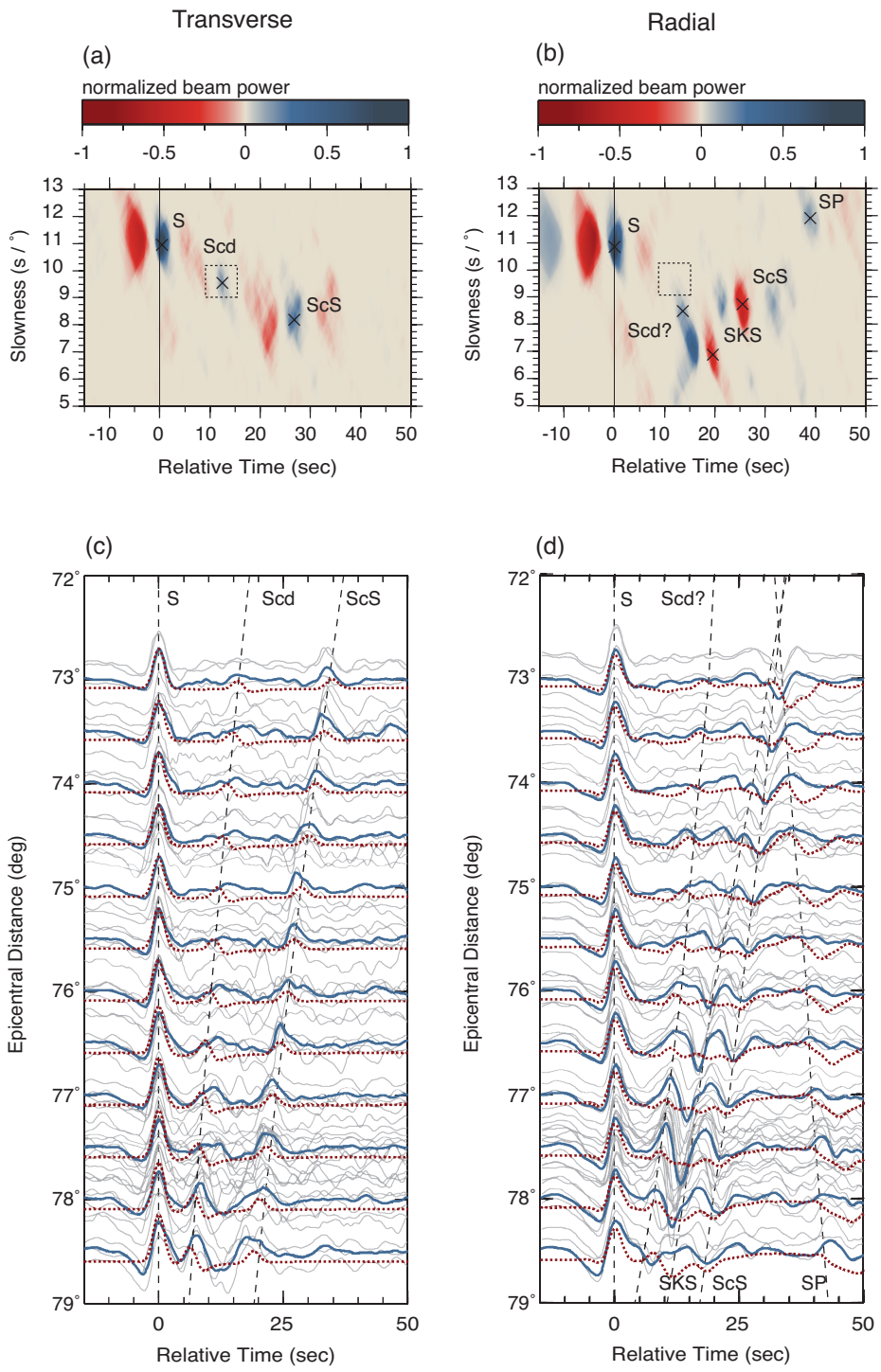


**Figure 2.8**. Example vespagrams and record sections of the (a, c) transverse component and (b, d) radial component (bounce-points centered at 47.32° N, 51.98° W and labeled as I06 in Figure 2.1b). Seismic traces were stacked per 0.5° (blue lines) and labeled with phase names. The stacked transverse and radial synthetic seismograms of best-fit model (model 57) of this bin were plotted as dashed red lines in (c) and (d) for comparison.

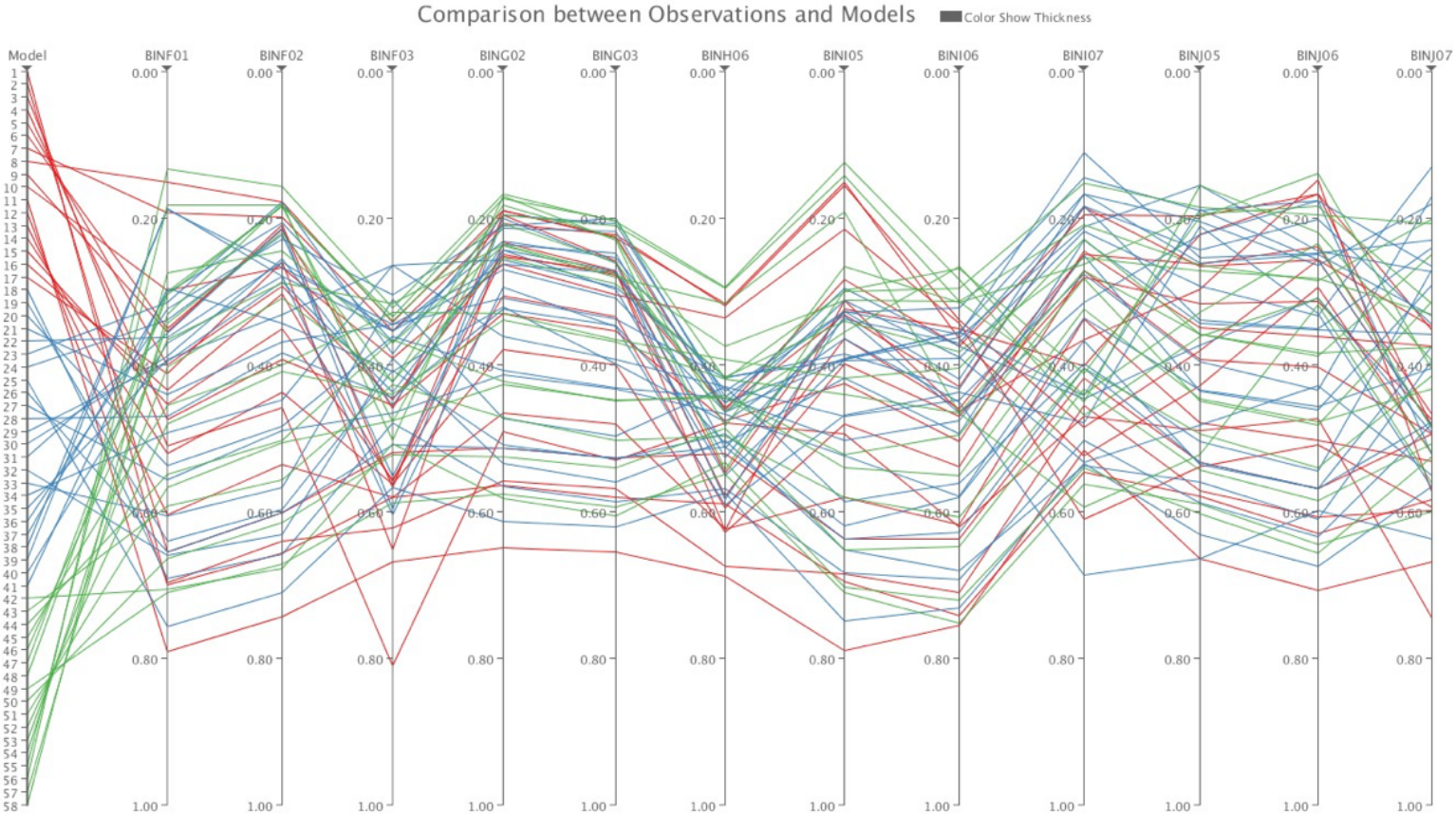


**Figure 2.9**. The data/synthetic misfits of 58 synthetic models based on 12 good observations. In all cases the overall misfit lies between 0.1 and 0.8, with the misfit of the best-fitting model for each bin at around 0.2. Type b (blue lines) and type c (green lines) models provide a better estimation than type a (red lines) models. Online dynamic figure: `http://home.utah.edu/~u0742435/index_research.html`.

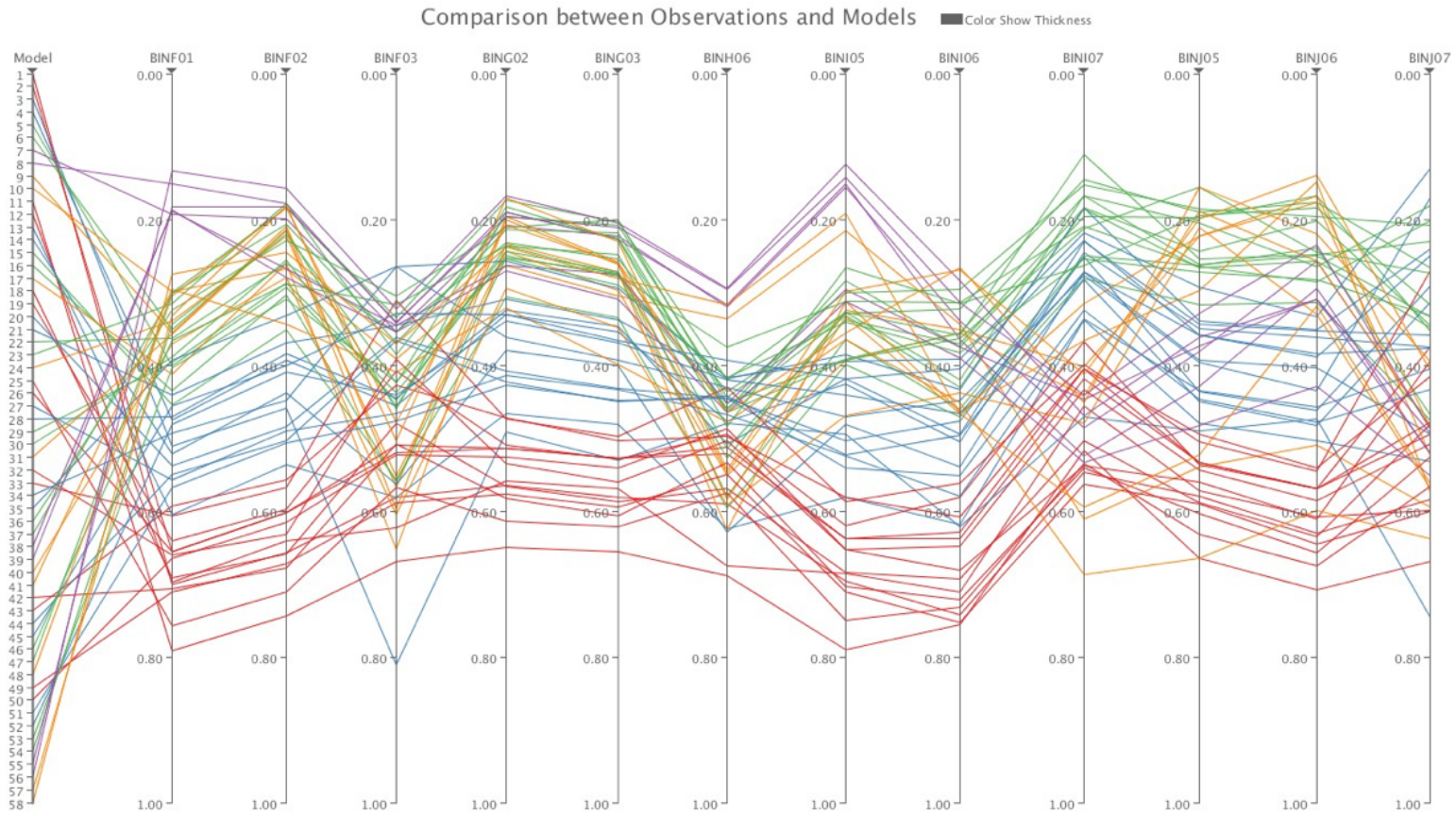


**Figure 2.10**. The data/synthetic misfit of 58 synthetic models based on 12 good observations. Color represents the elevation of D" discontinuity above the CMB: 150 and 175 km (red); 200 and 225 km (blue); 250 and 275 km (green); 300 and 325 km (purple); 350 and 375 km (orange). The misfits are more sensitive to the elevation of the discontinuity than of the velocity contrast at the top of the discontinuity. Models sharing the same discontinuity thickness (same color) have similar misfits. Online dynamic figure: `http://home.utah.edu/~u0742435/index_research.html`.

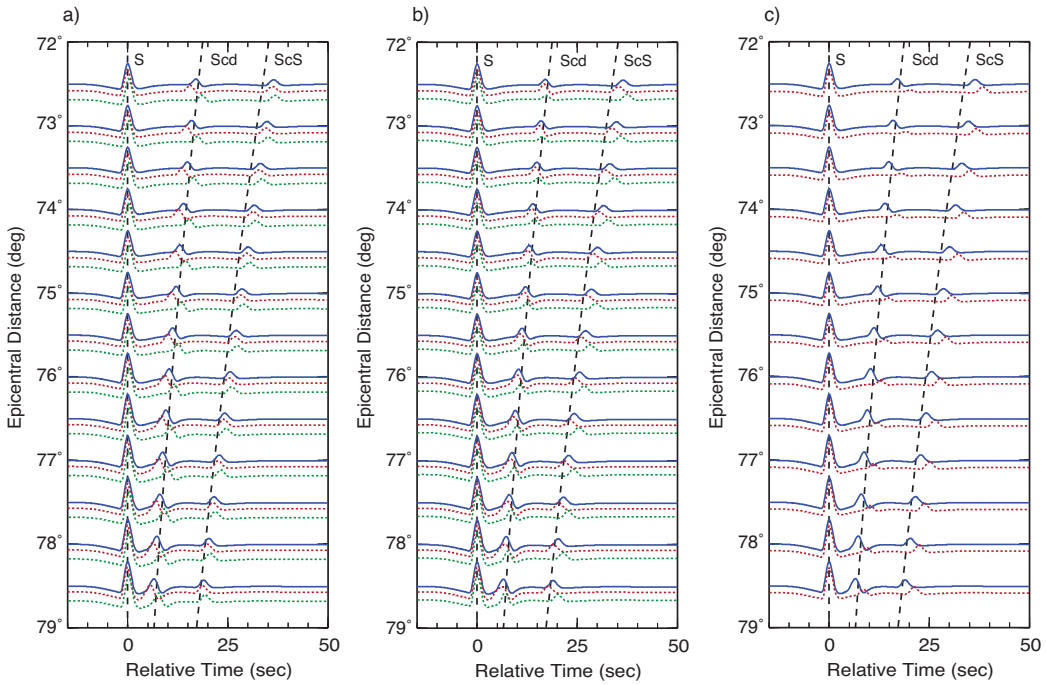


**Figure 2.11**. The waveform variations due to a) the variation of D" discontinuity thickness (red: +25 km, green: -25 km, blue: reference), b) variation of the velocity contrast at the top of the D" discontinuity (red: +1%, green: -1%, blue: reference), and c) the variation of model type (red: type A model, blue: reference).

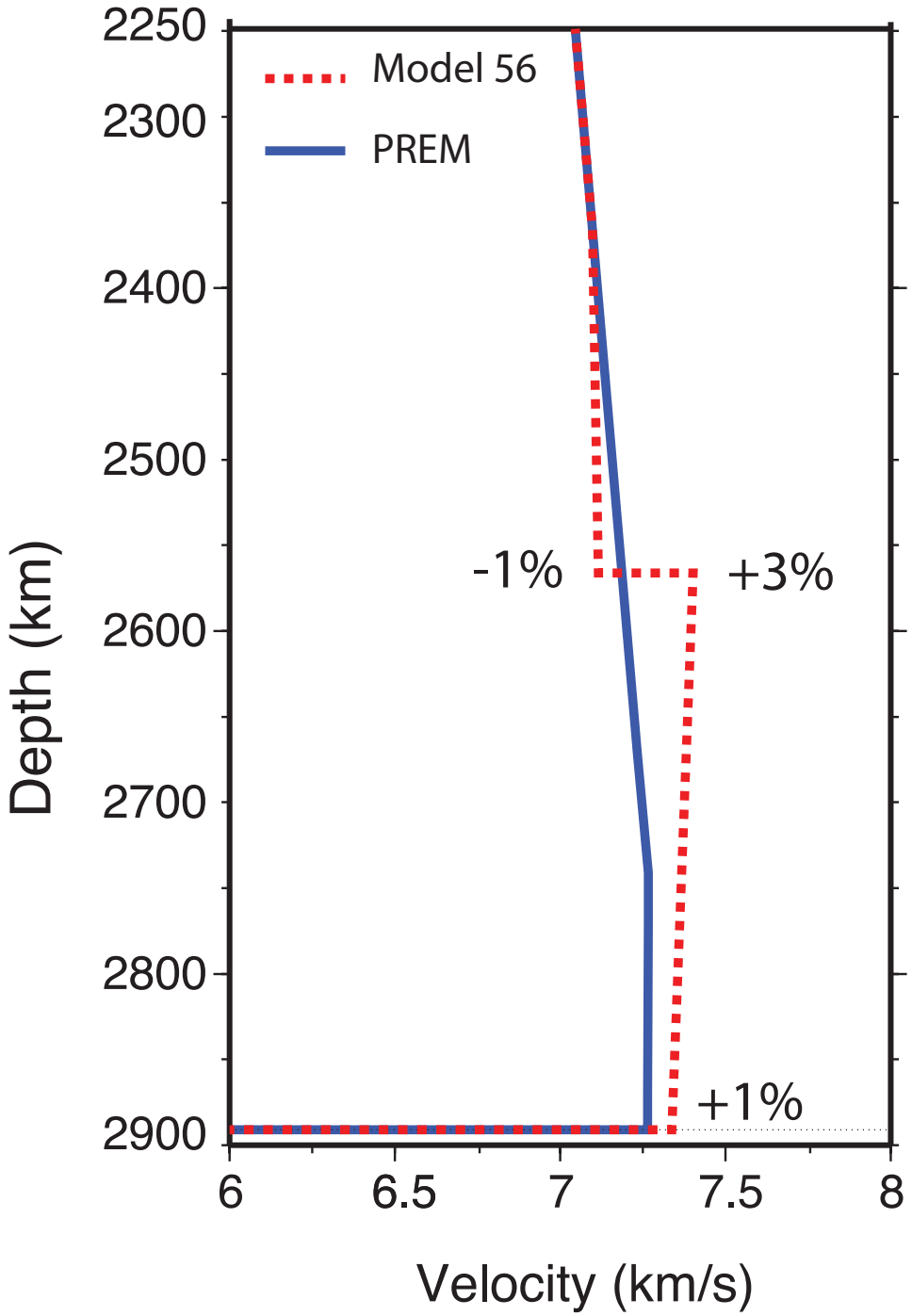


**Figure 2.12**. *S*-wave velocity profiles near D" discontinuity of the best-fit model (M57) of the bin I06 (red dashed line) and PREM model (blue).

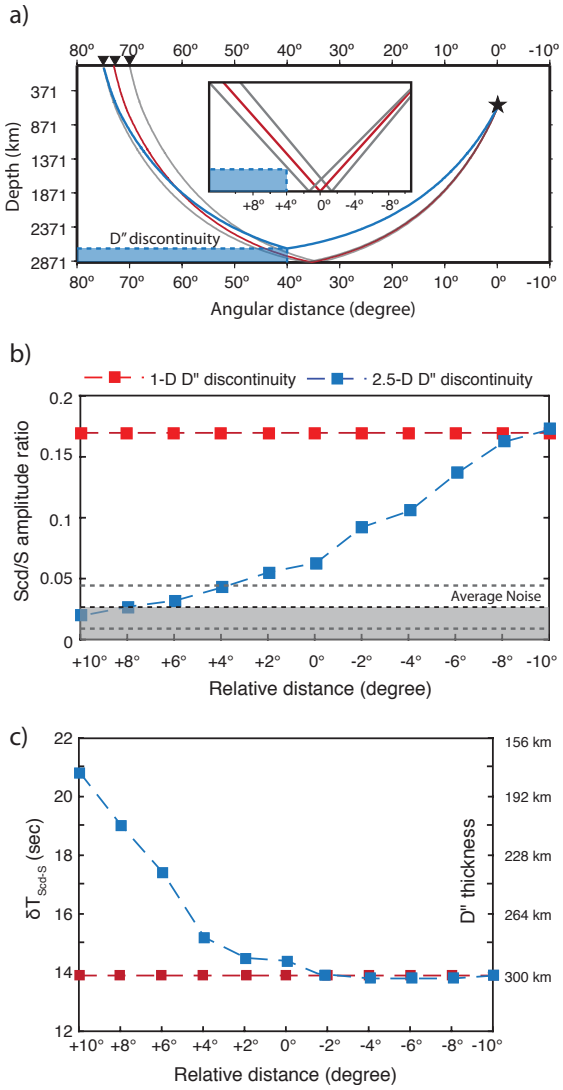


**Figure 2.13**. Sketch of the 2.5-D D" discontinuity model with a sharp edge. a) Sketch of the 2.5-D D" discontinuity model with a sharp edge. The inset shows detail near the CMB, and plots angular distance of the edge of the fast anomaly relative to the *ScS* CMB bounce point for an epicentral distance of 73°. b) Shows the *Scd/S* amplitude ratio with respect to the relative distance from the edge of the fast anomaly. Observed noise is plotted as average noise level (black-dashed line) and standard deviation (grey-dashed line). c) Travel time difference between *Scd* and *S* of the 1-D (red) and 2.5-D (blue) model as a function of relative distance from the edge of the fast anomaly. D" height estimates based on $mathbf{\sigma T_{Scd\text{-}S}}$ are shown on the right-hand y-axis.

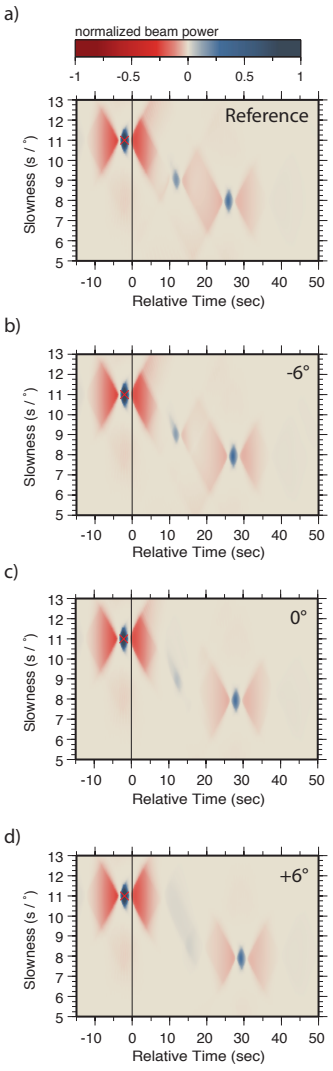


**Figure 2.14**. Example vespagrams for the (a) 1-D reference model and 2.5-D D" discontinuity with sharp edge models; b) edge located at -6° from the central *ScS* bounce-point; c) edge located at the central *ScS* bounce-point; d) edge located at +6° from the central *ScS* bounce-point.

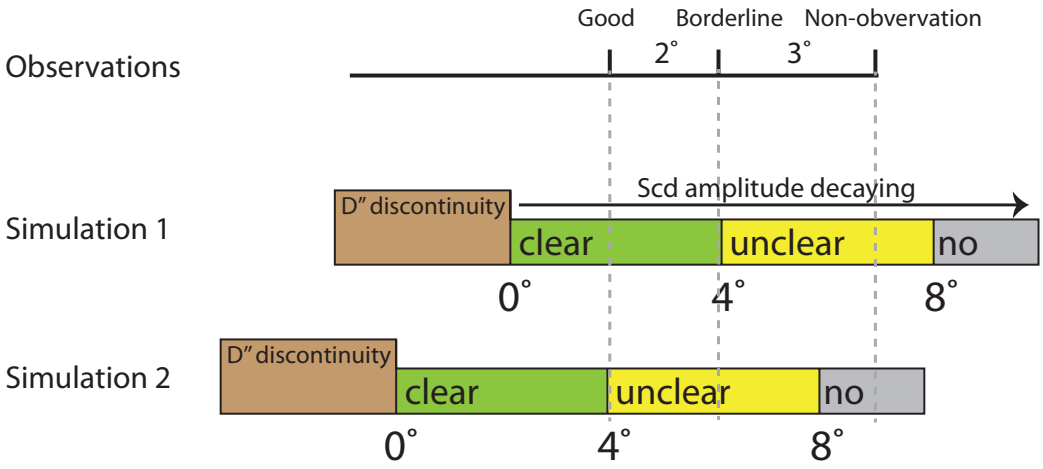


**Figure 2.15**. The estimate of the position of the edge based on the detectability of the *Scd* arrivals. The first panel shows the spatial relationship for the three types of observations (good, borderline and nonobservations). The second panel shows the first scenario where the edge is located 2° from the good case. The third panel shows the second scenario where the edge is located 4° from the good case.

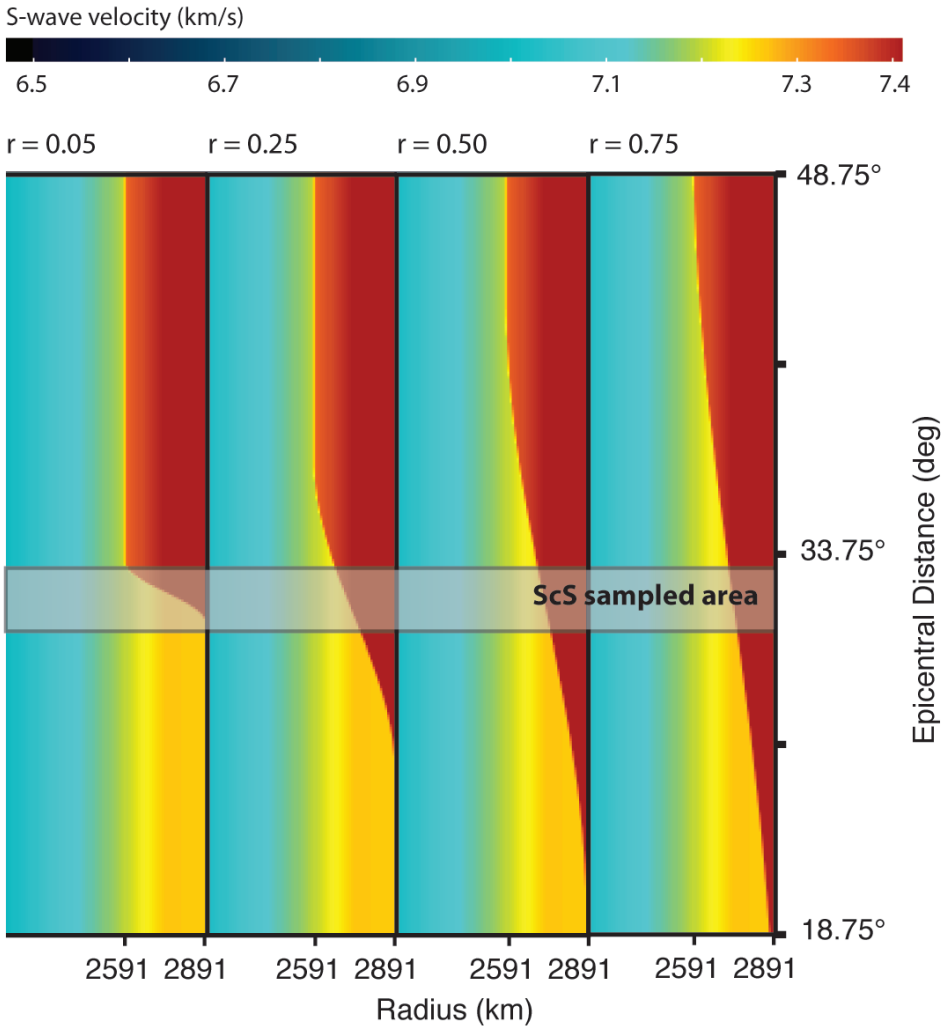


**Figure 2.16**. In our study, we used a Tukey window to define the shape of the edge of the D" discontinuity. A Tukey window is essentially a cosine function convolved with a rectangular window with the width of the cosine defined by the parameter r (r = 0 leads to a rectangular window). The models used in the manuscript use the parameter r=0.05 (the D" discontinuity builds up from 0 km to 300 km in 2.5°, which is 152 km on the surface of CMB). Here we tested more models (r = 0.25, r = 0.5, and r = 0.75) to investigate inclined edges. The discontinuity is located 300 km above the CMB with 2% *S*-wave velocity increase. The shaded area represents the locations of the theoretical *ScS* bounce points at the CMB for receivers located in the 70° to 75° range.

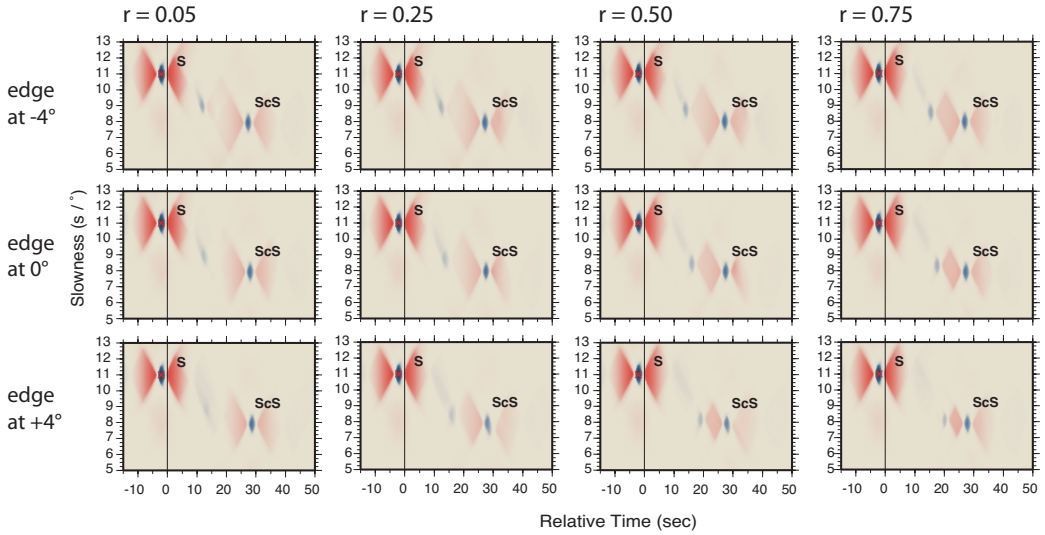


**Figure 2.17**. Synthetic vespagrams of models with different parameter r as shown in Figure 2.16. The edges are located at -4°, 0°, and +4°. Our results show that for relatively steeper edges (r $<$ 0.5), the energy of the *Scd* arrivals on the vespagrams becomes less concentrated as the edge moves away from the source. We also observed decreasing amplitudes and delayed travel times of *Scd* arrivals as the edge moves away from the source. However, for edges with more gentle slopes, the *Scd* waves behave as though they sample a small region on the slope of the edge, leading to relatively stable and concentrated *Scd* arrivals on the vespagrams. The difference in inferred discontinuity height (64 km) between our good observations and our borderline observations vary over about 2° laterally on the CMB which corresponds to a slope of approximately 30°. Thus, we cannot rule out a more slanted edge to the discontinuity, yet, we note that the amplitude of the *Scd* arrivals for our borderline cases are not as large as the amplitude for our good cases, which is more consistent with a sharp vertical edge because we do not see a similar *Scd* amplitude decay for the synthetic tests with a sloped edge.

**Table 2.1** Summary of synthetic models used in this study.

| Type A | | | | |
|---|---|---|---|---|
| Model | Height above the CMB (km) | $\delta V_S^{top}$ | | |
| 1–10 | 150 – 375 km (25 km increments) | 2% | | |
| 11–16 | 150 – 275 km (25 km increments) | 2% | | |
| 17 | 350 km | 2% | | |
| **Type B** | | | | |
| Model | Height above the CMB (km) | $\delta V_S^{top}$ | $\delta V_S^{bottom}$ | |
| 18–23 | 150 – 275 km (25 km increments) | 2% | 0% | |
| 24 | 350 km | 2% | 0% | |
| 25–30 | 150 – 275 km (25 km increments) | 3% | 1% | |
| 31 | 350 km | 3% | 1% | |
| 32–41 | 150 – 375 km (25 km increments) | 2% | -2% | |
| **Type C** | | | | |
| Model | Height above the CMB (km) | $\delta V_S^{neg}$ | $\delta V_S^{top}$ | $\delta V_S^{bottom}$ |
| 42–47 | 150 – 275 km (25 km increments) | -1% | 2% | 0% |
| 48 | 350 km | -1% | 2% | 0% |
| 49–58 | 150 – 375 km (25 km increments) | -1% | 3% | 1% |

*see Figure 2.3 for types of model

**Table 2.2** Summary of best-fit models for good observations

| Bin name | Cluster | Distance (degree) | Number of traces | Best-fit Model | D" Thickness |
|---|---|---|---|---|---|
| BINF01 | A | 71°-73° | 11 | 56 | 325 km |
| BINF02 | A | 71°-76° | 48 | 56 | 325 km |
| BINF03 | A | 73°-76° | 35 | 34 | 225 km |
| BING02 | A | 70°-74° | 68 | 56 | 325 km |
| BING03 | A | 71°-76° | 67 | 47 | 275 km |
| BINH06 | B | 75°-79° | 52 | 56 | 325 km |
| BINI05 | B | 71°-76° | 42 | 56 | 325 km |
| BINI06 | B | 72°-78° | 62 | 57 | 350 km |
| BINI07 | B | 74°-80° | 39 | 22 | 250 km |
| BINJ05 | B | 69°-74° | 34 | 48 | 350 km |
| BINJ06 | B | 71°-76° | 35 | 57 | 350 km |
| BINJ07 | B | 73°-78° | 28 | 35 | 225 km |

# CHAPTER 3

# *P*- AND *S*-WAVE SLOWNESS ANOMALIES IN THE MANTLE BENEATH THE NORTH PACIFIC

## 3.1 Introduction

The first seismic arrays were originally built to detect and identify explosions in 1960s [*Davies*, 1973]. However, they have also been widely used to resolve the fine-scale structure of the Earth [*Rost and Thomas*, 2009]. In recent decades, a number of seismic arrays have been installed around the globe including temporary arrays such as Portable Array Seismic Studies of the Continental Lithosphere (PASSCAL) experiments (e.g., EAGLE [*Bastow et al.*, 2005]; CANOE [*Mercier et al.*, 2008], to name a few), as well as permanent arrays (Hi-net [*Yee et al.*, 2014]) and movable arrays such as the transportable array (TA) component of USArray [*Meltzer*, 2003]. Among these arrays, the TA, with over 400 broadband seismographs and 14 years of operation, has provided an unprecedented data set that has allowed for creative new studies of Earth's interior by methods previously only imagined. For example, with the help of the dense spatial sampling of the seismic wave field provided by the TA, significant progress has been made in enhancing our understanding of the deep earth velocity heterogeneities such as the D" discontinuity [e.g., *Yao et al.*, 2015; *Whittaker et al.*, 2016; *Sun et al.*, 2016], ultra low-velocity zone [e.g., *Rost et al.*, 2010; *Cottaar and Romanowicz*, 2012], and mantle transition zone discontinuities [e.g., *Schmandt*, 2012; *Tauzin et al.*, 2013]. Ambient noise recorded by the TA has also provided opportunity to examine the detailed structure of the inner-core by retrieving core-sensitive body waves using seismic interferometry [*Lin et al.*, 2013; *Huang et al.*, 2015]. Furthermore, tomographic imaging of the crust and upper mantle beneath the United States has

greatly improved with the addition of the USArray data [e.g., *Burdick et al.*, 2008; *Lin et al.*, 2008; *Schmandt and Humphreys*, 2010; *Sun and Helmberger*, 2011].

One of the main attractions of using seismic array data is its ability to directly measure slowness ($dT/d\Delta$) of incident signals. Some previous studies have explored the possibility of measuring slowness of diffracted and direct seismic phases based on small aperture arrays and have used them to probe the velocity structures in the lower mantle. Slowness of diffracted seismic waves like *Pdiff* and *Sdiff* is expected to be most sensitive to the core-mantle boundary (CMB) lateral heterogeneities at the point where the ray paths leave the CMB, thus, these phases have been used to probe lowermost mantle structures like ULVZs [*Xu and Koper*, 2009] and the D" layer [*Valenzuela et al.*, 2000]. For the slowness measurements of direct seismic phases, most of these previous efforts have been focused on *P*-wave arrivals. However, there is much uncertainty in these studies as to whether slowness anomalies were related to near-receiver structures in the upper mantle and crust [e.g., *Berteussen*, 1976; *Burdick and Powell*, 1980; *Steck and Prothero*, 1993; *Hao and Zheng*, 2010], or in the lower mantle [e.g., *Chinnery and Toksöz*, 1967; *Johnson*, 1969; *Kulhánek and Brown*, 1974; *Muirhead and Hales*, 1980; *Tibuleac and Herrin*, 1999]. For example, *Chinnery and Toksöz* [1967] measured *P*-wave slowness of teleseismic events in the distance range 27° to 90° recorded by the LASA array in Montana in a narrow azimuth range (300° - 320°). They observed greater than usual slowness values around 800 km, 1300 km and 2000 km depth, indicating the *P*-wave velocity changes much more slowly in these depths. They concluded that these slowness anomalies have a mantle origin instead of originating in the crustal and upper mantle structure under the LASA array for the following reasons: 1) Strong slowness anomalies were still present after station corrections based on local crust and upper mantle structures; and 2) In addition to the data recorded by LASA array, they also investigated the data from LONGSHOT nuclear experiments recorded by U.S. and European stations. They calculated the *P*-wave travel time residuals with respect to a 1-D reference model and observed the same travel time residuals pattern around 800 km, 1300 km, and 2000 km depth for both data sets; 3) *P*-wave amplitude observations from both LASA and LONGSHOT nuclear experiments show low amplitudes if the ray path

samples these depth regions. *Tibuleac and Herrin* [1999] estimated the slowness of *PcP*- and teleseismic *P*-wave arrivals using small-aperture TXAR array in Texas and YKA array in Canada. They observed strong slowness anomalies in *PcP*- and *P*-wave arrivals and demonstrated that the slowness anomalies were caused by lateral inhomogeneities in the lower mantle beneath the Gulf of Mexico and the Caribbean Sea. They eliminated the hypothesis of shallow anomalies under the arrays because both *S*-wave and *PcP*-wave arrivals show the slowness anomaly only if their ray paths travel through a region located 1300 km depth the Gulf of Mexico and the Caribbean Sea. On the other hand, *Steck and Prothero* [1993] observed large perturbations in the *P*-wave slowness and azimuth of teleseisms recorded at Long Valley caldera by applying array processing techniques to 3-component arrays deployed during LNV and CST experiments. These two 2-km-aperture arrays were about 5 km apart from each other and the slowness anomalies from teleseismic events were significantly different at the two arrays. Therefore, they concluded the slowness perturbations were caused by crustal structure, probably between depths of 6 and 35 km. However, most of these slowness studies of direct seismic phases were conducted in short-period ($\sim$1 Hz) band with small aperture arrays (2 km-100 km). They were conducted before the deployment of the TA and no effort has been devoted to study the slowness anomalies of direct seismic phase using this large-aperture array which can provide better coverage and more stable observations.

In this study, we take advantage of the large amounts of seismic data recorded by broadband seismic stations in North America. We analyze high signal-to-noise teleseismic *P*- and *S*-wave arrivals from earthquakes occuring between January 2004 and June 2015 to study slowness anomalies in the mantle beneath the North Pacific.

## 3.2 Data and Slowness Perturbations

In this study, we searched for slowness anomalies associated with direct *P*- and *S*-wave arrivals. In order to search for potential slowness anomalies in the lower mantle, we focused on arrivals in the epicentral distance range between 40° and 90° because in this distance range the *P*- and *S*-wave arrivals have turning depths between

1000 and 2800 km. In this section, we first describe the data set we collected and then describe our method for determining slowness perturbations.

We collected seismic recordings from all broadband seismic stations in North America for earthquakes between January 2004 and June 2015 with moment magnitudes (Mw) between 5.8 and 7.5, event depths greater than 100 km, and epicentral distances from 40° to 90°. We chose this time range to coincide with deployments of the Transportable Array (TA) and Flexible Array (FA) components of the EarthScope program in order to take advantage of the large station coverage. We originally collected data for 92 events located along the North and West Pacific Rim. The original data set had 39,234 vertical component traces that were used to calculate $P$-wave slowness and 78,468 horizontal component traces that were later rotated to radial and transverse component traces. Data processing steps were: (1) We band-pass filtered these seismograms (0.05 Hz to 0.125 Hz for $P$-wave; 0.05 Hz to 3 Hz for $S$-wave); (2) We deconvolved the instrument response; and (3) Horizontal components were rotated to radial and transverse components and transverse components were later used to calculate $S$-wave slowness. We inspected each seismogram manually and discarded traces without detectable $P$- or $S$-arrivals. Our data set after this processing step had a total of 88 events with 38,752 vertical component traces and 34,271 transverse component traces.

In order to calculate slowness anomalies we first grouped data for each event into 2° radius geographic bins. We used a distance between bin centers of 2° which provided a partial overlap of recordings. Geographic bins with less than 10 traces were discarded. An example of geographic bins used for one event is shown in Figure 3.1. We calculated a slowness value for each geographic bin as described here. First, we calculated relative time shifts for each seismogram using the Automated and Interactive Measurement of Body-wave Arrival Times (AIMBAT) technique [*Lou et al.*, 2013]. AIMBAT is a python tool for measuring teleseismic arrival times based on the interactive cross-correlation and stack (ICCS) and the multi-channel cross-correlation (MCCC) methods. Second, we plotted the relative time shifts as a function of epicentral distance and calculated the best-fit line through a least-squares regression. The slowness ($\mathrm{dT/d\Delta}$) is then given by the slope of the regression line.

We threw out outliers with significant relative time anomalies which may strongly affect the slope of the regression line by excluding the data point if the residual between this data point and the best-fit line exceeds 3 times the standard deviation of the residuals between all data points in this bin and the best-fit line. Finally, the standard deviation of the residuals between the remaining data points and the regression line was calculated and used as an additional threshold (0.12 for $P$-waves, 0.25 for $S$-waves) to screen out potentially poor measurements. Thus, we only retained the highest quality slowness measurements. Examples of an accepted and a discarded slowness value calculation are shown in Figure 3.2a-b. As a further check on data quality, we created an estimate of the source-time function for each event by stacking the shifted traces. Here, we examined each stack to ensure that source complexity was not contaminating our slowness estimate. No events were discarded because of source complexity issues. An example stack is shown in Figure 3.2c. Our final dataset consisted of 1,232 $P$-wave slowness measurements from 59 events and 570 $S$-wave slowness measurements from 47 events, with turning point depths ranging from 1000 km to 2800 km beneath the North Pacific (Figure 3.3).

We next calculated a slowness perturbation, which we defined as:

$$\delta S = (S_{obs} - S_{prd})/S_{prd} \tag{3.1}$$

where $\mathbf{S}_{obs}$ is the observed slowness and $\mathbf{S}_{prd}$ is the predicted slowness value calculated using the TauP toolkit [*Crotwell et al.*, 1999] based on the AK135 earth model [*Kennett et al.*, 1995].

## 3.3 Crust and Upper Mantle Travel Time Corrections

Our slowness observations represent the accumulated slowness anomaly caused by all velocity heterogeneities along the ray path. In order to isolate potential lower mantle anomalies, travel time corrections for crust and mantle structures along the ray path must be made.

In this study, we first calculated the ray path of $P$- and $S$-waves for each event-station pair for the 1-D earth model AK135. We next calculated the $P$- and $S$-wave travel time deviation along the ray path through a single tomography model or combinations of tomography models for the crust (depth range of 0 - 60 km)

and/or for the upper mantle (depths from 60 - 1100 km), as described below. Next, we subtracted the travel time deviations predicted by tomography models from our original travel time measurements to correct for the crust and upper mantle velocity structure. We constructed four kinds of travel time corrections based on different combinations of tomography models, then evaluated which correction method would work best for our data set. Four kinds of correction methods are described below:

1. Receiver-side crustal travel time correction: we applied receiver-side (North American side) crustal (depths from 0 to 60 km) travel time correction for $S$-wave based on the 3-D crustal $S$-wave velocity model for the U.S. of *Schmandt and Lin* [2014]. For $P$-wave crust travel time correction, we modified the 3-D crustal $S$-wave velocity model mentioned above into a $P$-wave velocity model by multiplying the average $V_P/V_S$ ratio in the crust (1.73) to the $S$-wave velocity.

2. Receiver-side crust and upper mantle travel time correction: For both $P$ and $S$-wave, we corrected travel times for the crust as stated in correction method 1. In addition, we applied mantle (depths 60 - 1100 km) travel time correction on the receiver-side of the ray path using the $P$- and $S$-wave 3-D upper mantle velocity model of *Schmandt and Lin* [2014].

3. Source- and receiver-side crust and upper mantle travel time correction: for the receiver-side, we corrected travel times for the crust and mantle (depths 0 - 1100 km) using the model of *Schmandt and Lin* [2014]. For the source-side, we used the global $P$-wave model of *Li et al.* [2008] (depths 30 to 1100 km) to correct for $P$-wave travel times, and the global $S$-wave model of *Grand* [2002] (depths 100 to 1100 km) to correct for the $S$-wave travel times.

4. LLNL-G3D model source-side and receiver-side crust and upper mantle travel time correction: we corrected travel times on both the source- and receiver-side for the crust and upper mantle (depths 0 - 1100 km) using the global tomography models LLNL-G3Dv3 for $P$-waves [*Simmons et al.*, 2012] and LLNL-G3D-JPS for $S$-waves [*Simmons et al.*, 2015].

For each correction method, we used one tomography model, or a combination of different tomography models. These tomography models differ from each other in both large- and fine-scale features. It is thus difficult to evaluate which model provides

the most accurate travel time correction. However, we can evaluate which part of the shallow velocity heterogeneities (e.g., receiver-side or source-side, crust only or both crust and mantle) will affect our slowness observations the most, as well as which correction method works best with our travel time correction algorithm. For example, if the shallow velocity heterogeneities on the source-side do not produce large amounts of slowness perturbations, but applying source-side travel time correction based on the tomography model and travel time correction algorithm we choose will introduce more errors (See Section 3.6.1 for details of the errors caused by travel time correction algorithm), then we should not apply this travel time correction. Our ultimate goal in this step is to identify one or two correction methods which can reduce the effects of shallow velocity heterogeneities on the slowness observations to the greatest extent and minimize the errors induced by the travel time correction algorithm. We achieved this by applying travel time corrections to synthetic seismograms computed from tomography models, then investigating how well the travel time correction can correct for the known structures in these tomography models. For each correction method, we insert the 3-D tomography model(s) used in this correction method into a 3-D background seismic velocity model (here we used 3-D version of AK135). For example, for correction method 1, the resulting model has the $P$- and $S$-wave crustal structures beneath the U.S. from *Schmandt and Lin* [2014], while the rest of this model is AK135. Then we pick ten source-receiver pairs and extract 2-D velocity cross-sections for each source-receiver pair from this model. These cross-sections are used as velocity models to generated synthetic seismograms. We generate $P$-/$SV$- and $SH$- synthetic seismograms for stations from 40° to 90° with station spacing of 1° using PSVaxi [*Thorne et al.*, 2013] and SHaxi [*Jahnke et al.*, 2008] techniques (more details on these methods are provided in Section 3.4). The next step is to apply travel time correction from 0 to 1100 km to these synthetic seismograms based on different correction method. Finally, the slowness values of the corrected synthetic seismograms were calculated and compared with the AK135 reference slowness values. Ideally, if our travel time correction algorithm is perfect, we should be able to correct all velocity heterogeneities shown in the inserting tomography models, and the resulting slowness values of the corrected synthetic seismograms should completely match the

AK135 reference values. However, in practice we always have some misfit between the corrected slowness values and the AK135 reference slowness values. We defined the misfit as:

$$\delta S = (S_{cor} - S_{AK135})/S_{AK135} \tag{3.2}$$

where $\mathbf{S}_{cor}$ is the corrected synthetic slowness and $\mathbf{S}_{AK135}$ is the AK135 reference slowness. We calculated the mean misfit for all 10 cross-sections for the four correction methods. Our results show travel time correction method 2 ($\delta S = 0.6\%$) and method 4 ($\delta S = 0.4\%$) have the minimum misfit among all the methods (correction 1 ($\delta S = 1.2\%$), correction 3 ($\delta S = 1.3\%$)). Therefore, we apply travel time correction method 2 which is based on crust and upper mantle U.S. regional seismic velocity tomography model of *Schmandt and Lin* [2014] (later referred as SL14 correction) and travel time correction method 4 based on LLNL-G3Dv3 for $P$-waves [*Simmons et al.*, 2012] and LLNL-G3D-JPS for $S$-waves [*Simmons et al.*, 2015] (later referred as LLNL-G3D correction) to our observations in this study.

## 3.4 Synthetic Slowness Perturbations

In order to investigate the types of slowness anomalies caused by different seismic velocity structures, we compute synthetic seismograms for a series of hypothetical cases. We used the 2.5-D axi-symmetric finite difference algorithms PSVaxi (for $P$- and $SV$-waves) [*Thorne et al.*, 2013] and SHaxi (for $SH$-waves) [*Jahnke et al.*, 2008] to compute synthetic seismograms. These tests were calculated for a source depth of 500 km with station locations in the epicentral distance range 40° to 90° with a station spacing of 0.1°. Computations are valid down to dominant period of 3 sec for $P$-waves and 7 sec for $S$-waves. Synthetic traces were grouped into 2° epicentral distance bins and the relative travel time differences within a bin were calculated using the adaptive stacking method [*Rawlinson and Kennett*, 2004]. In the same manner as applied to the data, we calculated the slowness of each bin by fitting a regression line to the relative time shifts as a function of epicentral distance. Here, we defined the slowness perturbation as:

$$\delta S = (S_{syn} - S_{prd})/S_{prd} \tag{3.3}$$

where $\mathbf{S}_{syn}$ is synthetic slowness and $\mathbf{S}_{prd}$ is the predicted slowness value calculated from AK135 earth model. Finally, the slowness perturbations of each epicentral distance bin were plotted as a function of the turning depth to generate a slowness profile for each model. This allows us to determine potential slowness patterns that we may search for in real data.

### 3.4.1 Gradational Velocity Discontinuity

We first constructed models with a gradational decrease in seismic velocity. Models are constructed with velocity gradient zone centered at 1000 km above the CMB (turning depth is 1891 km). The $P$-wave velocity decreases from 0% to -2% inside the velocity gradient zone with the thickness of 100 km, 200 km, or 400 km. The velocity profiles for the three models and resulting slowness perturbations are shown in Figure 3.4a-b. The results show that the slowness perturbations start to increase in the vicinity of the discontinuity, then reach a maximum slowness perturbation of 7%. The slowness perturbations remain constant for over 300 km of turning depth and then drop to approximately 2% at a turning depth of 2400 km. The overall shapes of the slowness perturbations are identical for all three models, while thicker gradient zones lead to gentler slowness perturbation increases. For a 400 km thick gradient zone, the slowness anomaly is still observed.

In order to examine the effect of the magnitudes of the velocity perturbations, we generated three velocity models with -0.5%, -1%, and -2% velocity perturbations through a 400 km thick velocity gradient zone located from 1700 km depth to 2100 km depth (Figure 3.4c-d), for both $P$ and $S$-waves. Greater magnitudes of velocity perturbations lead to larger slowness perturbations for both $P$ and $S$-waves. For example, a $P$-wave velocity model with -2% velocity reduction results in a maximum slowness perturbation of 7% (blue dots in Figure 3.4d), while the model with the -0.5% velocity reduction results in a maximum slowness perturbation of 1% (red dots in Figure 3.4d). There is no significant difference in the magnitude of the slowness perturbations between $P$ and $S$-waves for the same velocity model.

### 3.4.2 Upper Mantle Receiver- and Source-side Velocity Anomalies

It is likely that we cannot remove all of the effects of crust and mantle velocity structures from our slowness observations with our travel time correction method. Thus, we are motivated to explore the effects of velocity heterogeneities close to the surface. We simulated three types of receiver-side anomalies with a 80 km thick, 2% increase (or decrease for Anomaly 3, see Figure 3.5) in seismic velocity located 100 km beneath the surface in the distance range of 60° to 70° (or 50° to 80° for Anomaly 2) (Figure 3.5a). Anomaly 1 and 2 are similar to what one might expect for a subducting slab. The three velocity anomalies cause slowness anomalies with a characteristic shape. The slowness perturbations become negative as the ray path approaches the left boundary of the fast velocity anomaly located at 60° (or 50° in Anomaly 2), then recovers to normal values as the ray path moves past the boundary and towards the center of the anomaly. When the ray path approaches the right boundary of the fast velocity anomaly at 70° (or 80° in Anomaly 2), the slowness perturbations becomes positive (Figure 3.5b-c). For Anomaly 3 which has a -2% velocity reduction beneath the receiver, we observed the same slowness perturbation pattern as for the fast velocity anomaly (Anomaly 1 and 2), but with opposite polarity of the shape of the slowness anomalies (Figure 3.5d). Slowness anomalies caused by receiver-side shallow velocity heterogeneities are strongly related to the position of the boundary of the heterogeneities (compare Anomaly 1 and 2). Furthermore, these slowness anomalies are caused by the change of the velocity gradient in the vicinity of the boundary of the velocity anomalies and are not a diffraction off the sharp boundary of the velocity anomaly for the following reasons: 1) different velocity perturbations near the boundary leads to opposite polarities of the slowness anomalies (compare Anomaly 1 and Anomaly 3). 2) We also generated a model with a fast velocity anomaly located beneath all the stations from 40° to 90°. We do not observe any slowness perturbation for this model. 3) We further examined the record section of synthetic seismograms and we are able to identify the diffracted arrivals. The amplitudes of the diffracted arrivals from the boundary are negligible and do not affect our slowness calculations. Compared with the slowness perturbations caused by lower mantle velocity gradient zone (Section 3.4.1), the slowness perturbations

caused by receiver-side shallow velocity anomalies are subtler (maximum slowness perturbation $\sim$ 2%). The width of the slowness anomalies zone ($\sim$200 km in turning depth) is also smaller than that caused by lower mantle velocity gradient zone (up to 500 km in turning depth). This is because the slowness perturbations caused by the shallow velocity heterogeneities are only sensitive to the boundary of the velocity anomaly and thus can only be observed when the ray path travels in the vicinity of the boundary. The magnitudes of the slowness perturbations are the same between $P$- ($\sim$2%) and $S$-wave ($\sim$2%) models.

The shape of the slowness perturbations for both $P$- and $S$-wave models are identical, with a shift to greater turning depth of approximately 100 km for the $P$-wave model. This is because the $P$- and $S$-waves have nearly identical ray paths in the upper mantle and thus experience the same slowness perturbation. However, the turning depth of the $S$-wave is about 100 km shallower than that of the $P$-wave, thus causing the apparent turning depth shift if we plot the slowness perturbations as a function of the turning depth. This feature can be used It may be to identify whether the slowness anomalies have a shallow origin.

It is also possible that velocity anomalies located beneath the source could contribute to slowness perturbations in our observations. Therefore, we tested four models with 100 km and 400 km thick low velocity anomalies (2% velocity reduction) or fast velocity anomalies (2% velocity increase) located beneath the source (Figure 3.6). We only observe slowness perturbations from the receivers located from 40° to 45° for the 400 km thick low or high velocity anomaly (Figure 3.6b-c). Yet, at these short epicentral distances the ray paths bottom inside the anomaly and thus do not solely represent source-side anomalies. No slowness perturbation can be observed for 100 km thick low or high velocity anomaly models, or at any other epicentral distances for the 400 km thick model. Similar to the results we concluded from the receiver-side shallow velocity heterogeneities, only the ray paths travel through the side edge of the velocity anomalies will lead to slowness perturbations. Since the seismic traces recorded by the receivers located from 40° to 90° travel almost vertically in the 500 km region beneath the source and share similar ray paths, the slowness perturbations caused by the velocity variations beneath 500 km of the source are negligible.

## 3.5 Results

We calculated slowness perturbations for a total of 59 $P$-wave and 47 $S$-wave events located along the North and Western Pacific Rim recorded by broadband seismic stations in North America. The ray paths of these events sample the area beneath the northern Pacific Ocean (35° N∼75° N, 140° E ∼ 100° W)(Figure 3.3). These slowness observations cover a large extent both spatially and with depth, thus we expect to observe spatial variations in our slowness measurements. Therefore, we grouped these slowness observations into clusters based on the turning-point locations of the ray paths using the k-means clustering method (Figure 3.7). K-means is one of the simplest unsupervised learning algorithms that groups data by setting a number of centroids as far as possible from each other, associating each data point to the nearest centroid and calculating new centroids recursively until no data point moves from cluster to cluster. In this study, we chose seven centroids because seven clusters lead to at least 50 slowness observations in each cluster, which will ensure we have enough slowness measurements to estimate the velocity structures in each cluster. For each cluster, we further used the k-means clustering to group the observations by depth, and then stacked the slowness observations in each depth range. In order to make sure we have enough slowness measurements ($> 10$) to be stacked in each depth range, the depth range we used in this study is between 35 km and 50 km. Finally, the stacked slowness perturbations for each depth range are plotted as a function of the turning depth for each cluster.

All our slowness observations, without travel time corrections, are shown in Figure 3.8 as a function of turning depth. For the complete data set, our slowness observations follow the predicted trend from the AK135 reference model, but with a significant amount of scatter. These scattered slowness values may be caused by (1) crust and upper mantle velocity heterogeneities, (2) errors in $P$- and $S$-wave arrival time picks, (3) errors in slowness calculation, and (4) lower mantle heterogeneities. The $S$-wave slowness observations are more scattered than that of the $P$-wave observations, and there is less coverage in the 1500 km to 1700 km depth range. The standard deviation of the slowness is 1.0234 for $P$-wave observations and 1.7994 for $S$-wave observations. The higher standard deviation of $S$-wave observations

may result from the larger uncertainties in picking the $S$-wave arrival times. We also looked at the standard deviations of the $P$- and $S$-wave slowness perturbations before and after travel time corrections. For $P$-wave slowness observations, the standard deviations are identical for noncorrected data (1.0234), SL14 corrected data (1.0236) and LLNL-G3D corrected data (1.0259). However, for $S$-wave slowness observations, the standard deviations of corrected data (1.6078 for SL14 corrected data, 1.4986 for LLNL-G3D corrected data) are less than that of the noncorrected data (1.7994). Therefore, the corrections we applied to $S$-wave travel times tend to reduce the scatter of the slowness values more than that of the $P$-wave observations. In the next sections, we explore the details of the slowness observations based on the individual clusters.

### 3.5.1 Cluster 1

In cluster 1, turning depths range from 1400 km to 1900 km for $P$-wave observations, and from 1000 km to 1600 km for $S$-wave observations (Figure 3.9). Because the turning depths of $P$- and $S$-waves are different for the same event-station pair, we do not have perfect overlap of our observation zone. For $P$-waves, we observe an increase in slowness perturbation in the depth range from 1400 km to 1900 km prior to applying the travel time corrections. This pattern is removed when we apply the SL14 correction. For LLNL-G3D corrected data, the slowness perturbation increases from -3% to 2% from 1400 km to 1600 km depth, then decreases from 2% to -1.5% from 1600 km to 1900 km. For $S$-waves, we observe the same slowness perturbation pattern as we observed from the $P$-wave for uncorrected data and LLNL-G3D corrected data. This pattern no longer exists if we apply the SL14 correction. For the uncorrected and LLNL-G3D corrected data, we observe similar slowness perturbation patterns for both $P$ and $S$-waves, but offset in turning depth (third row in Figure 3.1). This feature matches our synthetic test of slowness anomalies caused by receiver-side velocity heterogeneities (Figure 3.5). Therefore, the slowness perturbation in cluster 1 could be primarily caused by crust and upper mantle velocity heterogeneities on the receiver-side. SL14 corrected data can partially remove the heterogeneities, leaving slowness perturbations that appear more randomly distributed. Slowness anomalies

caused by lower mantle heterogeneities may be masked by the strong heterogeneities on the receiver side and thus may be difficult to detect in this region.

### 3.5.2 Cluster 2

In cluster 2, we examined the depth range from 900 km to 1500 km for both $P$ and $S$-waves (Figure 3.10). For $P$-wave observations, there is up to 4.5% slowness perturbation from 900 km to 1500 km after applying the SL14 correction, while the slowness perturbations for the noncorrected and LLNL corrected travel times appear randomly distributed. For $S$-wave observations, we see a steady increase in slowness perturbation ranging from -4% to 3% from 900 km to 1500 km depth in the uncorrected and LLNL-G3D corrected data. The magnitude of the slowness perturbation reduces to 2.5% after applying the SL14 correction, however a positive increase in slowness exists for the entire depth range. For both uncorrected $P$- and $S$-wave observations, we observe the increase in slowness from 900 km to 1300 km with no shift in turning depth between $P$ and $S$-waves. This increase in slowness still exists after applying the SL14 correction, but with lower magnitude $S$-wave slowness anomalies. Based on our synthetic slowness perturbations calculated from gradational velocity discontinuities (see Section 3.4.1), this slowness anomaly is consistent with a gradational velocity decrease centered at 1300 km depth with roughly 2% to 4% maximum velocity reduction. We do not suspect a shallow velocity heterogeneity, in this case, because the observed slowness pattern is not shifted in turning depth between $P$- and $S$-wave observations (See Section 3.4.2). In addition, the pattern exists over a wide depth range from 900 km to 1300 km, while slowness anomalies caused by shallow velocity heterogeneities seem to have a narrow range of $\sim$100 km (Figure 3.10).

### 3.5.3 Cluster 3

In cluster 3, we sample the turning depth range from 1100 km to 2500 km for both $P$ and $S$-waves (Figure 3.11). For $P$-waves, the slowness perturbations of uncorrected data creases from -2% to 1% as the turning depth increases from 1100 km to 1500km. There exists a clear "W" shape pattern in slowness from 1500 km to

2500 km depths. For $S$-waves, the slowness perturbation of uncorrected data follows the shape of the $P$-wave slowness perturbation from 1100 km to 2500 km, but shows a clear "V" shape instead of "W" shape from 1500 km to 2500 km. After applying the SL14 correction, we are able to resolve a much clearer slowness perturbation pattern with less scattering. The slowness perturbations of $P$-waves still have a "W" shaped pattern from 1300 km to 2200 km, while that of $S$-wave has a "V" shape pattern in the same depth range. The two arms of the "V" shaped $S$-wave slowness anomaly match the outside two arms of the "W" shaped $P$-wave slowness anomaly without any depth shifting, indicating the slowness anomaly is not likely caused by any remaining crust and upper mantle velocity anomalies after the travel time correction. Moreover, this slowness anomaly exists in a wide depth range (1100 km to 2000 km), while slowness anomalies caused by shallow velocity structures tend to exist in a narrower depth range (Figure 3.5). Therefore, the slowness anomalies shown in cluster 3 are likely the results of lower mantle velocity heterogeneities located from 1100 km to 2000 km. However, as noted, there is a significant difference between $P$ and $S$-wave slowness perturbations from 1500 km to 1900 km, indicating that either different $P$ and $S$-wave velocity structures exist in the cluster 3 region, or that perhaps the longer period $S$-waves are smoothing over the central bump in the "W" shaped anomaly observed in the $P$-waves.

After applying the LLNL-G3D travel time correction, the slowness perturbations of $P$-wave are reduced in magnitude from to 3% to 2%, but the "W" shaped slowness anomaly remain. For $S$-waves, the correction increases the magnitude of slowness perturbations up to 5%. Moreover, the depth range of the observations also gets shortened, because this travel time correction creates larger travel time residuals in each bin, which leads to fewer bins passing the standard deviation threshold test (see Section 2). Therefore, this travel time correction method resulted in less observation points. In this case, the $S$-wave travel time correction based on LLNL-G3D may not correct the shallow velocity structures as good as the SL14 model.

### 3.5.4 Cluster 4

In cluster 4 (Figure 3.12), the depth range we are able to sample is deeper than that in the previous clusters (depth range from 1900 km to 2700 km). We are unable to resolve any clear slowness perturbation patterns for either $P$ or $S$-waves, before or after travel time correction. The slowness of the $S$-waves has greater perturbations (up to 6%) than that of $P$-waves (up to 4%) and both travel time correction methods we applied do not reduce the scatter in the observations.

### 3.5.5 Cluster 5

In cluster 5 (Figure 3.13), no reliable $S$-wave slowness observation passes our data quality constraints. For $P$-waves, the depths we sampled ranges from 1000 km to 2500 km, while no clear slowness perturbation pattern can be identified, before or after travel time correction. We notice that in this region, most of our $P$-wave slowness observations($2\%to4\%$) are greater than the predictions calculated by AK135 model. The receivers in this cluster are mainly located at Alaska. Therefore, it is possible that the boundary of the complex subducting slab beneath Alaska is contributing to the positive slowness anomalies which are not completely being corrected by the SL14 and LLNL corrections. However, our synthetic tests of gradationally decreasing velocity (Section 3.4.1) show that constant positive slowness perturbations can also result from the ray paths traveling through a region with gradationally decreasing velocity. Therefore, we cannot rule out the possibility that there are velocity heterogeneities with gradually changing velocity in this area. $S$-wave slowness observations would be helpful to identify whether the observed slowness anomaly is caused by lower mantle or upper mantle velocity heterogeneities.

### 3.5.6 Cluster 6

In cluster 6, we are able to investigate the depth range from 1200 km to 2700 km for both $P$ and $S$-waves (Figure 3.14). In this region, the slowness perturbations after the SL14 correction are significantly different from the uncorrected slowness observations and LLNL-G3D corrected slowness observations. The discrepancy is mainly located from 1500 km to 2000 km, where SL14 correction introduces a significant decrease of

the slowness perturbation (slowness drops from 4% to -2% for $P$-waves, and from 6% to -3% for $S$-waves) while other observations show a relatively stable perturbation from -2% to 2%. For slowness perturbations after both corrections, the slowness perturbations of $S$-waves is shifted by about 100 km in depth compared with $P$-waves. However, this depth shift is not apparent in our original observations, which indicates the shift is caused by the crust and upper mantle travel time corrections. Therefore, the slowness perturbation patterns from 1500 km to 2500 km we observed from the corrected slowness values in this region are likely caused by the shallow structures that exist in the tomography models which may not be present in real crust and upper mantle.

### 3.5.7 Cluster 7

In cluster 7 (Figure 3.15), we investigate a region in close spatial proximity to cluster 6 and with similar depth ranges. Our observations in cluster 7 are similar to our observations in cluster 6, with distinct slowness perturbations indicating the travel time corrections we applied may have introduced these features. There is no clear evidence of any slowness anomaly with a lower mantle origin in cluster 7.

## 3.6 Discussion and Conclusions

We applied array processing techniques to 10 years of seismic data recorded by all available broadband seismic stations in North America from events located along the North and West Pacific Rim, to investigate the $P$- and $S$-wave slowness anomalies in the mantle. The results beneath North Pacific show significant regional variations of the slowness values. We identify slowness anomalies with the origin of lower mantle beneath cluster 2 and cluster 3 in the North Pacific. The slowness anomaly of cluster 2 (45° N $\sim$ 53° N, 135° W $\sim$ 150° W) is best explained by a lower mantle velocity gradient zone centered at 1300 km depth with -2% to -4% velocity reduction. The slowness anomaly beneath cluster 3 (50° N $\sim$ 70° N, 140° W $\sim$ 160° W) is likely caused by lower mantle low velocity heterogeneities located from 1100 km to 2000 km. The $P$- and $S$-wave velocity structures of this heterogeneity is possibly different in the depth range from 1500 km to 2000 km. We are unable to identify any lower mantle

slowness anomalies beneath cluster 6 and 7 because the slowness perturbations appear to be dominated by slowness perturbations caused by artificial velocity anomalies in the tomography models we used for travel time corrections.

### 3.6.1 The Importance of Accurate Crust and Mantle Travel Time Corrections

Resolving the fine-scale seismic velocity structures in the deep mantle is often challenging because of the low amplitudes of deep-mantle phases as well as interference between target phases and other mantle phases. Furthermore, crust and upper mantle heterogeneities along the ray path add another level of uncertainty to estimations of the deep mantle structures. The most common way to overcome this problem is by applying travel time corrections based on tomography models to remove the travel time anomalies caused by velocity perturbations in areas outside of the study zone. In this study we attempt to focus on the slowness anomalies caused by lower mantle velocity heterogeneities, while our slowness observations represent the accumulated slowness anomalies along the whole ray path. Therefore, we apply different kinds of travel time corrections to correct for the crust and upper mantle velocity structures as described in Section 3.3. However, as we observed from Section 3.5, the slowness perturbations after applying different travel time correction methods sometimes are distinct from each other, thus, the corrected results cannot be directly used to imply structures. The errors of travel time corrections arise from two aspects: 1) the tomography models, and 2) the travel time correction algorithms. Current 3-D tomography models are generated with different methods, different seismic phases, and different travel time arrival picks and picking methods. Ultimately, these models have some level of discrepancies between each other. In many efforts, choosing which model to use is a result of balancing between available resources and personal biases. *Ventosa and Romanowicz* [2015] discussed the importance of applying accurate travel time corrections for upper mantle heterogeneities when examining the CMB region with *PcP-P* differential travel times. In their study, they used a Japan event which sampled the CMB beneath the Gulf of Alaska, which was recorded by TA stations located in the central United States. They observed up to 2 sec *PcP-P* travel time

anomalies from the stations in the epicentral distance range from 65° to 70° which led them to suspect a fast velocity anomaly located from 600 km to 1500 km depth beneath North America. They applied upper mantle travel time corrections based on four different global tomography models (MIT-P08 [*Li et al.*, 2008], LLNL-G3Dv3[ *Simmons et al.*, 2012], SEMUCB-WM1 [*French and Romanowicz*, 2014], and S40RTS [*Ritsema et al.*, 2011]) to remove this anomaly. Only the LLNL-G3Dv3 model was able to reduce the *PcP-P* travel time anomaly caused by the fast mantle velocity heterogeneity, but it also introduced up to -2 sec of additional travel time anomaly which is absent in the original data for the stations from 70° to 75°. The other three models could partially reduce the *PcP-P* travel time anomaly but also introduced around 1 sec travel time perturbations at the other stations. In their case, the travel time residuals caused by the travel time corrections were as large as half of the observed travel time residual, which may lead to misinterpretations of the velocity structures. Moreover, none of the four models were able to completely remove the slab structure without introducing artificial travel time perturbations caused by some velocity heterogeneities present in the model but might be absent in real Earth. Currently there is no reliable way to evaluate which tomography model will provide the best travel time corrections, thus, we recommend interpretations based on a combination of original data and travel time corrected data based on various of tomography models.

The travel time correction algorithm can also bias the correction results and add extra uncertainties. Most of travel time correction algorithms use 1-D ray tracing method to estimate the ray path of target phase and then apply travel time correction based on the structures along this ray path. The main issue here is the predicted ray path fails to present the actual ray path through the 3-D tomography model. The differences between the predicted and actual ray path become hard to ignore if the ray encounters large-scale velocity heterogeneities such as Large Low Shear Velocity Provinces (LLSVPs) and slabs. Moreover, for computational efficiency, most of travel time algorithms discretize the original tomography model into cells, and then averages the velocity in each cell in order to calculate the travel time of the ray path in each

cell. Therefore, the final model used in the travel time correction algorithm may differ from the input tomography model.

In Section 3, we demonstrated that the errors caused by our travel time correction algorithm can be as large as 1.3% while most of our slowness perturbations fall in the range between 3.0% and 5.0%. In this study, we picked the two travel time correction methods that performed better than the other methods we tested. Then, instead of fully trusting the corrected results, we compared the results generated by uncorrected data and corrected data and used synthetic test results as a guide to identify if the slowness anomalies are likely caused by remnant, uncorrected shallow velocity heterogeneities or lower mantle structures.

### 3.6.2 Implications for Seismic Observations of Iron Spin Transition in the Mantle

The pressure induced iron spin transition was proposed as early as 1960s, and has been further demonstrated by experiments and calculations in the last 10 years [e.g., *Badro et al.*, 2003, 2004]. Ferropericlase and perovskite are the two most abundant iron-bearing minerals in the lower mantle and will undergo a high-spin to low-spin transition in the lower mantle. Mineral physics experiments confirmed ferropericlase undergoes a spin transition in the 50-70 Gpa (1200 km to 2000 km depth) range at room temperature [e.g., *Marquardt et al.*, 2009]. However, the effect of high temperature present in the lower mantle is to broaden spin transition zone, which may be as broad as 1000 km. The elastic properties of ferropericlase change smoothly and gradually in this transition zone [*Li et al.*, 2005]. Most lab experiments and first principle calculations conclude that this transition will lead to a very large softening of the bulk modulus across the transition zone, while the shear modulus remains unaltered [e.g., *Marquardt et al.*, 2009; *Yang et al.*, 2015]. Seismologically, this leads to a gradual decrease in $P$-wave velocity in a wide depth range located from 1000 km depth to 2000 km depth while $S$-wave velocity likely remains unchanged [*Cammarano et al.*, 2010]. However, seismological evidence of such an anomaly is elusive. The main difficulty of the detection of this anomaly comes from the fact that the $P$-wave velocity decreases gradually over a wide depth range, and thus, there is no

sharp velocity discontinuity to generate reflected or refracted seismic waves. Several studies have explored the possibility of seismically detecting the spin transition and have concluded that either the velocity perturbations caused by the spin transition are too small to be detected seismologically, or the density variations through the spin transition zone balance out the variations in the bulk modulus, thus leading to an imperceptible change of the seismic velocity [*Caracas et al.*, 2010; *Antonangeli et al.*, 2011].

In this study, we demonstrated that slowness perturbations are very sensitive to gradational changes in seismic velocity. In order to understand whether slowness perturbations can provide insights to the iron spin transition, we tested synthetic models with Gaussian shape velocity discontinuity (Figure 3.16). In these models, the velocity gradually decreases to the maximum velocity anomaly of -2% at 1000 km above the CMB and increases back to the original value in a velocity transition zone with the width of 100 km, 200 km, and 400 km, to simulate the velocity perturbations caused by the softening of the elastic moduli in the spin transition zone. The $P$-wave synthetic seismograms are computed for dominant period of 3 sec while the $S$-wave synthetics are computed with a dominant period of 7 sec. For $S$-waves, the slowness anomalies appear in a smaller range as the thickness of the velocity gradient zone increases. However, the amplitude of the slowness perturbations for these models, are almost constant, with a magnitude of approximately 2% (Figure 3.16b). For $P$-waves, the magnitude of the slowness anomalies increases with increasing width of the Gaussian function. In general, the slowness anomalies for the $S$-waves are subtler than that for $P$-waves, no matter how broad the Gaussian function is. Most likely this is because, the longer wavelengths of the $S$-waves are less sensitive to small, gradually changing velocity structures compared to the higher frequency $P$-waves. In general, one expects that the slowness perturbations caused by the spin transition should lead to a stronger slowness perturbation on $P$-waves than for $S$-waves because: (1) most of the mineral physics experiments agree that the elastic moduli softening is only significant for the bulk modulus; and (2) our synthetic tests indicate even for the same magnitude of velocity perturbations in the Gaussian shape velocity anomaly, the slowness perturbations for $S$-waves are likely less than that of the $P$-waves.

For $P$-wave, the magnitude of the slowness anomalies increases with increasing width of the Gaussian function (Figure 3.6). Therefore, the broader the Gaussian velocity anomaly is, the stronger the slowness perturbations should be. We computed synthetic seismograms for a $P$-wave model with a 800-km wide Gaussian shape velocity anomaly centered at 1900 km depth with maximum -2% velocity perturbations at its center (Figure 3.17). Our results show the 800-km wide Gaussian velocity anomaly will induce up to 4.5% $P$-wave slowness perturbations which is stronger than that of thinner Gaussian shape velocity anomalies (up to 4.2%). Therefore, if the spin transition causes a $P$-wave velocity perturbation in a wide depth range spreading out even 800 km in the mantle, the $P$-wave slowness perturbation should be strong enough to be observed with proper mantle corrections. On the other hand, if the Gaussian shape velocity anomaly is not significantly broad, then detecting the spin transition zone by identifying slowness perturbations may be challenging.

In our study, we observed two velocity anomalies beneath the North Pacific. The slowness anomaly of cluster 2 (45° N $\sim$ 53° N, -135° W $\sim$ 150° W) may be due to a lower mantle gradient in velocity centered at 1300 km depth with velocity perturbation of at least -2%. For SL14 corrected data, we observed a stronger $P$-wave slowness perturbation (from -2% to 5%) than that for $S$-waves (from -2.5% to 0%) (Figure 3.10). For all synthetic models we have tested, we only observe stronger $P$-wave slowness perturbations thant that of $S$-wave for Gaussian shaped velocity anomalies. Therefore, the slowness perturbation beneath cluster 2 is likely caused by iron spin transition. However, the same pattern of slowness anomalies does not appear in the uncorrected data or LLNL-G3D corrected data (Figure 3.10). Therefore, based on our current method, we cannot be certain if the discrepancy between the SL14 $P$- and $S$-wave slowness perturbations in cluster 2 is caused by the spin transition, or is related to under or overestimated $S$-wave velocities in the SL14 model. The slowness anomaly beneath cluster 3 (50° N $\sim$ 70° N, 140° W $\sim$ 160° W) is likely caused by lower mantle low velocity heterogeneities located from 1100 km to 2000 km. A discrepancy exists between the slowness perturbations of $P$ and $S$-wave from 1500 km to 2000 km, which could be due to the longer period nature of the $S$-wave. The $P$- and $S$-wave slowness perturbations caused by the same Gaussian shape velocity anomaly can be

significant different from each other (Figure 3.16), because of the complex velocity variations in this discontinuity. Therefore, a Gaussian shape velocity discontinuity in $P$-wave (or both $P$ and $S$-wave) beneath cluster 3 could also lead to the discrepancy between the the $P$- and $S$-wave slowness perturbations. We are unable to resolve any other mantle slowness anomalies beneath other areas because the strong crust and upper mantle velocity heterogeneities beneath the receivers appear to dominate the data. We noted the slowness perturbations of cluster 2 and cluster 3 are caused by velocity anomalies located at different depths. Because the formation of the spin transition zone is strongly related to iron-partitioning and temperature, it is reasonable to assume the spin transition zone may occur at different depths and be accompanied by different velocity variations in different regions. In order to confirm the existence of the spin transition zone one would likely expect that such slowness anomalies as shown here are observed globally. Because 1-D Earth models do not see a global low velocity layer in the deep mantle, a possible explanation is that the spin transition does occur at differing depths in different regions of the globe. This would necessarily make globally seismological detection of iron spin transition challenging. Nevertheless, a compelling argument could be made for detection of the spin transition if similar slowness anomalies are found in similar tectonic regions and are not related to obvious lower mantle structures such as LLSVP boundaries. In order to further explore the possibility of using slowness perturbations to identify iron spin transition in the mantle seismologically, accurate mantle corrections based on higher resolution mantle models is needed.

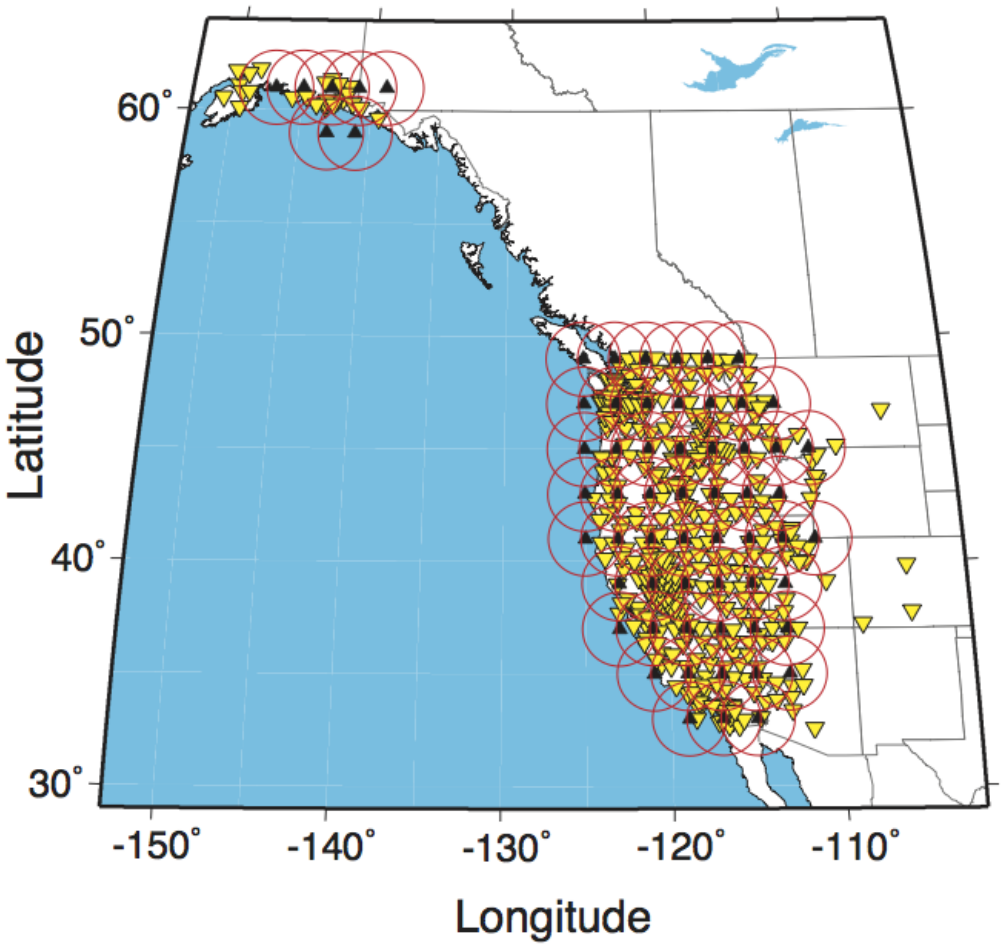


**Figure 3.1**. The distributions of stations (yellow inverted triangles) and geographic bin centers (black triangles) for the March 9, 2007 event (event ID: 200703090322). Stations are grouped into 2° radius geographic bins (red circles).

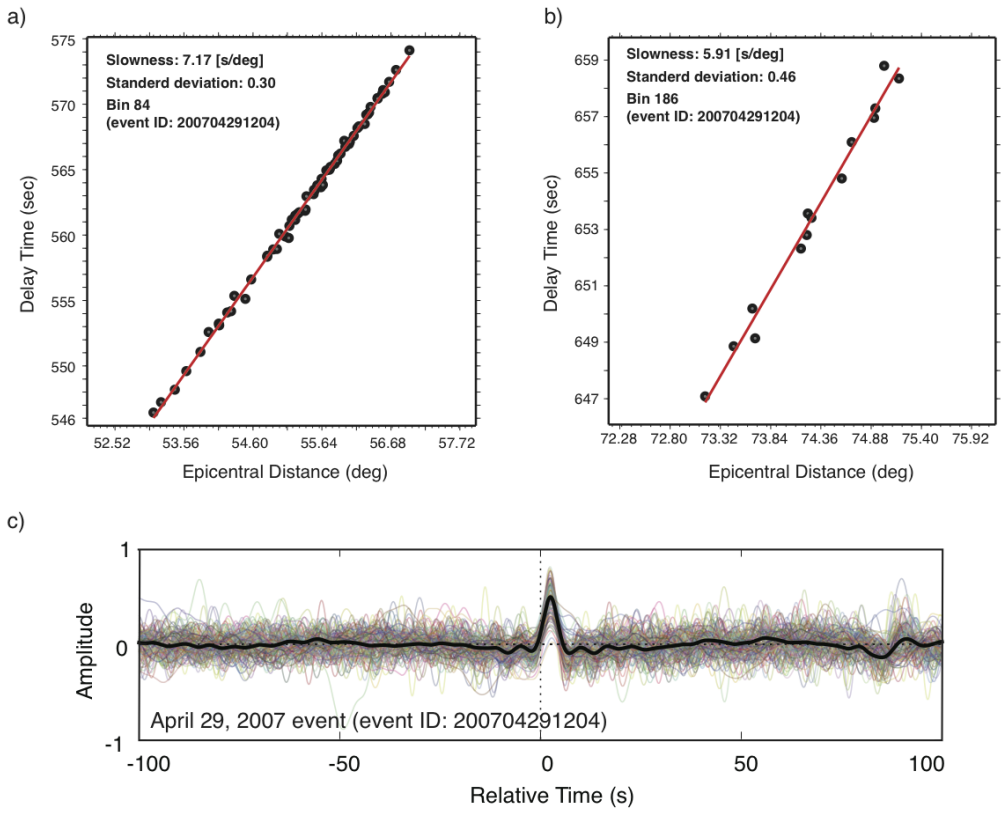


**Figure 3.2**. Example of an accepted (a) and a discarded (b) slowness value for the April 29, 2007 event (event ID: 200704291204). Each panel shows $P$-wave arrival time picks (gray circles) and the best-fit line (red line) from which the slowness is measured. c) Example vertical component displacement seismograms recorded by all stations for the same event. Seismograms are aligned based on the $P$-wave arrival time (0 sec) and the stacked trace is shown as the black line.

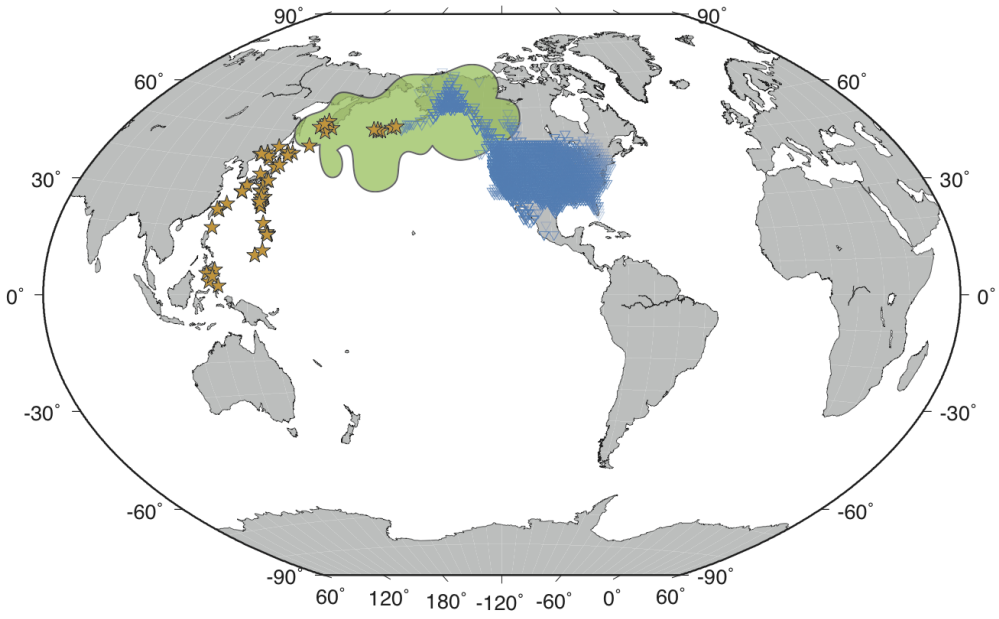


**Figure 3.3**. Events (orange stars) and stations (inverted blue triangles) are shown for our final data set. The turning points in the lower mantle are outlined by the green shaded zones.

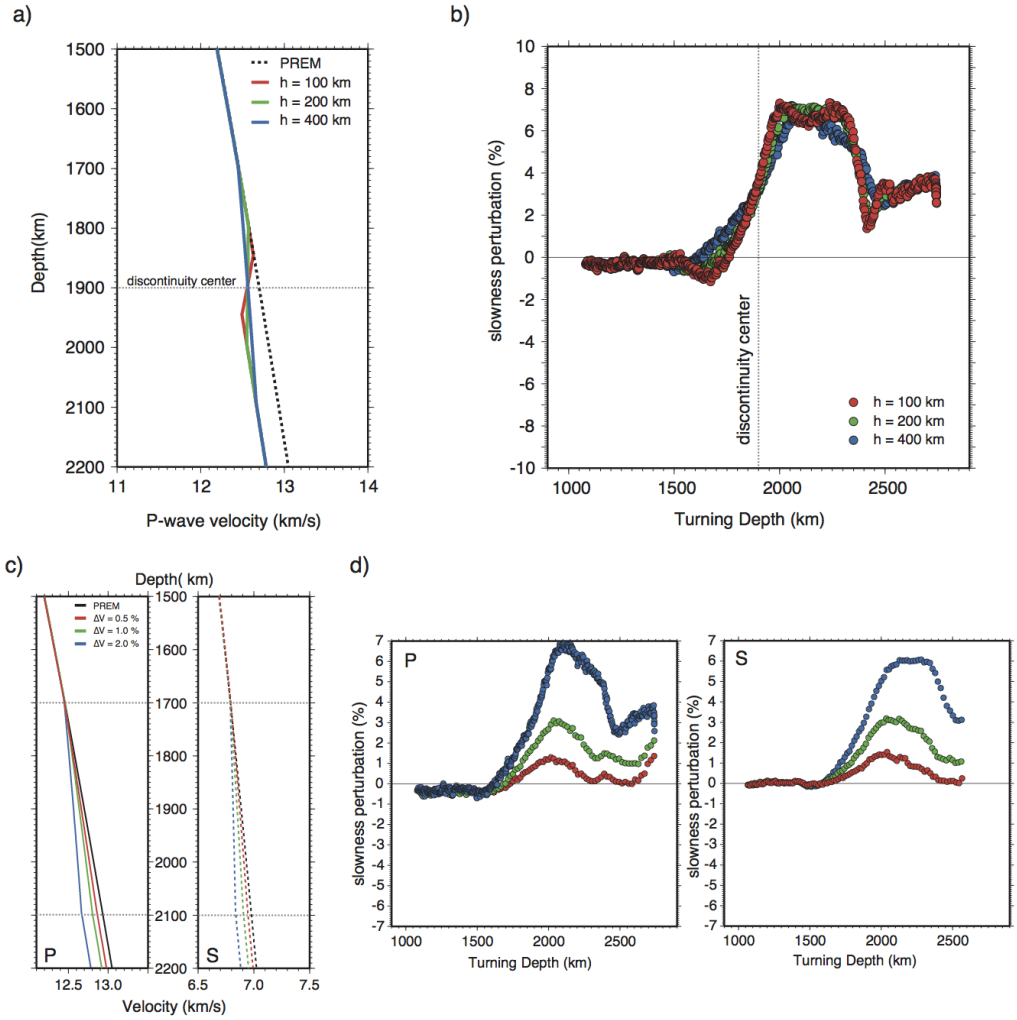


**Figure 3.4**. Velocity profiles and slowness perturbations for gradational velocity discontinuity. a) *P*-wave velocity models with 100-km (red), 200-km (green), and 400-km (blue) thick velocity gradient zone. *P*-wave velocity decreases to -2% and the discontinuity is centered at 1000 km above the CMB. b) The corresponding slowness perturbations as a function of turning depth. c) The velocity profiles of *P*- and *S*-wave gradually decreasing velocity discontinuity models with a 400-km thick velocity gradient zone. The maximum velocity perturbations are -0.5%(red), -1%(green), and -2%(blue). d) The corresponding slowness perturbations as a function of turning depths of *P*-wave (left) and *S*-wave (right) velocity models.

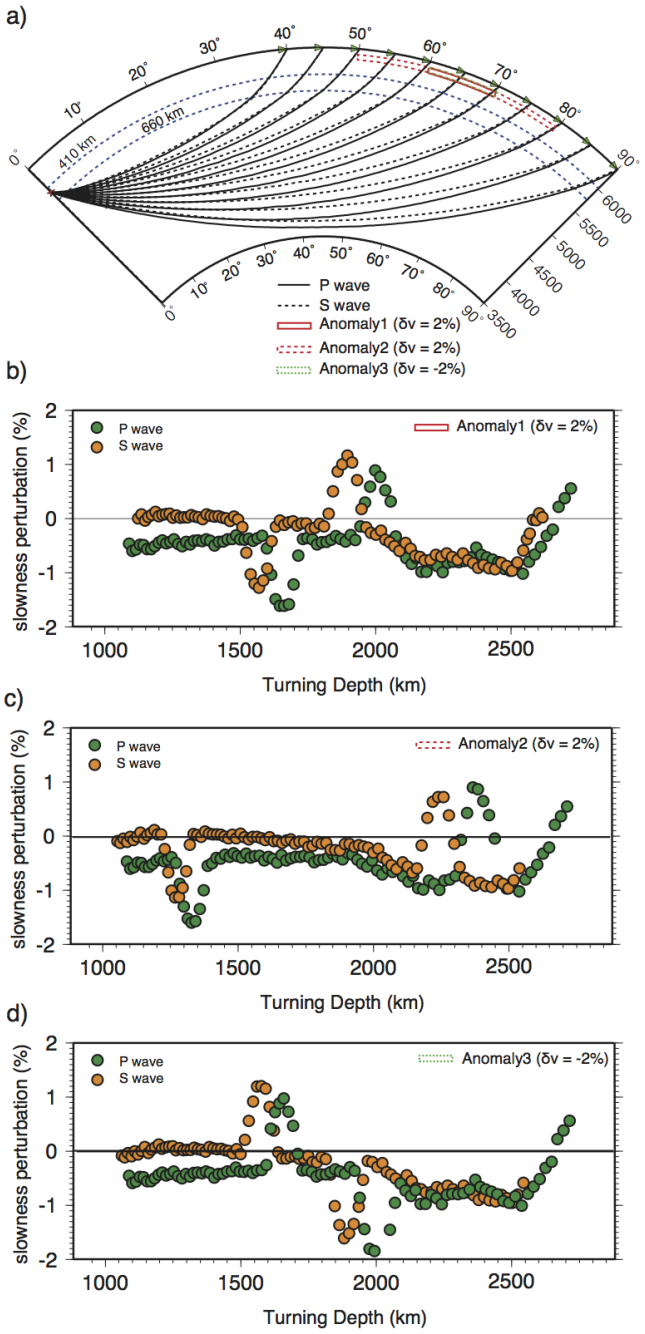


**Figure 3.5**. Velocity profiles and slowness perturbations for receiver-side velocity anomalies. a) Model cross-section and ray paths for $P$- and $S$-waves traveling through three kinds of velocity anomalies on the receiver side. The anomalies have a width of 80 km and the distance from the top of the anomaly to the surface is 100 km. Anomaly 1 and 3 have 2% (Anomaly 1) or -2% (Anomaly 3) velocity perturbation in $P$- or $S$-wave velocity in the distance range of 60° to 70°, Anomaly 2 has 2% increase in $P$- or $S$-wave velocity in the distance range of 50° to 80°. Slowness perturbations of Anomaly 1, Anomaly 2 and Anomaly 3 are shown in b), c) and d) for $P$- waves (green) and $S$-waves (orange).

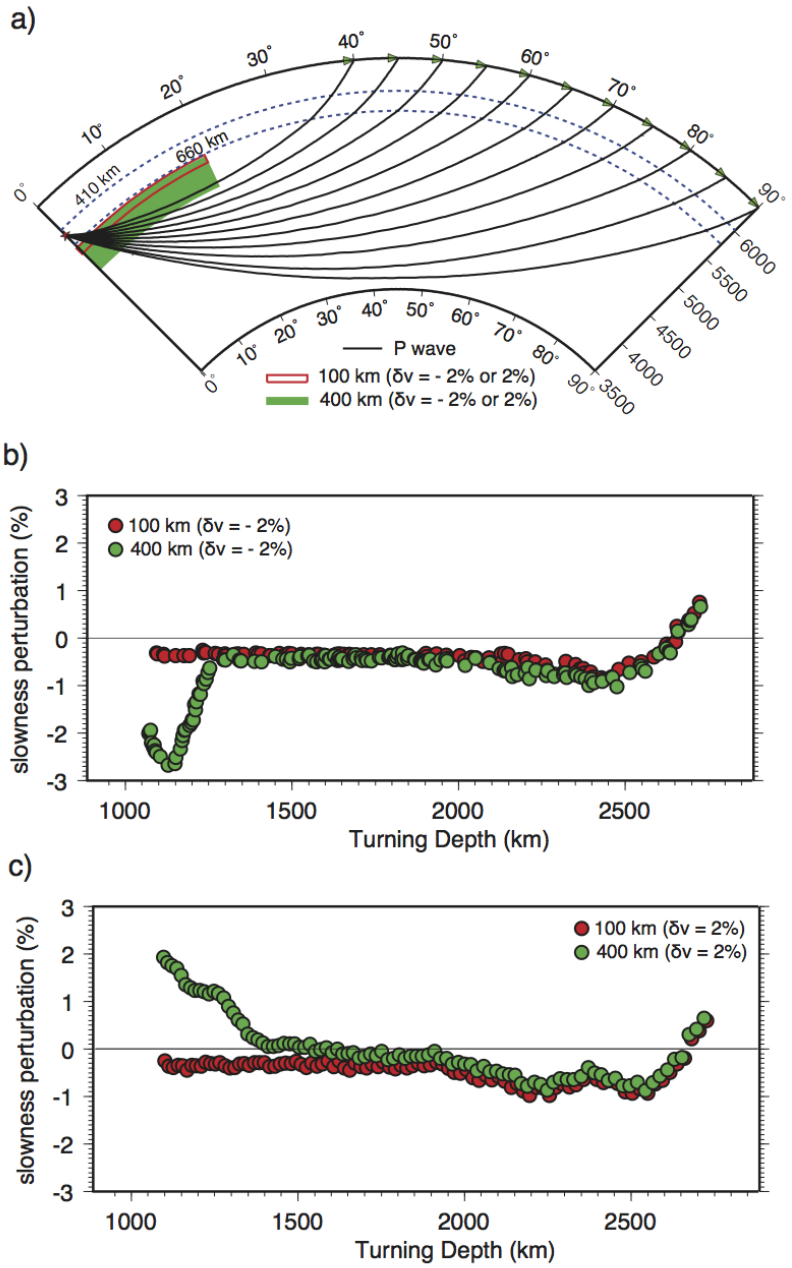


**Figure 3.6**. Velocity profiles and slowness perturbations for source-side velocity anomalies. a) Model cross-section and ray paths for *P*-wave traveling through four kinds of velocity anomalies on the source side. The anomalies have a width of 100 km or 400 km and the distance from the top of the anomaly to the surface is 700 km. Two anomalies are fast (b) and two anomalies are slow (c) in the distance range of 0° to 20°. Slowness perturbations of 100 km and 400 km thick slow velocity anomaly are shown in b) and slowness perturbations of fast velocity anomalies are shown in c).

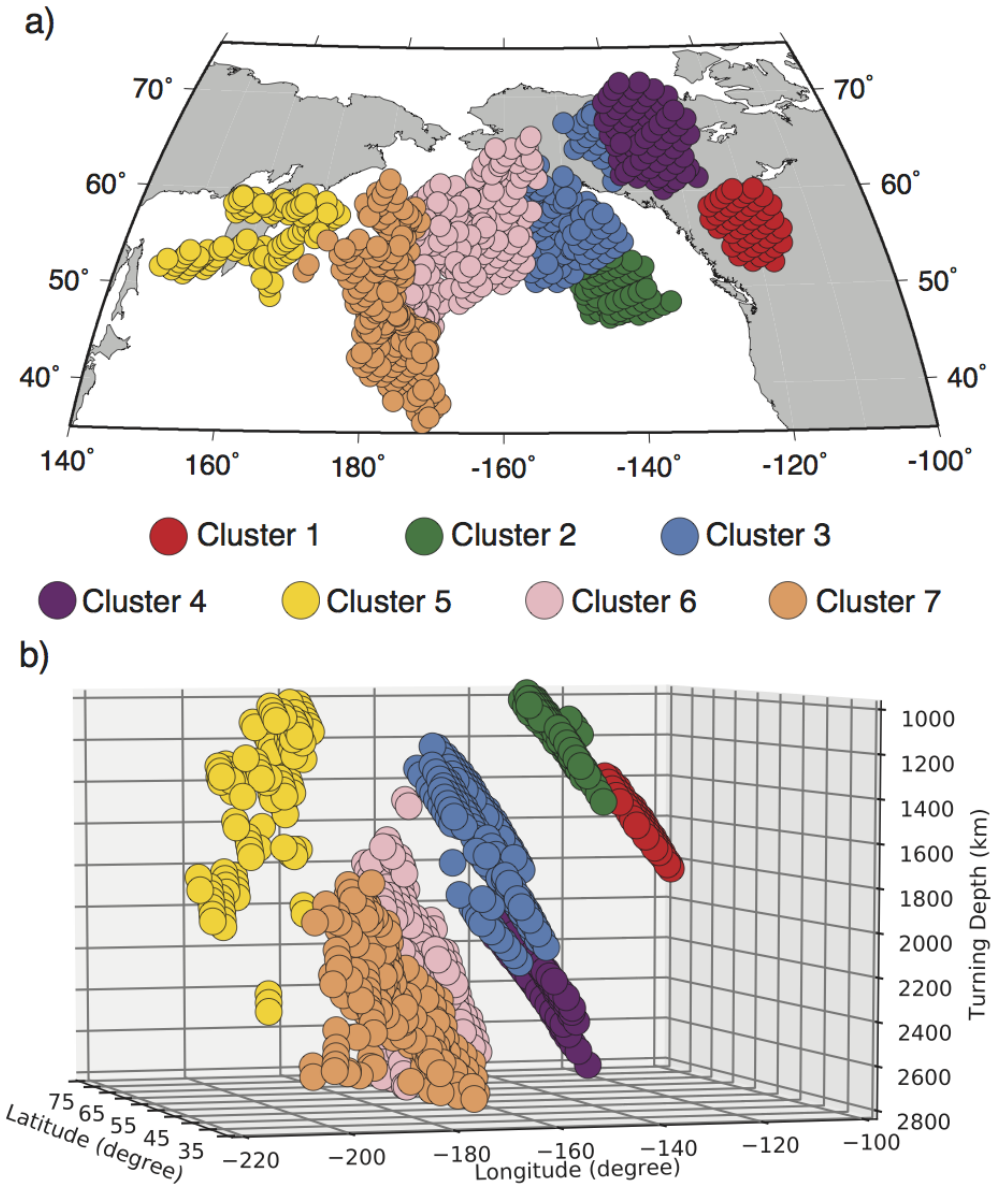


**Figure 3.7**. The locations of the turning points of the slowness observations. These observations are grouped to 7 clusters by k-means clustering method. a) shows the locations of the turning points on a 2-D map and b) shows the locations of the turning points as a function of turning depth.

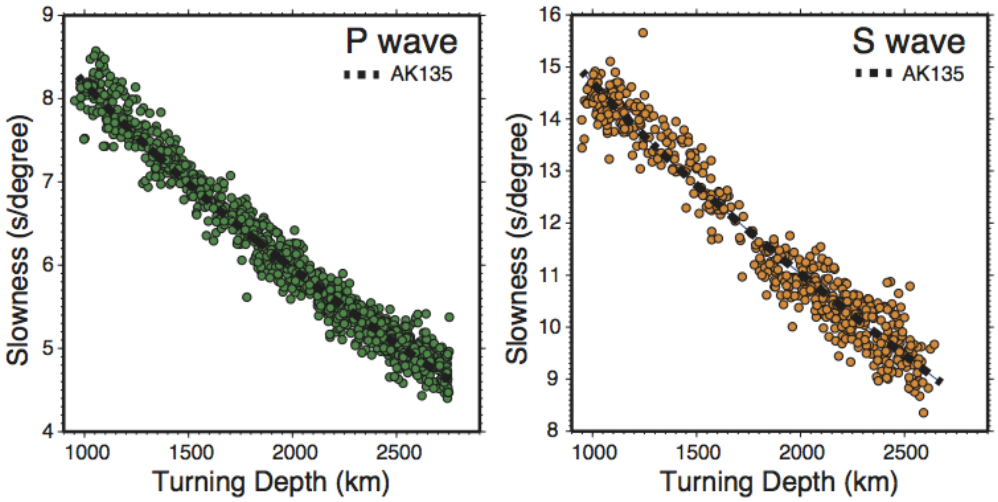


**Figure 3.8**. North Pacific slowness observations as a function of turning depth for all $P$-wave (left) and $S$-wave (right) measurements without travel time corrections.

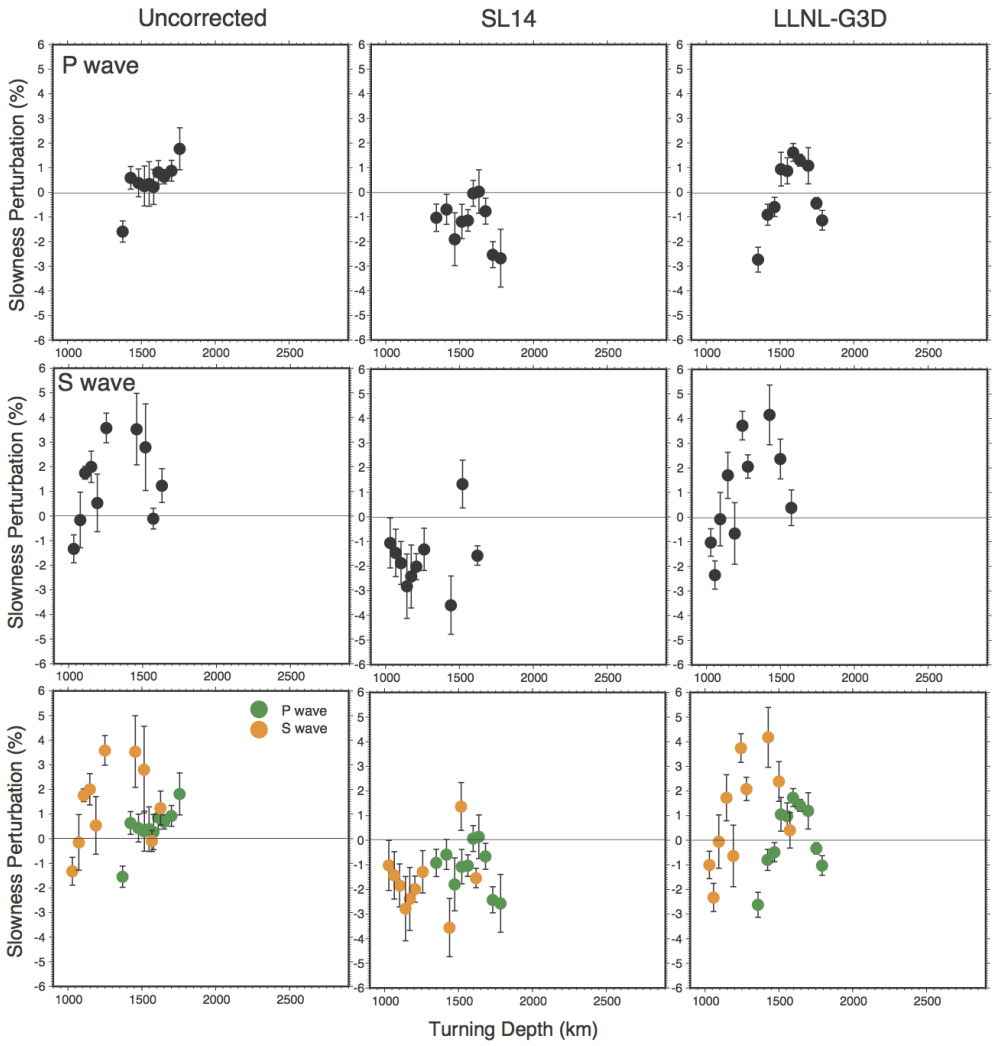


**Figure 3.9**. Slowness perturbations for cluster 1. Perturbations are calculated using the original travel time measurements (left column), travel times corrected using the SL14 tomography model for the U.S. regional crust and upper mantle (center column) and travel times corrected based on the LLNL-G3D global tomography model (right column). The top row shows the results for $P$-waves and the center row shows the result for $S$-waves. The bottom row overlays the slowness perturbations for both $P$- and $S$- waves.

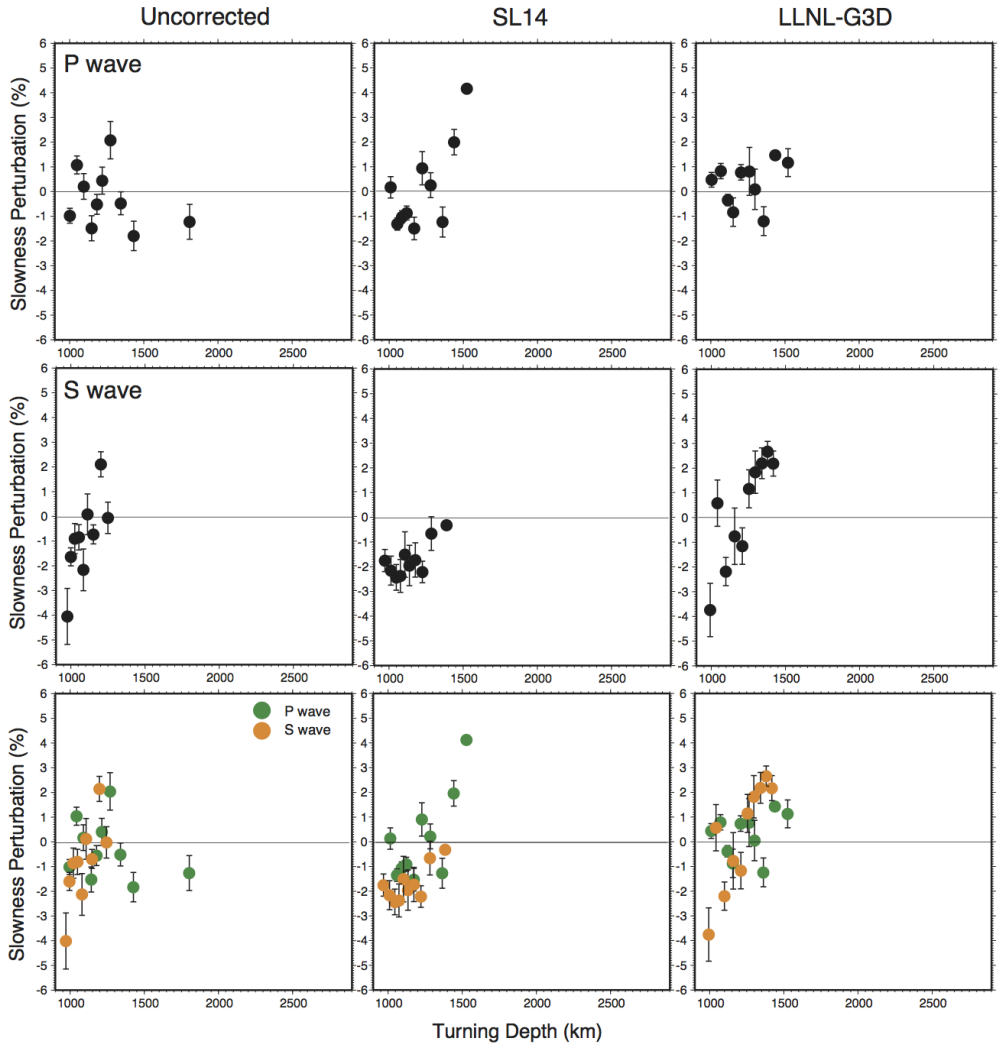


**Figure 3.10**. Slowness perturbations for cluster 2. Perturbations are calculated using the original travel time measurements (left column), travel times corrected using the SL14 tomography model for the U.S. regional crust and upper mantle (center column) and travel times corrected based on the LLNL-G3D global tomography model (right column). The top row shows the results for $P$-waves and the center row shows the result for $S$-waves. The bottom row overlays the slowness perturbation for both $P$- and $S$- waves.

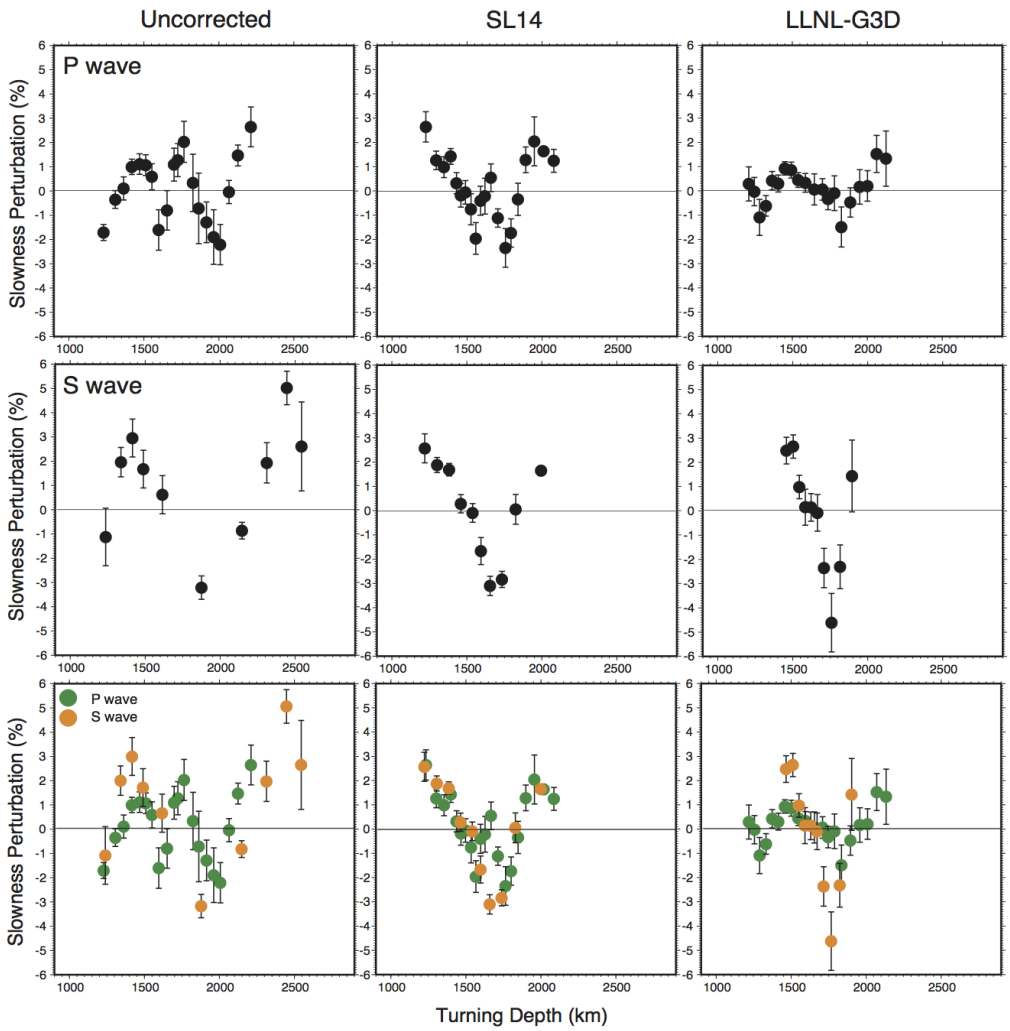


**Figure 3.11**. Slowness perturbations for cluster 3. Perturbations are calculated using the original travel time measurements (left column), travel times corrected using the SL14 tomography model for the U.S. regional crust and upper mantle (center column) and travel times corrected based on the LLNL-G3D global tomography model (right column). The top row shows the results for $P$-waves and the center row shows the result for $S$-waves. The bottom row overlays the slowness perturbations for both $P$- and $S$- waves.

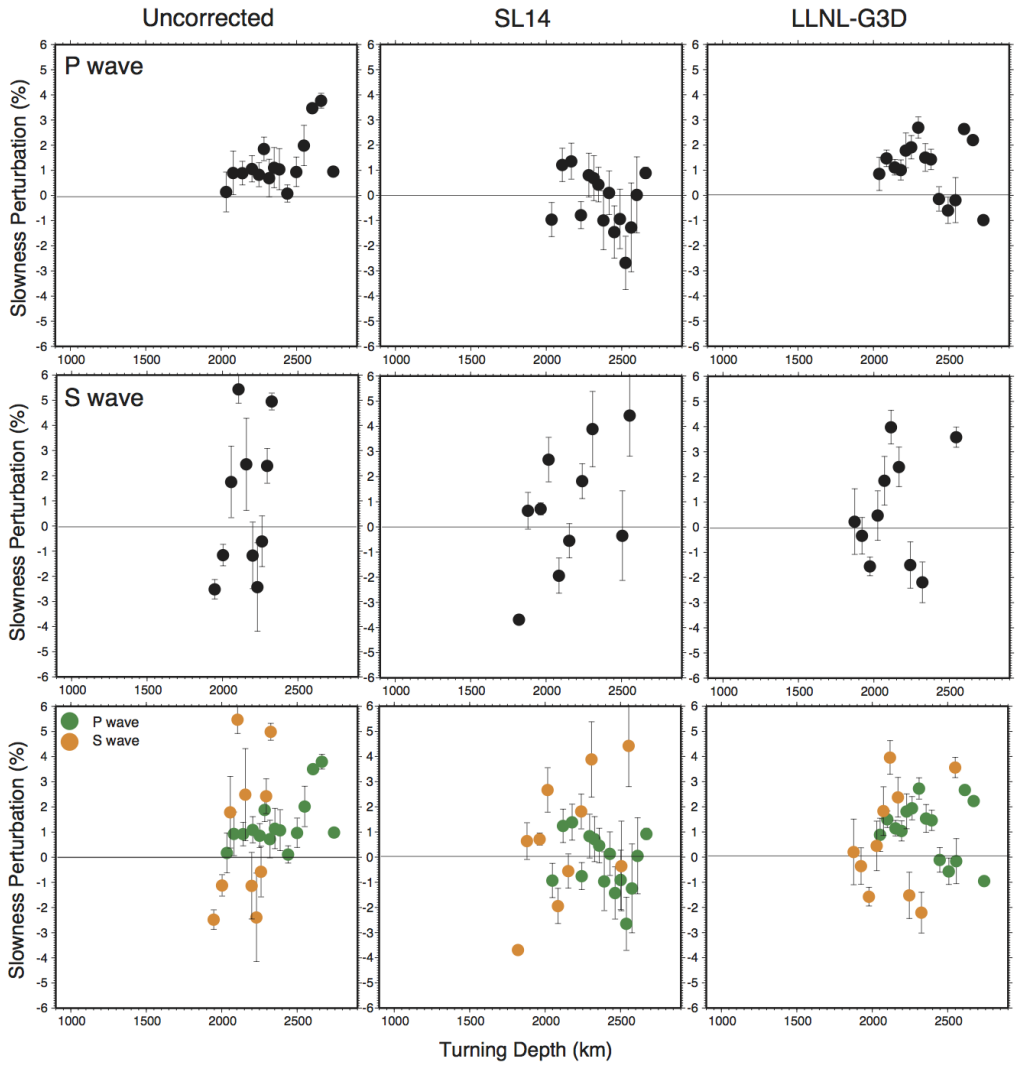


**Figure 3.12**. Slowness perturbations for cluster 4. Perturbations are calculated using the original travel time measurements (left column), travel times corrected using the SL14 tomography model for the U.S. regional crust and upper mantle (center column) and travel times corrected based on the LLNL-G3D global tomography model (right column). The top row shows the results for $P$-waves and the center row shows the result for $S$-waves. The bottom row overlays the slowness perturbations for both $P$- and $S$- waves.

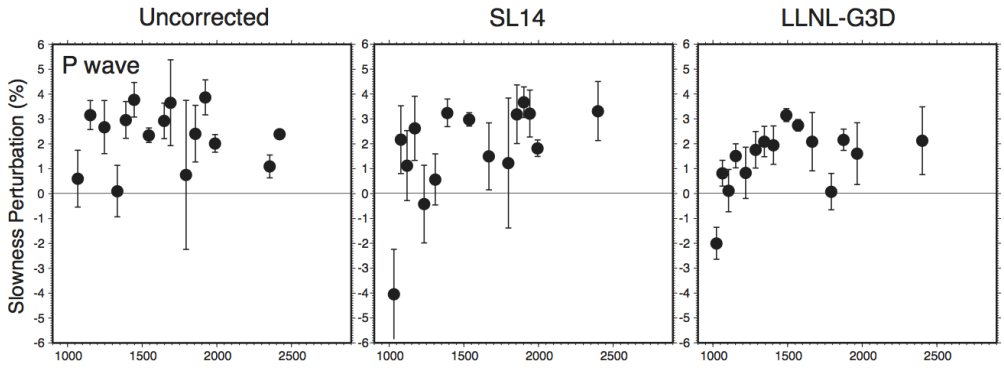


**Figure 3.13**. *P*-wave slowness perturbations for cluster 5. Perturbations are calculated using the original travel time measurements (left column), travel times corrected using the SL14 tomography model for the U.S. regional crust and upper mantle (center column) and travel times corrected with the LLNL-G3D global tomography model (right column).

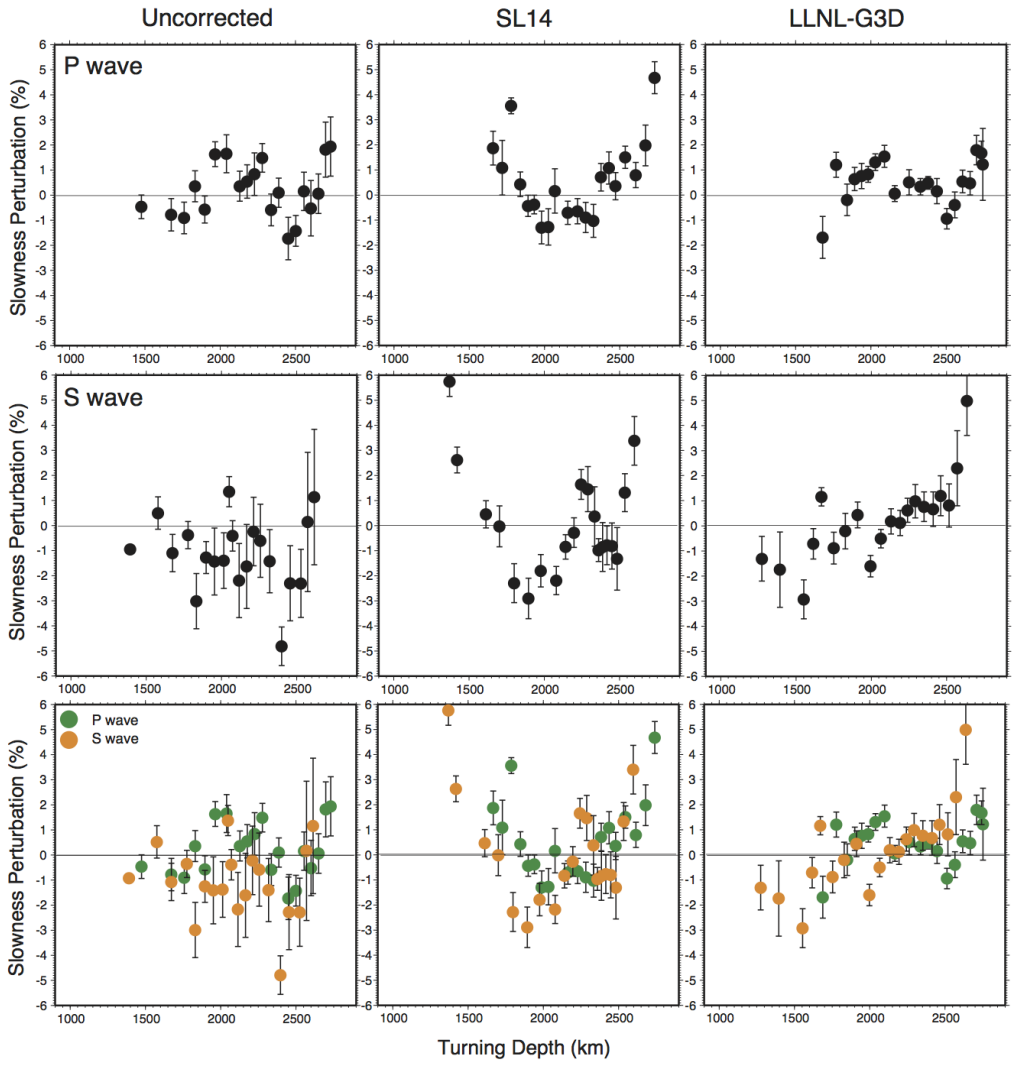


**Figure 3.14**. Slowness perturbations for cluster 6. Perturbations are calculated using the original travel time measurements (left column), travel times corrected using the SL14 tomography model for the U.S. regional crust and upper mantle (center column) and travel times corrected based on the LLNL-G3D global tomography model (right column). The top row shows the results for $P$-waves and the center row shows the result for $S$-waves. The bottom row overlays the slowness perturbations for both $P$- and $S$- waves.

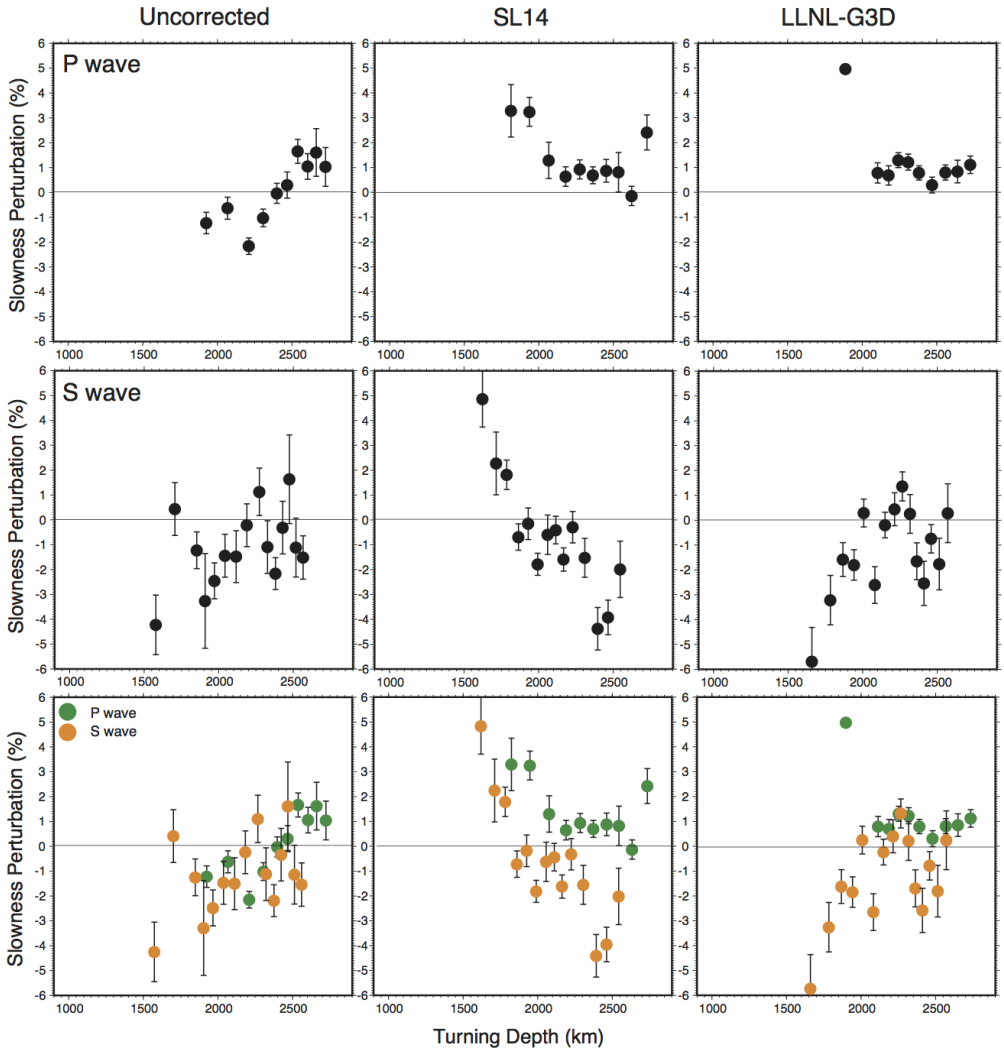


**Figure 3.15**. Slowness perturbations for cluster 7. Perturbations are calculated using the original travel time measurements (left column), travel times corrected using the SL14 tomography model for the U.*S*. regional crust and upper mantle (center column) and travel times corrected based on the LLNL-G3D global tomography model (right column). The top row shows the results for *P*-waves and the center row shows the result for *S*-waves. The bottom row overlays the slowness perturbations for both *P*- and *S*-waves.

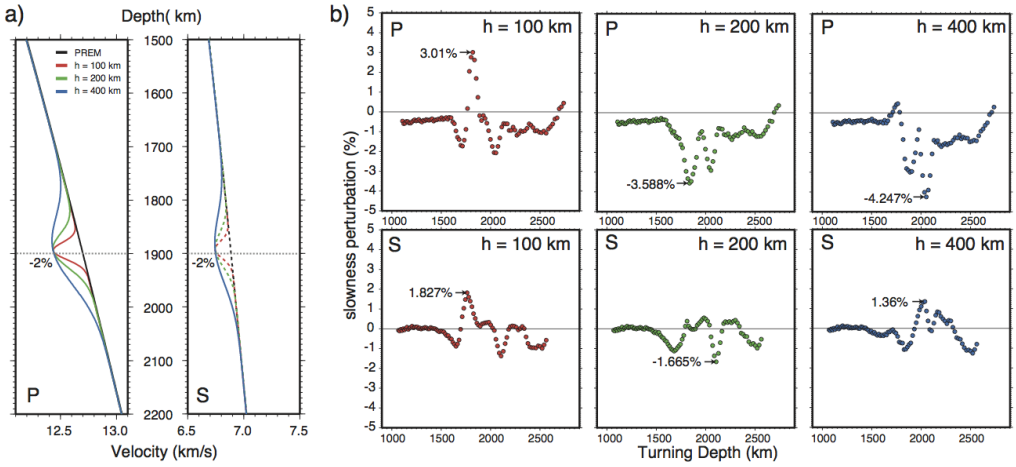


**Figure 3.16**. The velocity profiles of $P$- and $S$-wave velocity Gaussian shapes velocity discontinuity models. a) The velocity profiles of $P$- and $S$-wave velocity Gaussian shape discontinuity models. The width of the Gaussian anomaly is 100 km (red), 200 km (green) and 400 km (blue) thick. b) The corresponding slowness perturbations as a function of turning depths of $P$-wave (top row) and $S$-wave (bottom row) velocity models. Peak magnitudes of slowness anomalies values are indicatnoted by arrows.

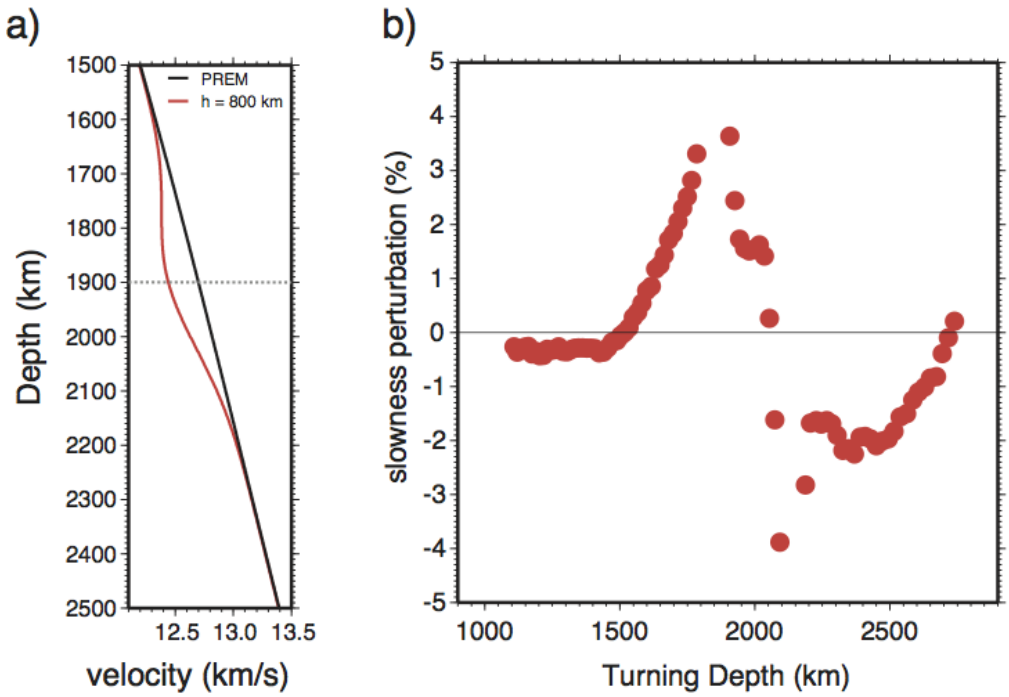


**Figure 3.17**. *P*-wave velocity profile and slowness perturbations of a Gaussian shaped velocity anomaly. a) *P*-wave velocity profile of a Gaussian shape velocity anomaly located at 1900 km depth with maximum velocity perturbation of 2%. b) The corresponding slowness perturbations as a function of turning depth.

# CHAPTER 4

# THE LUNAR SEISMIC WAVEFIELD

## 4.1 Introduction

From 1969 to 1977 a network of four seismic stations was established and operated on the Moon as a part of the Apollo Lunar Surface Experiments Package (ALSEP). Each station consisted of a long-period (15 sec resonant period) three-component seismometer collocated with a single short-period (1 sec resonant period) vertical component seismometer. Subsequent analyses of data recorded in this experiment have identified over 12,000 moonquakes. Roughly 7,355 of these events have been located, including 9 artificial impacts, 73 meteoroid impacts, and 28 shallow moonquakes [*Nakamura*, 2003]. The majority of identified events (7,245) were deep moonquakes occurring in clusters in the depth range from 559 to 1419 km [*Nakamura*, 2005]. A total of nine 1-D seismic velocity models were generated based on these data using a variety of techniques. In spite of the fact that these models were generated from the same data set, significant differences exist between them.

In a previous effort [*Yao*, 2013], we analyzed the various 1-D models of the Moon that have been previously proposed. Ultimately this led us to construct a 1-D average lunar model (referred as YY13) that explains travel times of direct $P$- and $S$-wave arrivals. In that work we computed synthetic seismograms for this 1-D average model. However, synthetic seismograms computed for this model do not appear similar to observed lunar seismograms because the long duration of the seismic coda inherent in lunar seismograms is not reproduced. Many previous studies have suggested that the long coda is generated by scattering in the lunar interior, yet only a few previous efforts have attempted to simulate the coda.

*Blanchette-Guertin et al.* [2012] conducted a systematic survey of the coda characteristics of impacts and moonquakes recorded at all four ASPE stations. They investigated the dependence of the coda decay time on source type, frequency, and

epicentral distance. For shallow moonquakes, the coda decay rates are closely related to the epicentral distance while the coda decay rates of deep moonquakes appear to be the same regardless of epicentral distances. Their results suggest that highly scattered media in a near-surface global layer (referred as the megaregolith) is the dominant source of scatterers that generate the coda observed in lunar seismograms. In order to study the effects of the megaregolith on the lunar seismic signals, they adapted the seismic phonon method [*Shearer and Earle*, 2004] to simulate the 3-D global scattering [*Blanchette-Guertin et al.*, 2015]. In this method, they track a large number of seismic phonons as they travel through the planetary interior and encounter 2.5D scattering heterogeneities in a Monte Carlo approach. They calculated the coda decay rates and risetimes from the synthetics generated from various models with megaregolith and/or whole mantle background scatterers for a surface impact (0 km) and deep moonquake (1000 km). The results show that a sharp contrast at the crust-mantle boundary, thin, very low velocity layer near the surface, or a discontinuity with sharp velocity gradient beneath the crust tend to trap and focus the seismic energy in the scattering layer near the surface, and will affect shallow events more than deep events. Moreover, low levels of seismic scattering in the lunar interior will contribute to longer seismic codas, resulting in increasing coda delay time with increasing epicentral distance. They suggested that the magnitude of the coda delay time is mainly controlled by the background velocity model and the shallow low velocity layer at the surface. The size-frequency distribution of the scatterers, thickness of the scattering layer, intrinsic attenuation Q, and impedance contrast at the scatterers play secondary roles.

In order to study the lunar seismic coda, *Yao* [2013] reprocessed a total of 85,466 moonquake traces and calculated the coda decay rate separately for shallow and deep events. They classified moonquakes as either (1) shallow events including artificial impacts, meteoroid impacts, and shallow moonquakes that occurred on or near the surface or (2) deep events that were defined as deep moonquakes. They generated smoothed envelope function for moonquake traces and stacked them in 10° epicentral distance bins for shallow and deep events, separately (for a description of the method, see *Yao*, 2013). Figure 4.1 shows the average behavior of the lunar seismic coda for

both shallow and deep events as a function of epicentral distance. In general, shallow events have relatively longer coda than deep events and the codas for deep events decay faster than shallow events. As the epicentral distance increases, the coda becomes longer for both shallow and deep events.

In this chapter, we first introduce synthetic seismograms for simplified versions of the lunar interior and describe the seismic phases that are observed in these models. Then we introduce a series of models that include random seismic velocity perturbations in the lunar crust and mantle in order to assess the effect of incorporating scattering into the simulations.

## 4.2 Synthetic Seismograms

To compute synthetic seismograms we have adapted two techniques commonly used in earthquake seismology. First, to investigate lunar seismic phases generated by 1-D lunar models we adapted the Green's Function of the Earth by Minor Integration (GEMINI) method [*Friederich and Dalkolmo*, 1995]. With this code we compute the full seismic wave field for 1-D radial models with dominant periods down to 10 sec. Although the recorded lunar data typically have dominant periods on the order of 1 sec, our goal was to first identify the major seismic arrivals inherent in these models, and second, to determine the primary differences in synthetics between these models and not necessarily try to model individual events.

In order to compute synthetic seismograms with the addition of seismic scatterers we explore SH-wave only simulations using the SHaxi [*Jahnke et al.*, 2008] technique. SHaxi is a 2.5-D axi-symmetric method based on high-order finite-differences. The code computes the seismic wave field on a 2-D grid which is virtually rotated about an axis of symmetry between the moonquake source and the center of the Moon. In this study, we compute seismograms down to periods of 2 sec, and through the virtual rotation retain the correct 3-D geometric spreading. We map 2-D random velocity heterogeneities into the models. The resulting synthetic seismograms can be used to compare with our observations and provide important insights about the position and thickness of the scattering layer.

Models of the lunar interior generally provide $P$- and $S$-wave velocities as a function of depth, but not all models provide density structure and/or quality factors (Q) which are needed to generate synthetic seismograms. Several studies have published density models [*Bills and Ferrari*, 1977; *Garcia et al.*, 2011; *Hood and Jones*, 1987; *Kuskov*, 1997; *Kuskov and Kronrod*, 1998; *Toksöz et al.*, 1974; *Weber et al.*, 2011], but the variation in these models is not large. Hence, we used average density values determined from these previous studies as: (1) crust: $\rho = 2.95\ g/cm^3$; mantle: $\rho = 3.41\ g/cm^3$; and core: $\rho = 6.51\ g/cm^3$. The effect of these densities on our synthetic seismograms does not affect the travel times but primarily affects the impedance contrast at the base of the crust.

We also constructed an average Q model for use in the GEMINI synthetics based on previous attenuation models [*Goins et al.*, 1981; *Nakamura et al.*, 1982; *Toksöz et al.*, 1974]. This model was also a three-layer model where we used the same Q for both $Q_S$ and $Q_P$: (1) crust: Q = 6000, (2) mantle: Q = 1500, and (3) core: Q = 500. We use a purely elastic computation for SHaxi synthetics and do not incorporate Q values into those models.

## 4.3 The VSM, SM, and 2LM Lunar Models

In order to explore the basic seismic phases observed for lunar seismic models, we generated synthetic seismograms for three simplified lunar seismic models: a very simple model (VSM) with only mantle and core; a simple lunar model (SM) with crust, mantle, and core; and a relatively complex model (2LM) with a two-layer crust, mantle, and core. Schematic illustrations of these models are shown in Figure 4.2.

We started with the very simple moon model (VSM) (Figure 4.2a). This simplified model has no crust and consists of only two constant-velocity layers ($V_S$ = 4.4 km/s and $\rho$ = 3.41 g/$cm^3$ from 0- to 1498-km and $V_S$ = 2.25 km/s and $\rho$ = 6.5 g/$cm^3$ from 1498- to 1738-km depth) representing the mantle and core of the Moon. In order to better understand the features of lunar seismograms we generated two sets of seismograms for a shallow source at 0.1 km depth and a deep source at 300 km depth. We also used the TauP Toolkit [*Crotwell et al.*, 1999] to calculate predicted

travel times of $S$-related phases and map them on the synthetic seismogrms. The synthetic seismograms generated by GEMINI for a 0.1 km depth source are shown in Figure 4.3. For the near surface source, the only arrivals observed are the direct $S$-wave and those arrivals associated with underside reflections. For example, after the direct arrival we note individual arrivals from *SS*, *SSS(S3)*, up to *S6*. After *S6*, the individual arrivals merge together to form the Love wave. Here we can see the generation of the Love wave due to the spherical boundary at the surface. The arrivals of different $S$-related waves shown in synthetic seismograms match with the predicted travel time calculated by TauP. For the synthetics computed for a 300 km deep source (Figure 4.4), in addition to the underside reflections we also observe the depth phase ($sS$) and subsequent underside-reflections such as *sSS* and *sSSS*. For the deep source, no surface wave is observed.

In our next step we added a layer of complexity and generated the simple moon model (SM) by adding a constant-velocity layer representing the crust into the VSM model (Figure 4.2b). The average velocities and density in the crust between the depth of 0 km and 60 km are set at $V_S = 3.3$ km/s and $\rho = 2.95$ g/$cm^3$. Compared with the synthetic seismograms of the VSM model, the synthetics of the SM model for a surface source shows a series of arrivals with significant large amplitude (the green lines shown in Figure 4.5) after the *S5* wave. These arrivals are consistent with multiple reflections inside the crust. Three phases are shown in Figure 4.5 marked by the predicted travel times. The *(Sv60S)6* phase, for example, is a down-going $S$-wave reflected from the top-side crust-mantle discoutinuty at depth 60 km for a total of 6 times. In the epicentral distance range from approximately 0° to 60°, we do not observe these mutiple reflections in the synthetic seismograms. This is due to the small amplitudes of these reflections at near off-set. When the angle of incidence for the seismic ray is greater than the critical angle (at an epicentral distance of 46.39°), total reflection occurs and the amplitude of the arrivals starts to increase. The reflected arrivals in the crust at near off-set have vanishingly small reflection coefficients as shown in Table 4.1, for distanes of 20°, 40°, and 60° degrees and for the seismic phases *(Sv60S)6*, *(Sv60S)7*, and *(Sv60S)10*. Figure 4.6 shows a zoomed-in image of three sections around these reflected arrivals. We assume a seismic ray

leaving the source with amplitude of 1, the amplitudes of *(Sv60S)6*, *(Sv60S)7*, and *(Sv60S)10* recevied at stations located at epicentral distance of 20°, 40°, and 60° are shown in Table 4.1. At 20°, the amplitudes of these arrivals are too small to be shown in synthetics. At 40°, *(Sv60S)6* and *(Sv60s)7* undergo total internal reflection so the amplitudes become larger and we begin to observe them in the synthetics. At 60°, all of three rays can be seen in the synthetics because they all undergo total reflection. In the epicentral distance range farther than 60°, this train of reflected waves trapped in the crust forms the surface wave with large amplitudes. The synthetic seismograms of the SM model for a deep source at 300 km depth become more complicated compared to the VSM model. Besides $S$ and mutiple $S$-waves, various $S$ reflections from the top- and bottom-side of the 60 km discontinuty are observed up (Figure 4.7). For reference we illustrate of the ray paths of three sections A, B, and C in Figure 4.7 are plotted in Figures 4.8-4.10.

Finally, we modified the crust in the SM model into two layers with $V_S$ = 2.27 km/s from 0- to 30-km depth and $V_S$ = 4.01 km/s from 30- to 60-km depth. Even though the velocity structure in the crust of the Moon is likely more complicated than that in this two-layer model (2LM), synthetic seismograms of the 2LM model indicate the changes in the seismograms along with the velocity changes in the crust. The synthetic seismograms (Figure 4.11) of the 2LM model at a 0.1 km depth source show a significant difference from the synthetics of the SM model, especially the arrival time of the mutiple reflections in the crust. In the 2LM model, the amplitudes of a series of *Sv60S* reflections become very smaller but the amplitudes of the series of *Sv30S* are much greater. In addtion, more reflected energys is observed in the 2LM model than in SM model. The space between the $S$-wave and *(Sv30S)6* is filled up by multiple $S$-waves and $S$ reflections on the top or bottom of the 30 km discontinuity. This train of reflected waves trapped in the first layer of the crust forms the surface wave with large amplitudes, silimar to the surface wave we observed from the SM model but with different phase velocities. This is due to the the difference in the seismic velocity of the crust of SM and 2LM models. For the synthetics of a source located at 300 km depth, however, only a small difference can be observed between the 2LM model and SM model (Figure 4.12). The reflections of the 30 km discontinuity in the 2LM

model take place of the reflections of the 60 km discontinuity in the SM model. The reflections of the 60 km discontinuity in 2LM model are still observed (yellow lines in Figure 4.12) but with a much smaller amplitude compared to the reflections in SM model.

Overall, synthetic seismograms of the simplied lunar velocity models VSM, SM and 2LM show distinct characteristics between each other and provide an understanding of the influence of the crust. The existence and layers of crust lead to stronger surface waves. However, these synthetic seismograms lack the long duration coda which should result from transmission of seismic enerygy within a poorly attentuating and highly scattering layer. In the next section, we investigate the effects of highly scattered velocity heterogeneties on the lunar seismic signals by inserting random distributed velocity heterogeneities into 1-D background lunar velocity models and generating synthetic seismograms.

## 4.4 The Scattering Models

The most notable feature of the lunar seismograms is the long duration of the lunar coda (see Figure 4.1). Here we compute synthetic seismograms where we incorporate the effects of seismic scattering into the computations. To construct models with random velocity perturbations we construct a velocity field such that:

$$V(s) = v_0 + \delta v(s) \tag{4.1}$$

where $\mathbf{V}(s)$ is the final velocity model, $\mathbf{v_0}$ is the mean velocity, $\delta v(s)$ are the perturbations to the mean velocity, and $\mathbf{s}$ is a location vector. Our initial assumption is that the velocity perturbations are a realization of some random process such that:

$$E\{\delta v(s)\} = 0 \tag{4.2}$$

where $\mathbf{E}$ represents the expectation operator. Furthermore, we require the perturbations to be Gaussian distributed. Previous studies have constructed the velocity perturbations by taking the convolution of a white noise process (e.g., *Frankel and Clayton*, 1986; *Baig and Dahlen*, 2004). This can be represented as:

$$V(s) = r(s) * k(s) \tag{4.3}$$

where $\mathbf{r}(s)$ is a white noise process (for example, randomly generated numbers), $\mathbf{k}(s)$ is the convolution kernel, and $*$ represents the convolution operator. For stationary random processes correlation functions are chosen for the convolution kernel as their Fourier Transform (FT) equals the power spectrum of the output random media (e.g., *Frankel and Clayton*, 1986; *Sato et al.*, 2012). For speed the convolution is performed in the FT domain. If we denote the FT by $\mathfrak{J}$, the construction of random velocity perturbations can be represented as:

$$V(s) = \mathfrak{J}^{-1}[\mathfrak{J}(r(s)) \times \mathfrak{J}(k(s))] \tag{4.4}$$

where $\times$ represents complex multiplication.

The FT based method uses correlation functions to statistically describe the spatial characteristics of the media (e.g., *Sato et al.*, 2012; *Frankel and Clayton*, 1986; *Ikelle et al.*, 1993). In this study, we use a von Karman (self-similar) type of correlation function which is defined in *Frankel and Clayton* [1986]:

$$N(r) = K_0(\frac{r}{a}) \tag{4.5}$$

where $\mathbf{K}_0$ is a modified Bessel function of $0^{th}$ order, $\mathbf{r}$ is the spatial lag and $\mathbf{a}$ is the auto-correlation length.

In this study we explore the effects of scattering based on the simple moon (SM) model using the SHaxi approach for computation of synthetic seismograms. Here, random velocity perturbations are applied to the $S$-wave field, and in some tests also applied to generate density perturbations. Our goal is to assess the effects of different scattering layers on lunar seismograms.

### 4.4.1 Shallow Moonquakes with Scatterers in the Crust

We first examine the effects of only adding scatterers to the crustal layer. Here we assess the effects of (1) changing the thickness of the crustal layer, (2) changing the auto-correlation length of the scatterers, and (3) adding density perturbations. Example stacks of seismograms are shown in Figure 4.13. In Figure 4.13a we show three examples where the thickness of the crustal scattering layer is set at either 1 km (yellow), 5 km (green), or 10 km (blue). In this case we use an extreme root-mean-square (RMS) velocity perturbation of 30% and fix the auto-correlation length at 1.3

km. The primary effect of adding scatterers to the crust is that we increase the coda in the time window between the direct $S$-wave and the onset of the surface waves. Additional scattered energy is also contained after the Love wave arrivals, but the duration of the surface wave arrivals is not strongly affected. Increasing the thickness of the crust tends to generate larger amplitude and slightly longer coda. However, the overall decay time of the coda is on the order of 100 sec, which is still far below the decay time in real lunar seismograms ($\sim$ 2500s). Furthermore, clear Love wave can still be observed from the synthetics, while surface waves are not clearly observed in real lunar seismograms.

Next we fixed the thickness of the crust at 10 km, and varied the autocorrelation length (Figure 4.13b). In general the effectiveness of the heterogeneities at scattering the wave field is related to the size of scatterers with respect to the wavelength of the seismic energy. Here we tested auto-correlation lengths of 1.3 km (yellow), 4.5 km (green), and 9.1 km (blue) (Figure 4.13b). An autocorrelation length of 4.5 km is similar to the wavelength of the direct $S$-wave. In these tests we observe an increase in coda duration for auto-correlation lengths of 4.5 km (1 wavelength) and 9.1 km (2 wavelengths) with respect to an auto-correlation length of 1.3 km (1/4 wavelength). That is, we maximize the scattering when the auto-correlation length of the scatterers are of the same spatial size as the wavelength of seismic energy. Moreover, we can only observe clear Love wave on the synthetics with 1.3 km auto-correlation length. The Love wave is covered by strong coda on the synthetics with 4.5 km and 9.1 km auto-correlation lengths, which is similar to our observations for the real lunar seismograms. At longer epicentral distance ($< 55°$), only the synthetics with 1.3 km auto-correlation length have an impulsive direct $S$-wave arrival. While on the synthetics with 4.5 km and 9.1 km auto-correlation lengths, the waveforms are characterized by longer rise times (time from initial $S$-wave arrival to maximum amplitude), which also matches our observations for real lunar seismograms. Increasing the auto-correlation length to larger wavelengths primarily introduces travel time variations as the velocity fluctuations increase in size beyond the wavelength of the seismic energy.

Finally, we introduced perturbations to the density. In this case we added 5% and 30% RMS density perturbations to an $S$-wave model with 30% RMS velocity fluctuations. The auto-correlation length is set at 4.5 km (1 wavelength). The spatial location of the density perturbations matches those of the $S$-wave perturbations. The results are compared with the case of no density perturbation in Figure 4.13c. In general, we only observe a slight increase in scattering intensity immediately after the direct $S$-wave arrivals, with almost no change in the coda decay rate.

In conclusion, the thickness of the crustal scattering layer plays an important role in controlling the length of the seismic coda after direct seismic arrivals. Having an auto-correlation length of the scatterers on the same scale as the wavelength of the seismic waves also introduce more scattering energy. The effects of the density perturbations of the scatterers, however, is relatively small.

### 4.4.2 Shallow Moonquakes with Mantle and Megaregolith Contributions

Because the addition of scatterers in the crust alone do not reproduce the long duration of the seismic coda observed, we also tested cases where we added scatterers to the mantle. First, we computed synthetics for a model where we included scatterers in the deep mantle at a radii range from 938-1238 km. Here we used an auto-correlation length of 8.8 km and 30% RMS $S$-wave velocity perturbations. A comparison between crust only scatterers (yellow; correlation length = 4.5 km, RMS = 30%) and mantle only scatterers (green) is shown in Figure 4.14a. In comparison to the crust only scattering model, the mantle scatterers generate coda in an extremely limited time window (e.g., at 85° epicentral distance, we only observe seismic coda between 300 and 600 sec). Virtually no coda is observed at the shortest epicentral distances. This is primarily controlled by the turning depth of the direct $S$-wave. In this case, the direct $S$-wave should first start to interact with the mantle scattering layer when its turning point reaches 500 km depth. This occurs at an epicentral distance of roughly 85°. However, a near insignificant amount of coda is observed behind the direct $S$-wave. Rather the largest amount of coda is observed after the onset of the surface waves. This is likely because the additional scattered energy

gets trapped in the crustal layer and can thus provide more energy into this layer. Nonetheless, the effect of a deep mantle only scattering layer is negligible.

If we combine scatterers in the crust and the mantle we do however gain some insights into possible mantle contributions to the lunar coda. Figure 4.14b shows two such examples with the source located at 0.1 km depth. The first model (yellow; Figure 4.14b) has a 10 km thick crust, with a 1.3 km auto-correlation length and 30% RMS velocity perturbations. In this case we include the deep mantle layer with scatterers located in radii from 938-1238 km. Here the mantle scatterers have 10% RMS $S$-wave velocity perturbations and a 22 km auto-correlation length. The second model (green; Figure 4.14b) has a 10 km thick crust, with a 4.5 km auto-correlation length and 30% RMS perturbations. In this case we have extended the mantle contributions to radii from 600 to 1728 km. Here we used a 30% RMS $S$-wave velocity perturbation and an 8.8 km auto-correlation length. We observed strong scattering effects for both models. The synthetics of the model with a thinner mantle scattering layer (yellow) show clear $S$-wave impulse arrivals and surface waves until the epicentral distance reaches 85°, where the ray path starts to interact with the mantle scattering layer. This result indicates the existence of the mantle scattering layer plays an important role in blending the sharp $S$-wave arrivals. On the other hand, the synthetics for the model with a thicker mantle scattering layer (green) show extremely long rise time and coda decay time. The surface wave is completely covered by the strong coda of the $S$-wave. The rise time can be as long as 1200 sec in this extreme case, which is much longer than our observations ($\sim$800 sec, Figure 4.16). Comparing the synthetics for the two models, the deep mantle scattering layer contributes to smoothing over the $S$-wave impulse arrivals and is able to mask the signal of the surface wave.

Finally we add an additional 1-km thick layer thin low-velocity layer with the $S$-wave velocity of 0.5 km/s at the surface to simulate the megaregolith on the Moon. We add this layer to a crust only scattering model (10 km thick crust, 30% RMS velocity perturbations and 4.5 km auto-correlation length) and compare this new model (green in Figure 4.14c) with a model without megaregolith (yellow in Figure 4.14c). Our results indicate the addition of this regolith layer primarily affects the

coda duration at the shortest epicentral distances, which is in contrast with our observations of the real lunar seismograms, where we observed increasing coda delay time with increasing epicentral distance.

In conclusion, our synthetic tests show: 1) Shallow scattering layer near the crust is crucial to the long duration coda of moonquakes (Figure 4.15a); 2) Some deep scattering in the mantle is likely necessary to explain the masking of the first arrivals and surface waves in real lunar seismograms. 3) The effects of a megaregolith on the surface of the moon is of secondary importance on the lunar seismograms.

### 4.4.3 Deep Moonquakes

In real lunar seismic observations, we observed long rise time and long coda decay time for both shallow and deep events. There is not a large difference of the duration of the risetime and coda decay time between the shallow and deep events. Thus, we tested two models with the source located at 900 km to study the scattering effects on the deep moonquakes.

We computed synthetics for a model with a crustal scattering layer (10 km thick crust, 30% RMS velocity perturbations and 4.5 km autocorrelation length; Yellow in Figure 4.15). We also tested a model with 1 km thick megaregolith (green in Figure 4.15) to study the effects of the megaregolith on deep moonquakes. The results show sharp $S$-wave arrivals for both models, which is not consistent with the long rise times observed in the lunar seismograms. The model with regolith tends to create greater amplitudes of the coda, however this might be caused by the amplitude normalization in the data processing step. We normalized the amplitudes of the synthetic traces according to the maximum amplitude in the trace before we calculated the smoothed envelope. Therefore, for the traces where the amplitude of the $S$-wave arrival is the maximum amplitude arrival (e.g., traces at 15° to 115° in Figure 4.15), the amplitude of the trace is normalized based on the $S$-wave arrival. For the model with megaregolith, the amplitude of the $S$-wave arrival will be reduced because the extra low velocity layer on the surface. Therefore, the amplitude of the coda will be enhanced after the amplitude normalization.

## 4.5 Discussion and Conclusions

In this study, we investigated synthetic seismograms for three simplified lunar seismic models: a very simple model (VSM) with only mantle and core; a simple lunar model (SM) with crust, mantle, and core; and a relatively complex model (2LM) with a two-layer crust, mantle and core. Overall, synthetic seismograms of the simplied lunar velocity models show distinct characteristics from each other and provide an understanding of the influence of the crust. All three models with a surface source produce large amplitude surface waves, which are not clearly observed in the real lunar seismograms. Even though the origins of the surface wave are different in each model (multiple $S$-waves for VSM model, multiple reflections in the crust for SM model, multiple relfections in the first layer of the crust for 2LM model), our tests indicate we should be able to observe a surface wave on lunar seismograms. However, no clear surface wave can be identified on real lunar seismograms for shallow events. It is generally believed the surface wave is masked by the long duration coda following the $P$ and $S$-waves for shallow events. If this is the case, then the argument that crustal scattering layer controls longer coda observed from shallow events need to be reconsidered. The moonquake is characterized with long risetime, which defined as the time from the $P$ or $S$ arrivals to the maximum amplitude of the seismic traces. Previous studies have demonstrated that the rise time and coda of shallow events are longer than that of deep events (e.g., Figure 4.16 adapted from *Yao*, 2013). This observation has been used to demonstrate that most of the scatterers are located near the crust, because the longer rise time and coda of shallow events is caused by more portion of the ray path traveling through the crust scattering layer. However, it is also possible that the surface waves of the shallow events will contribute to the extra long rise time and coda. An extreme case will be if the lunar interior is equally heterogeneous everywhere, then for both shallow and deep moonquakes, we will observe equally amounts of coda caused by scattering. However, we will still see longer rise time, longer coda on shallow events because of the presence of surface wave on shallow events. Therefore, the long risetime and coda on shallow events can not be directly linked to the existence of the surface scattering layer. It is possible that the lunar mantle is highly scattering as well.

We further simulated the seismic coda by adding random velocity perturbations into our models using a Fourier Transform based method. We choose the simple moon (SM) model as the background model and applied small-scale randomly distributed velocity/density heterogeneity inside this model. The random distribution is controlled by a self-similar auto-correlation function (ACF). We modified the position of the scattering layer (crust or mantle), the thickness of the scattering layer, and the auto-correlation length of the scattering media. Our main observations are: 1) A shallow scattering layer near the crust is crucial to the long duration coda of moonquakes; 2) Some deep scattering in the mantle is likely necessary to explain the masking of first arrivals and surface waves in real lunar seismograms. 3) The effects of a megaregolith layer on the surface of the moon only adds minor additional scattering. 4) A crustal scattering layer by itself is not sufficient to create the long rise time we observed from either shallow or deep moonquakes. 5) Deep moonquakes are inefficient at generating surface waves.

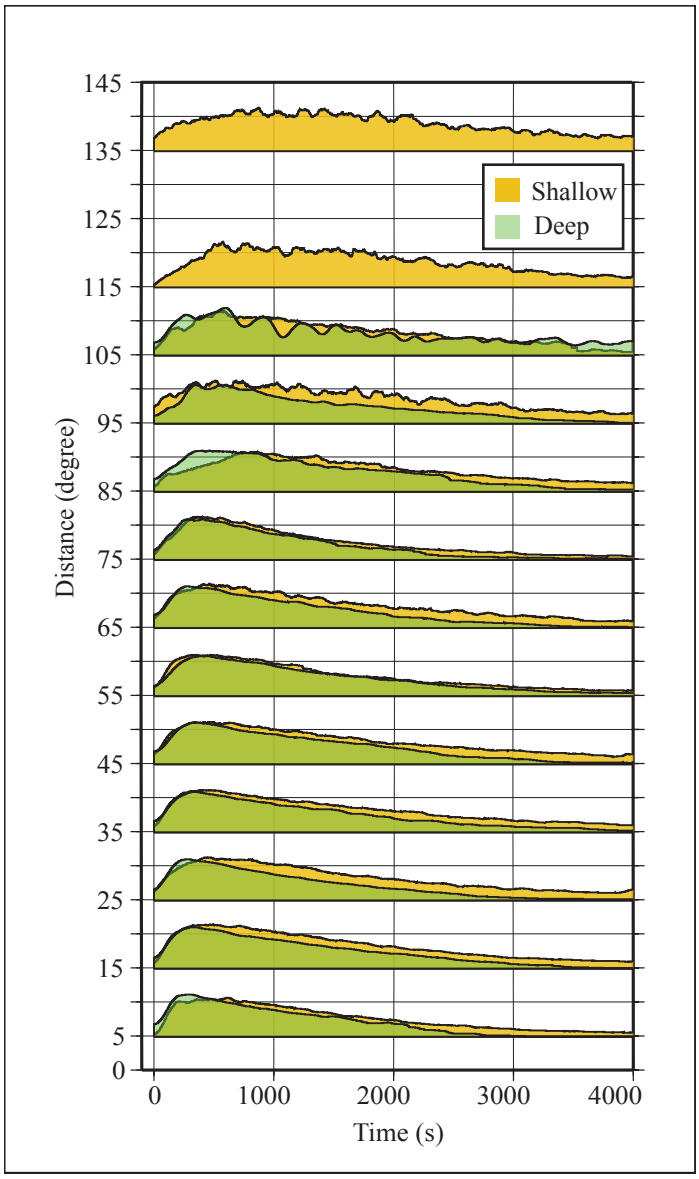


**Figure 4.1**. The smoothed envelope function of moonquake coda for shallow events (yellow) and deep events (green).

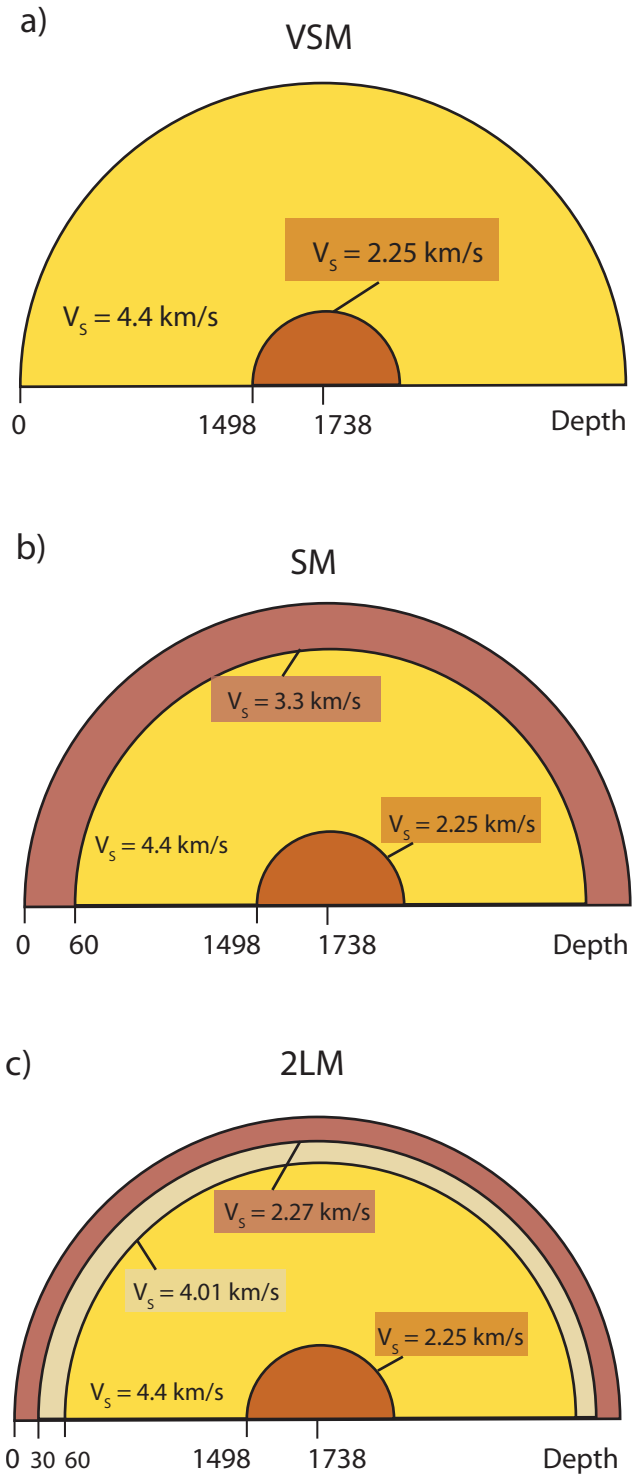


**Figure 4.2**. Schematic illustrations of VSM, SM, and 2LM lunar model

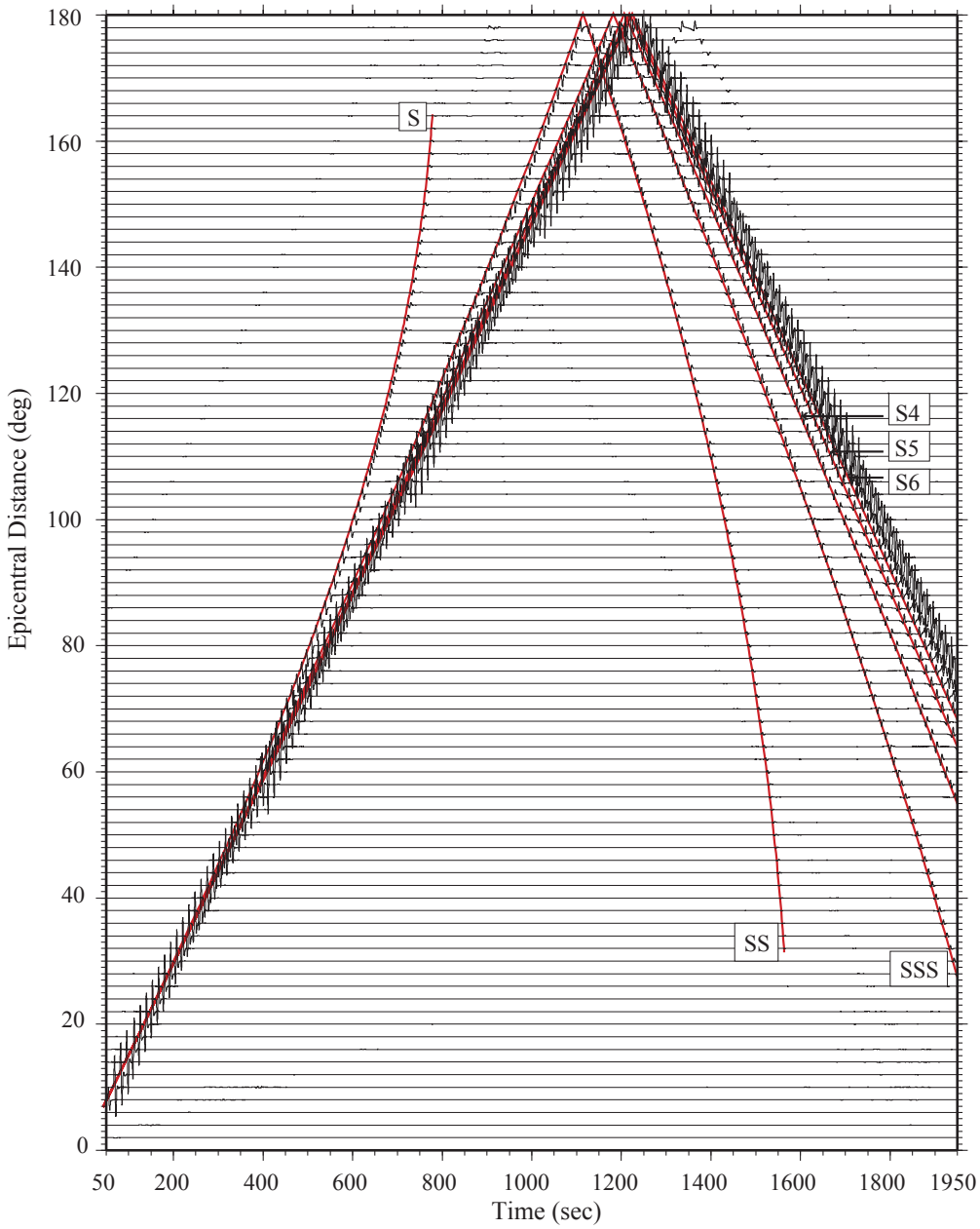


**Figure 4.3**. Synthetic seismograms of the VSM model generated by GEMINI. The source depth is 0.1 km. Phase arrivals are marked based on the travel times calculated by TauP

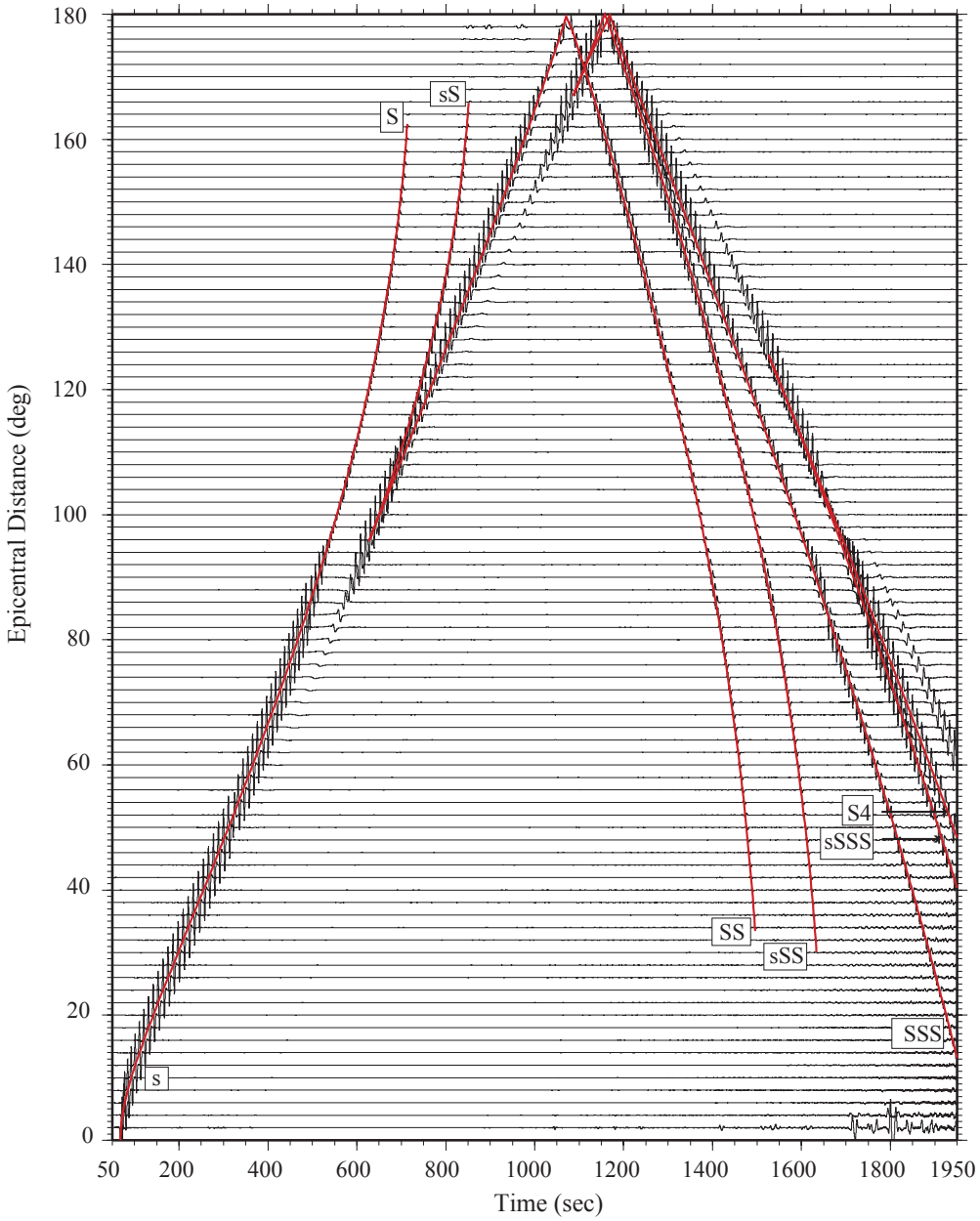


**Figure 4.4**. Synthetic seismograms of the VSM model generated by GEMINI. The source depth is 300 km. Phase arrivals are marked based on the travel times calculated by TauP

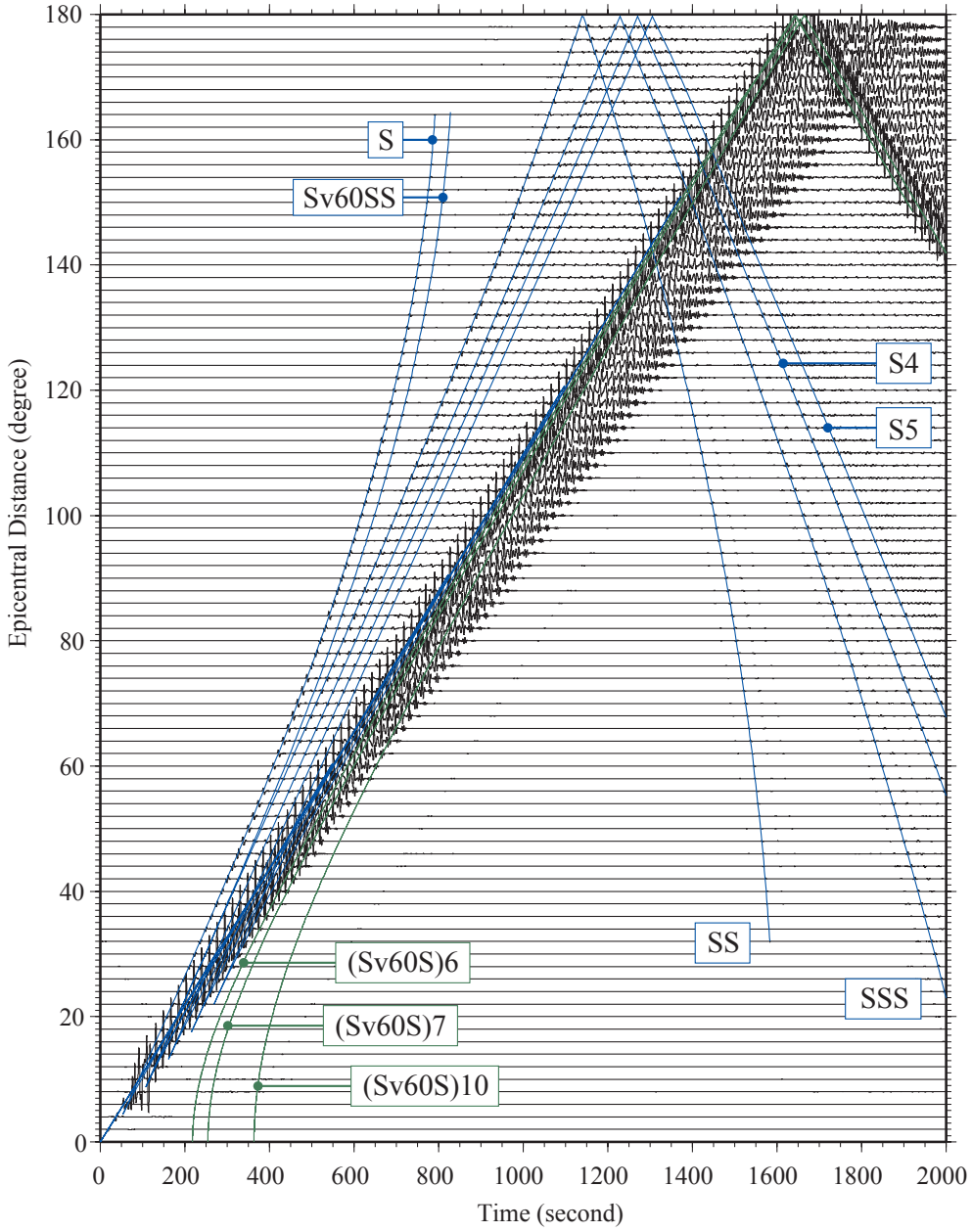


**Figure 4.5**. Synthetic seismograms of the SM model generated by GEMINI. The source depth is 0.1 km. Phase arrivals are marked based on the travel times calculated by TauP

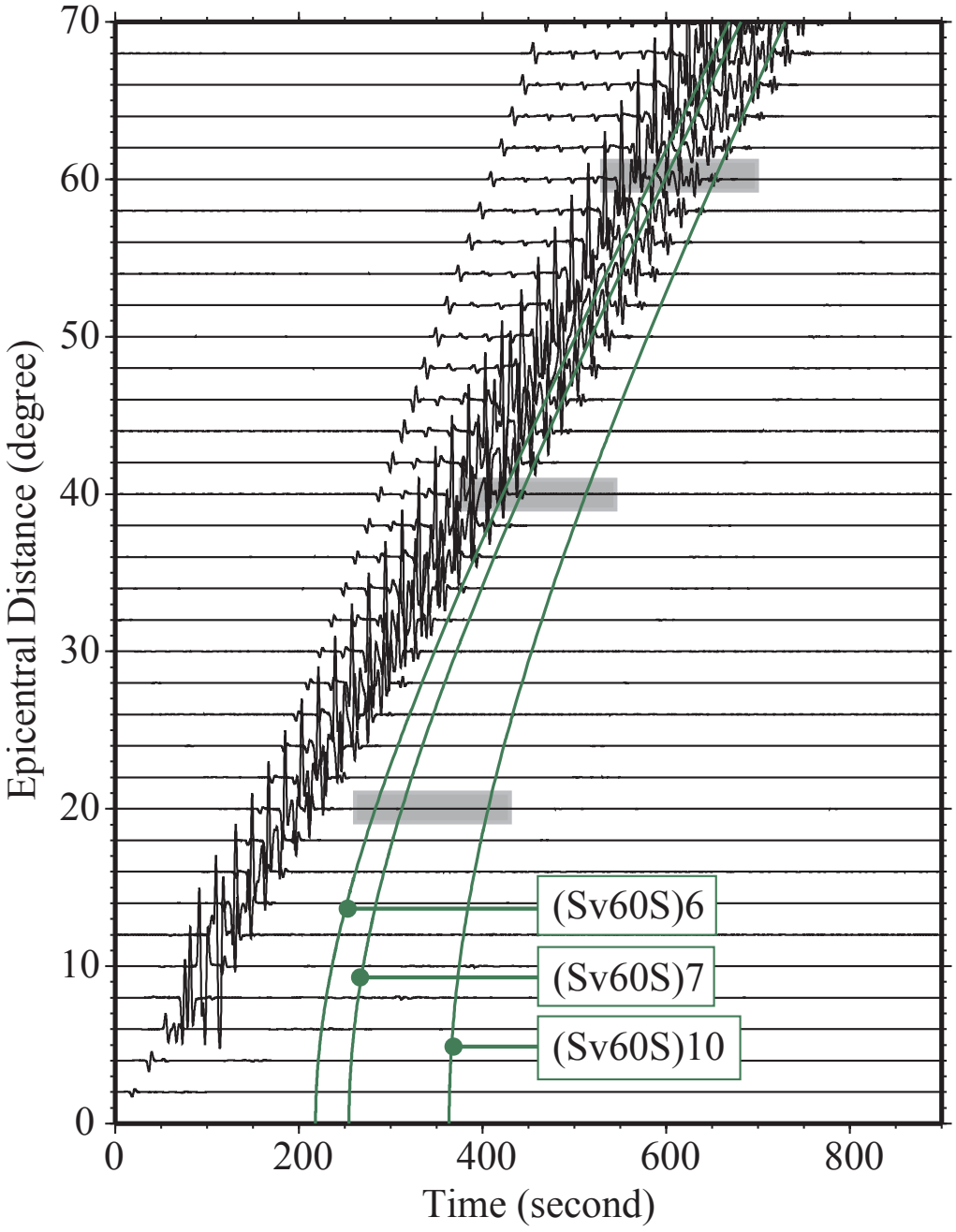


**Figure 4.6**. Synthetic seismograms of the SM model generated by GEMINI. The source depth is 0.1 km. Three multiple reflections in the crust (green lines) are shown as examples.

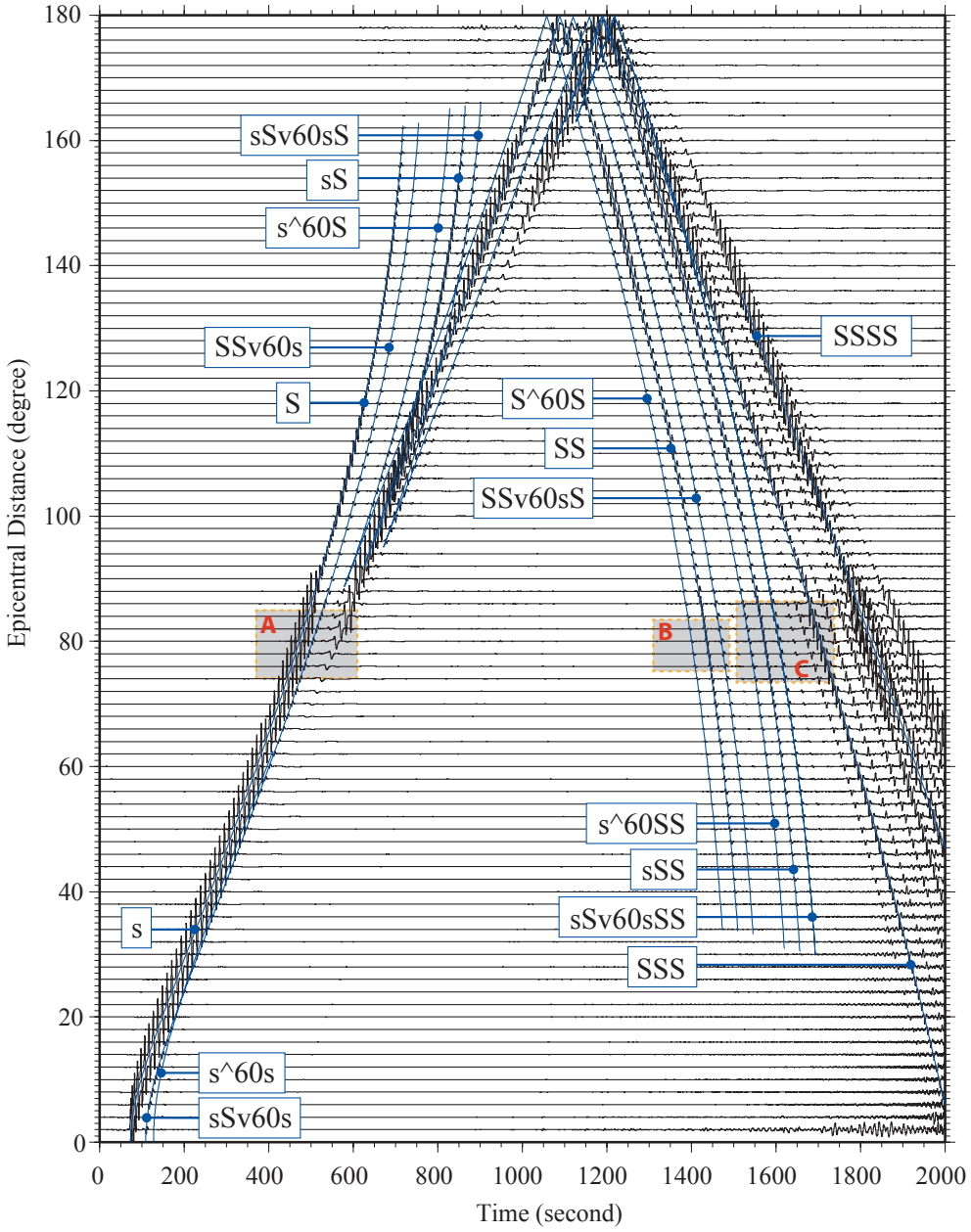


**Figure 4.7**. Synthetic seismograms of the SM model generated by GEMINI. The source depth is 300 km. The zoomed-in details of details of Section A, B, and C are shown in Figure 4.8, 4.9, and 4.10.

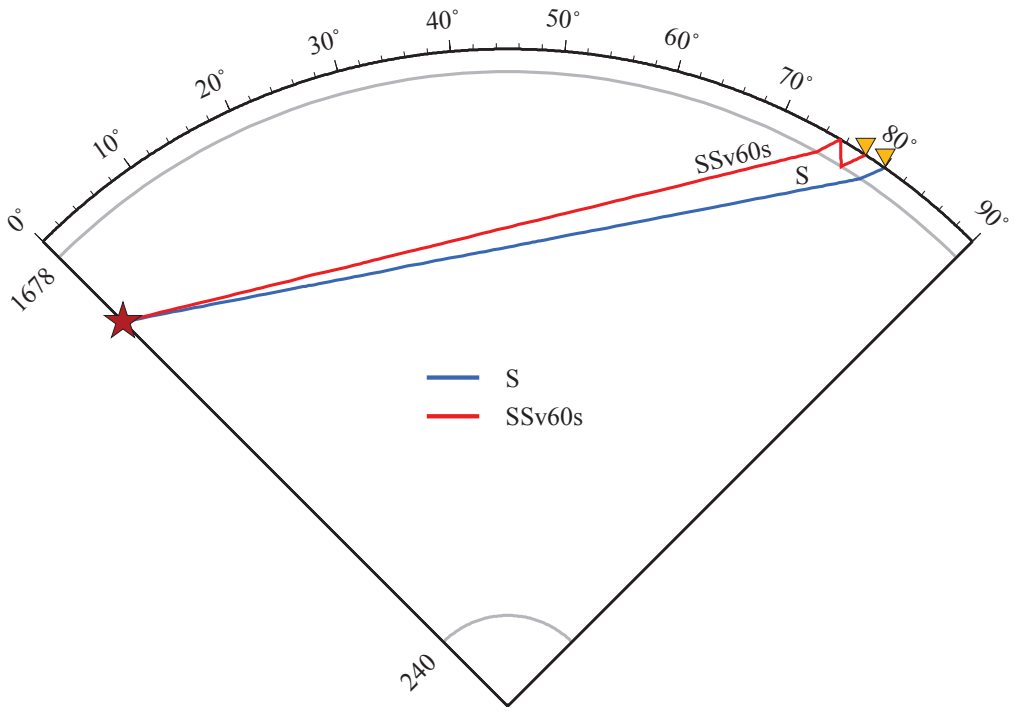


**Figure 4.8**. Ray path of seismic phases in Section A of Figure 4.7

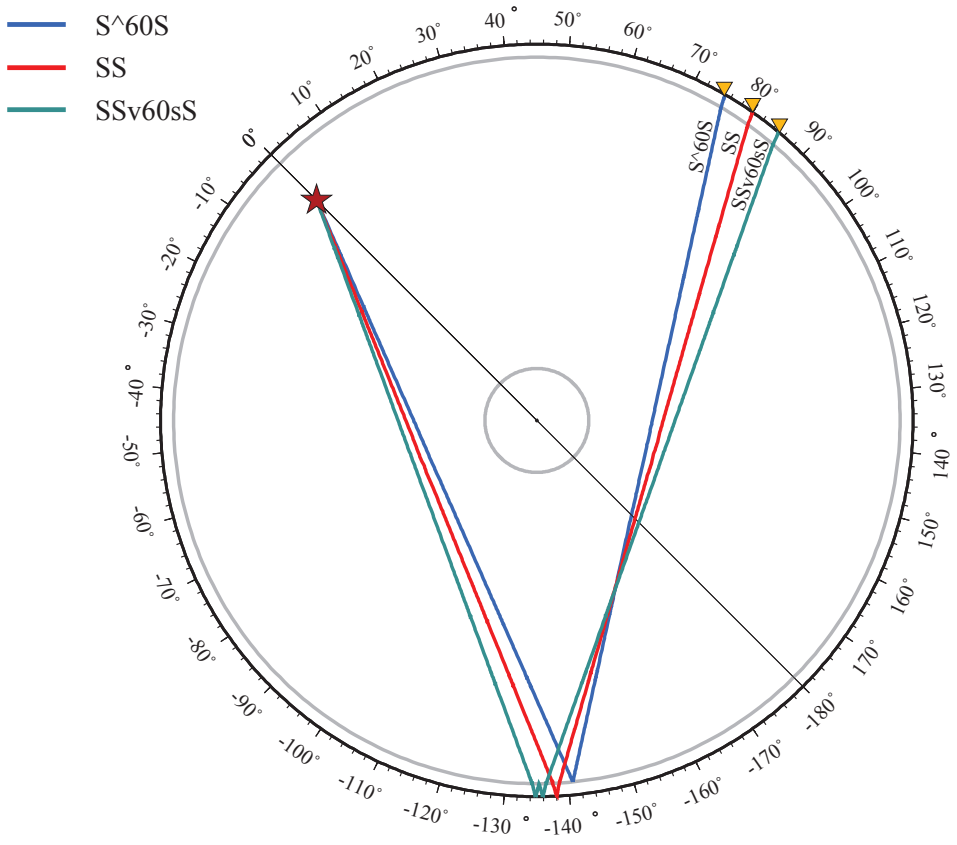


**Figure 4.9**. Ray path of seismic phases in Section B of Figure 4.7

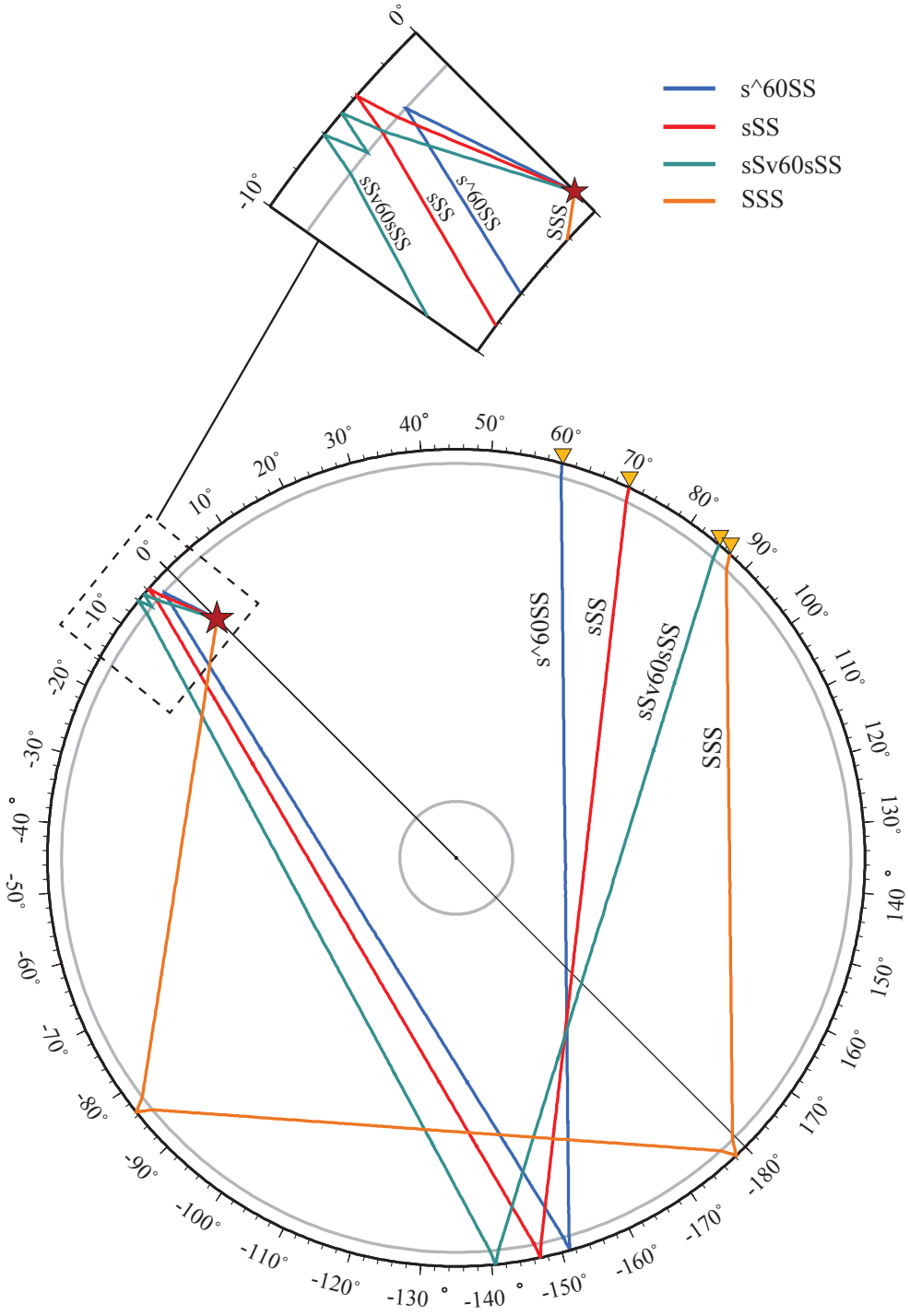


**Figure 4.10**. Ray path of seismic phases in Section C of Figure 4.7

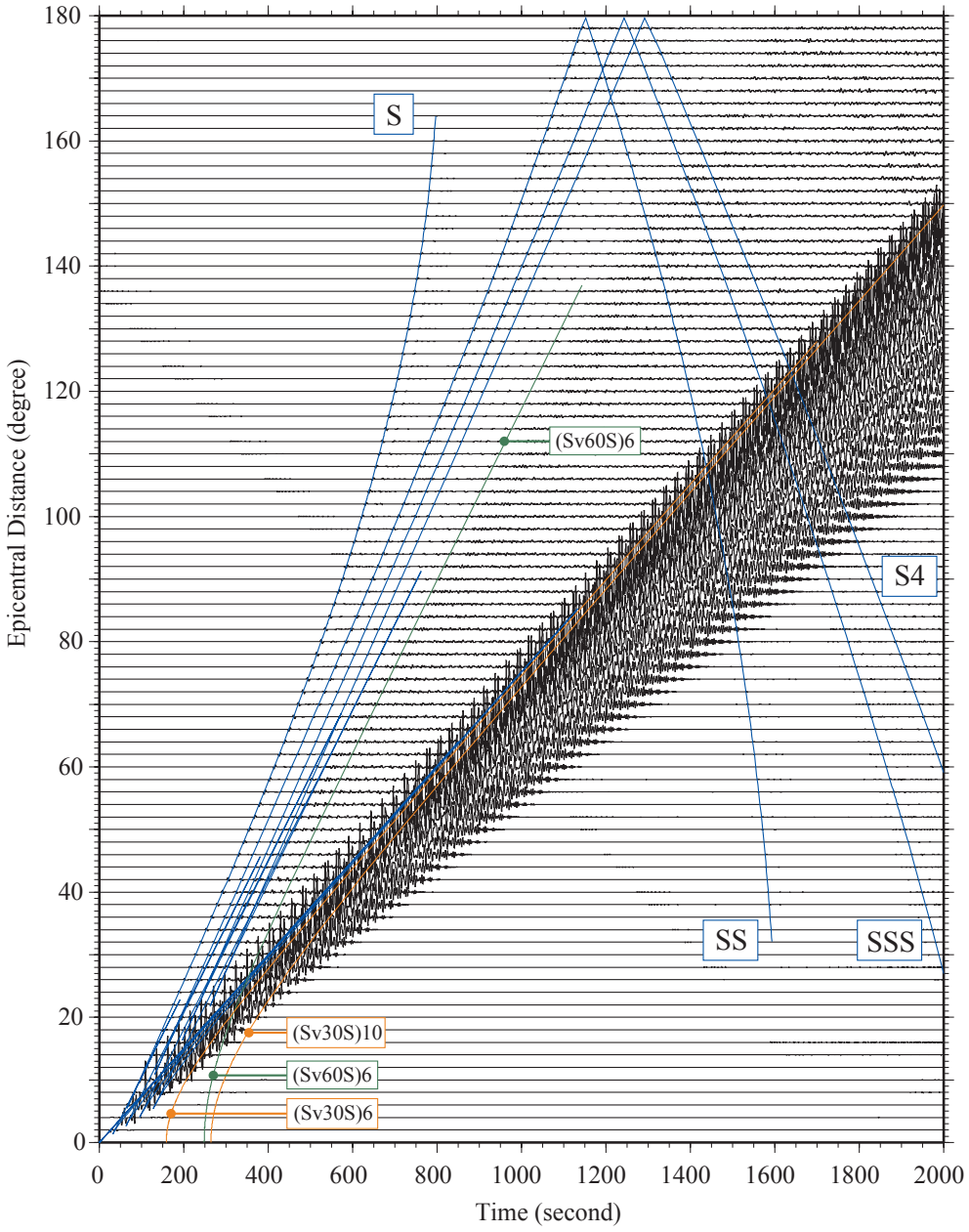


**Figure 4.11**. Synthetic seismograms of the 2LM model generated by GEMINI. The source depth is 0.1 km.

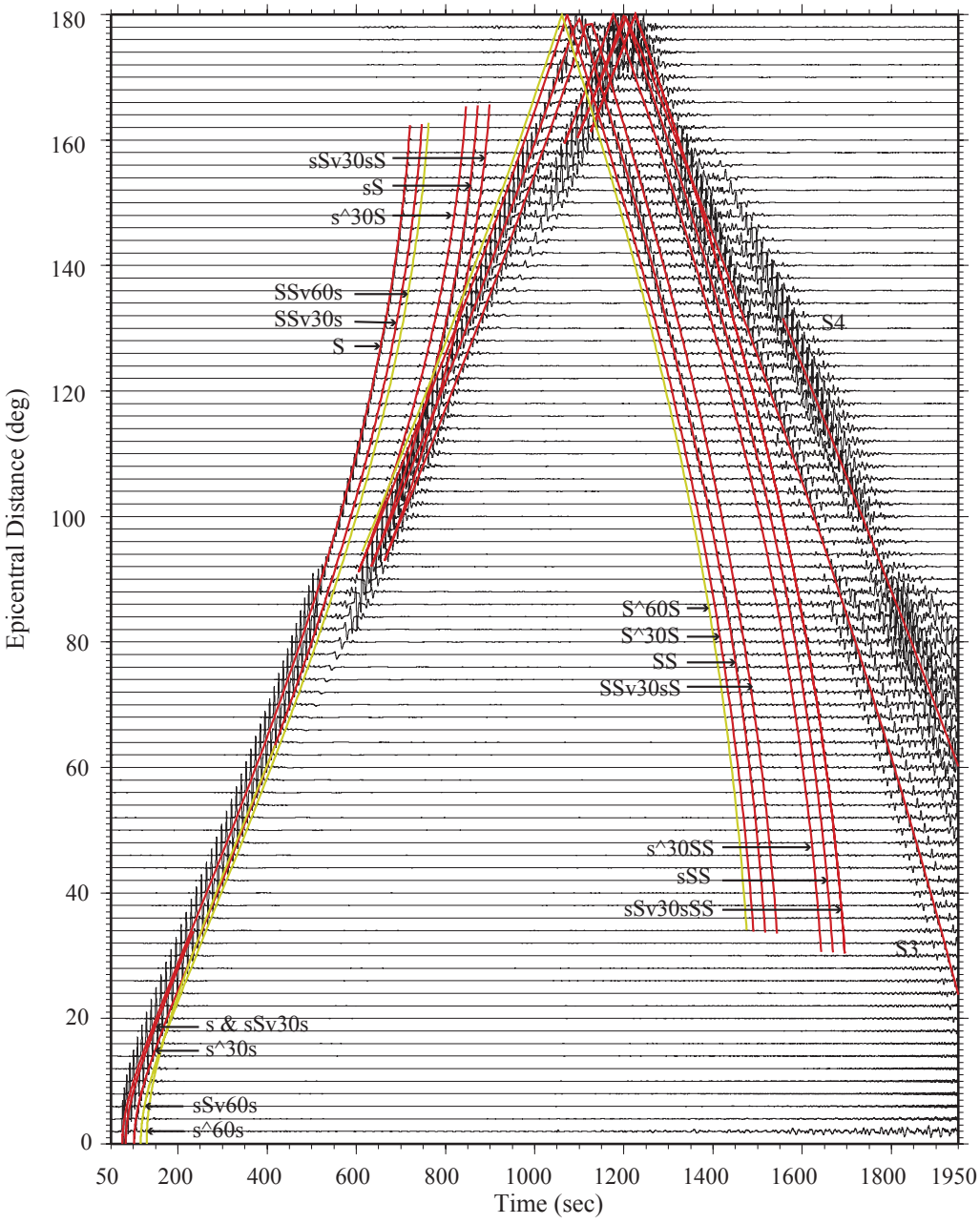


**Figure 4.12**. Synthetic seismograms of the 2LM model generated by GEMINI. The source depth is 300 km.

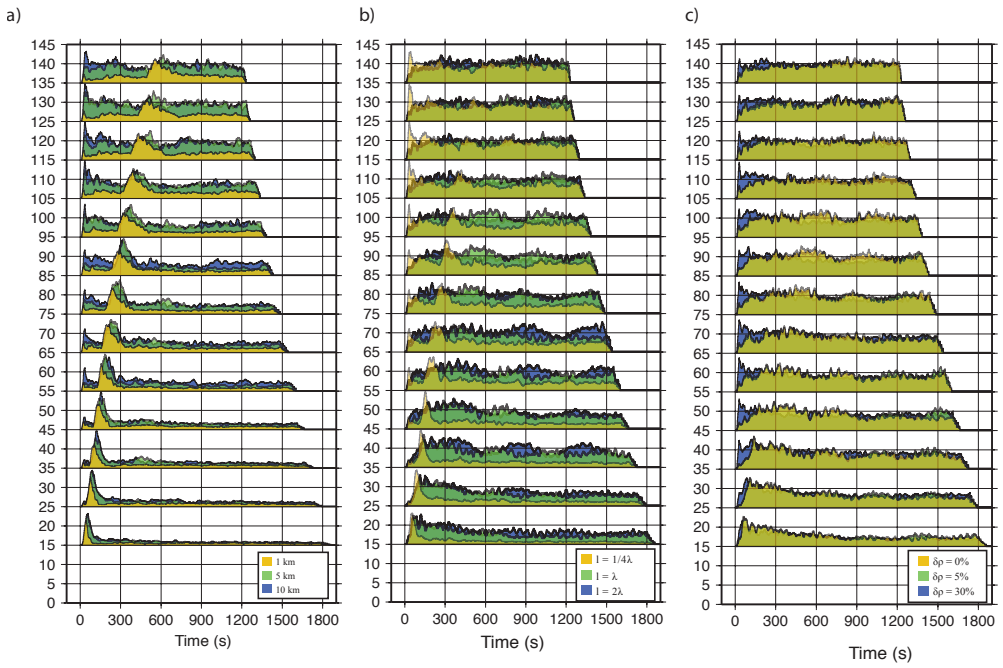


**Figure 4.13**. Smoothed envelope function of the synthetic moonquake seismograms for crust only scatterer models. The random velocity heterogeneities are generated by self-similar auto-correlation functions with 30% maximum velocity perturbations. The seismic source is located at 0.1 km depth. a) Comparison between the crustal scattering layers with different thickness (yellow: 1km, green: 5km, blue: 10km). b) The thickness of the scattering layer is fixed as 10 km. The auto-correlation length of the self-similar heterogeneities equal to 1.3 km (1/4 of the wavelength; yellow), 4.5 km (wavelength; green), or 9.1 km (twice of the wavelength; blue). c) The thickness of the scattering layer is fixed as 10 km and the auto-correlation length of the self-similar heterogeneities is fixed to 4.5 km. We apply 0% (yellow), 5% (green), or 30% (blue) density perturbations to the scattering layer.

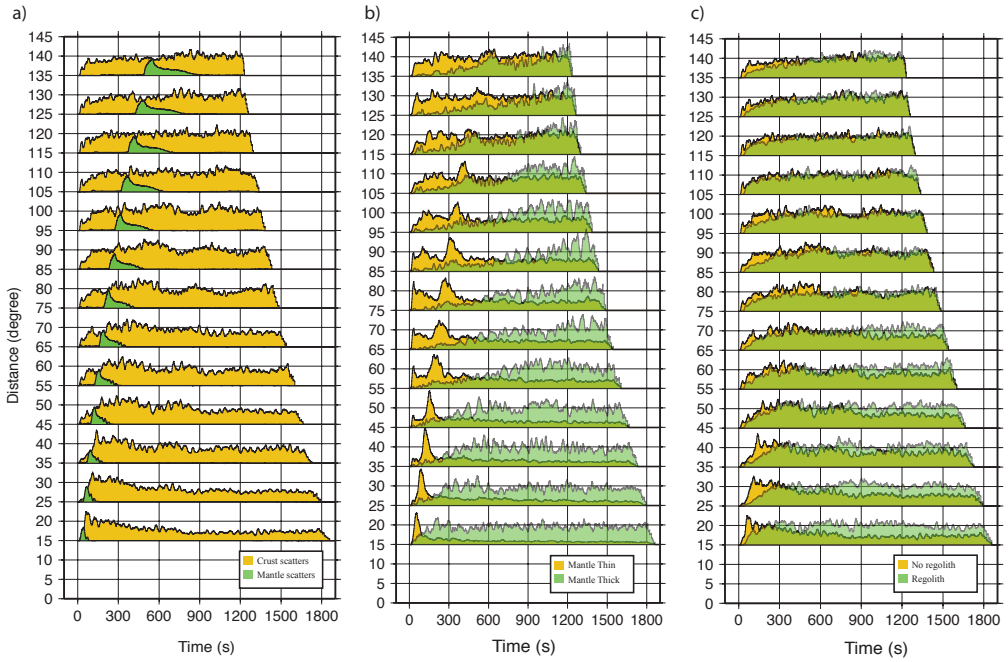


**Figure 4.14**. Smoothed envelope function of the synthetic moonquake seismograms for crust scattering layer and mantle scattering layer models. The random velocity heterogeneities are generated by self-similar auto-correlation functions with 30% maximum velocity perturbations. The seismic source is located at 0.1 km depth. a) Comparison between 10 km thick crust scattering layer (yellow) and 400 km thick mantle scattering layer located from 938 km to 1238 km depth (green). b) The thickness of the crust scattering layer is fixed as 10 km. We add another mantle scattering layer located from 938 km to 1238 km depth (yellow) or 600 km to 1728 km depth (green). c) The thickness of the scattering layer is fixed as 10 km and the auto-correlation length of the self-similar heterogeneities is fixed to 4.5 km. We show the comparison between the non-regolith crust model (yellow) with a model with 1-km thick regolith layer with 0.5 km/s $S$-wave velocity (green).

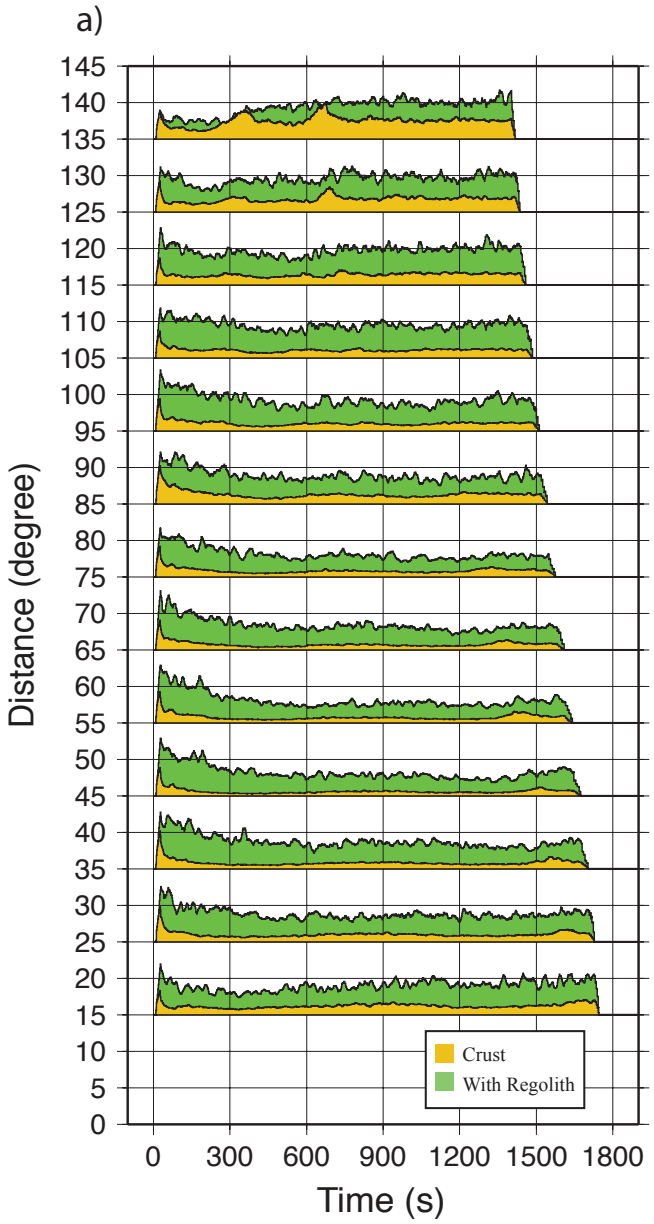


**Figure 4.15**. Smoothed envelope function of the synthetic moonquake seismograms for a source located at 900 km depth. The random velocity heterogeneities are generated by self-similar auto-correlation functions with 30% maximum velocity perturbations. The thickness of the scattering layer is fixed as 10 km located at the surface of the Moon. a) Comparison between the non-regolith crust model (yellow) with a model with 1 km thick regolith layer with 0.5 km/s $S$-wave velocity (green).

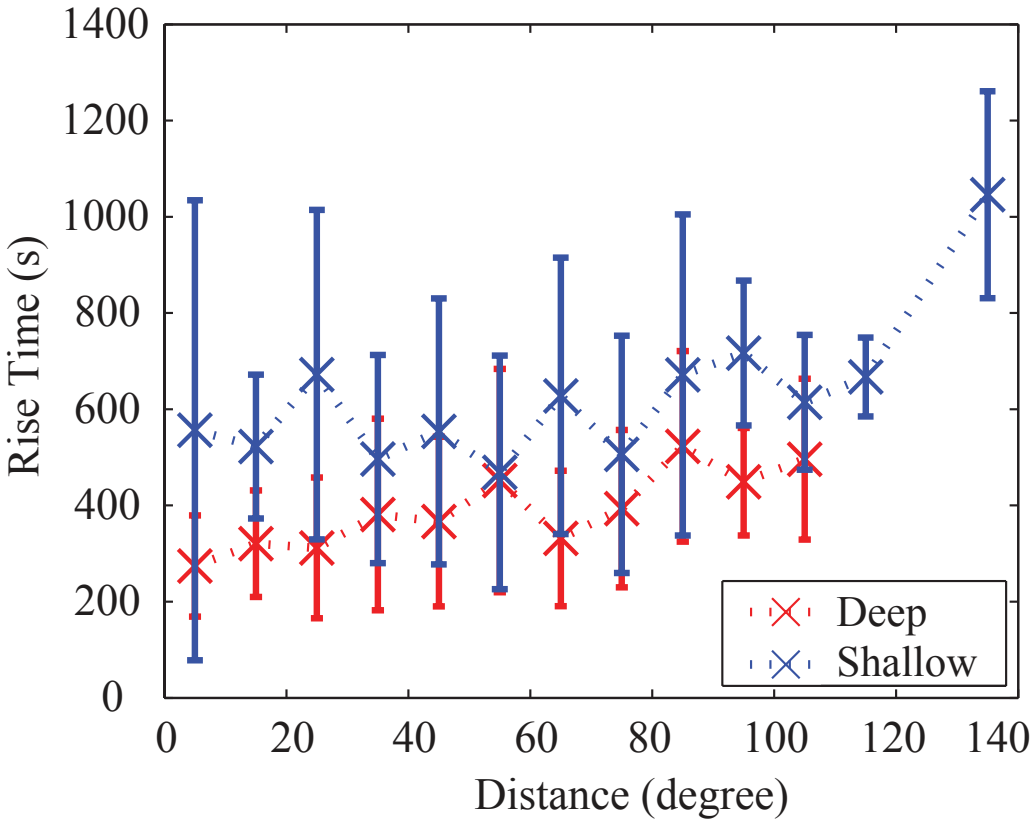


**Figure 4.16**. Risetime for shallow and deep moonquakes.

**Table 4.1** Reflection amplitudes of (Sv60S)6, (Sv60S)7, and (Sv60S)10

| Distance | (Sv60S)6 | (Sv60S)7 | (Sv60S)10 |
|---|---|---|---|
| 20° | $2.03\times10^{-8}$ | $-1.01\times10^{-9}$ | $4.58\times10^{-11}$ |
| 40° | Total reflection | Total reflection | $1.80\times10^{-3}$ |
| 60° | Total reflection | Total reflection | Total reflection |

# REFERENCES


Antonangeli, D., J. Siebert, C. M. Aracne, D. L. Farber, A. Bosak, M. Hoesch, M. Krisch, F. J. Ryerson, G. Fiquet, and J. Badro (2011), Spin crossover in ferropericlase at high pressure: A seismologically transparent transition?, *Science*, *331*(6013), 64–67.

Avants, M., T. Lay, S. A. Russell, and E. J. Garnero (2006), Shear velocity variation within the D" region beneath the central Pacific, *J. Geophys. Res.: Solid Earth*, *111*(B5).

Badro, J., G. Fiquet, F. Guyot, J.-P. Rueff, V. V. Struzhkin, G. Vankó, and G. Monaco (2003), Iron partitioning in Earth's mantle: toward a deep lower mantle discontinuity, *Science*, *300*(5620), 789–791.

Badro, J., J.-P. Rueff, G. Vankó, G. Monaco, G. Fiquet, and F. Guyot (2004), Electronic transitions in Perovskite: Possible nonconvecting layers in the lower mantle, *Science*, *305*(5682), 383–386.

Baig, A. M., and F. A. Dahlen (2004), Traveltime biases in random media and the S-wave discrepancy, *Geophys. J. Int.*, *158*(3), 922–938.

Bastow, I. D., G. W. Stuart, J.-M. Kendall, and C. J. Ebinger (2005), Upper-mantle seismic structure in a region of incipient continental breakup: northern Ethiopian rift, *Geophys. J. Int.*, *162*(2), 479–493.

Berteussen, K. A. (1976), The origin of slowness and azimuth anomalies at large arrays, *Bull. Seismol. Soc. Am.*, *66*(3), 719–741.

Bills, B. G., and A. J. Ferrari (1977), A lunar density model consistent with topographic, gravitational, librational, and seismic data, *J. Geophys. Res.*, *82*(8), 1306–1314.

Blanchette-Guertin, J.-F., C. L. Johnson, and J. F. Lawrence (2012), Investigation of scattering in lunar seismic coda, *J. Geophys. Res.*, *117*(E6), E06,003.

Blanchette-Guertin, J.-F., C. Johnson, and J. Lawrence (2015), Modeling seismic energy propagation in highly scattering environments, *J. Geophys. Res.: Planets*, *120*(3), 515–537.

Braña, L., and G. Helffrich (2004), A scattering region near the core-mantle boundary under the North Atlantic, *Geophys. J. Int.*, *158*(2), 625–636, doi:10.1111/j.1365-246X.2004.02306.x.

Brown, S. P., M. S. Thorne, L. Miyagi, and S. Rost (2015), A compositional origin to ultralow-velocity zones, *Geophys. Res. Lett.*, *42*(4), 1039–1045.

Bunge, H., and S. Grand (2000), Mesozoic plate-motion history below the northeast Pacific Ocean from seismic images of the subducted Farallon slab, *Nature*, *405*, 337–340.

Burdick, L. J., and C. Powell (1980), Apparent velocity measurements for the lower mantle from a wide aperture array, *J. Geophys. Res.: Solid Earth*, *85*(B7), 3845–3856.

Burdick, S., C. Li, V. Martynov, T. Cox, J. Eakins, T. Mulder, L. Astiz, F. L. Vernon, G. L. Pavlis, and R. D. van der Hilst (2008), Upper mantle heterogeneity beneath North America from travel time tomography with global and USArray Transportable Array Data, *Seismological Research Letters*, *79*(3), 384–392.

Burke, K., B. Steinberger, T. H. Torsvik, and M. A. Smethurst (2008), Plume generation zones at the margins of large low shear velocity provinces on the core-mantle boundary, *Earth Planet. Sci. Lett.*, *265*(1), 49–60.

Cammarano, F., H. Marquardt, S. Speziale, and P. J. Tackley (2010), Role of iron-spin transition in ferropericlase on seismic interpretation: A broad thermochemical transition in the mid mantle?, *Geophys. Res. Lett.*, *37*(3), L03,308.

Canup, R. M., and E. Asphaug (2001), Origin of the Moon in a giant impact near the end of the Earth's formation, *Nature*, *412*(6848), 708–712.

Caracas, R., D. Mainprice, and C. Thomas (2010), Is the spin transition in Fe2+-bearing perovskite visible in seismology?, *Geophys. Res. Lett.*, *37*(13).

Chinnery, M. A., and M. N. Toksöz (1967), P-wave velocities in the mantle below 700 km, *Bull. Seismol. Soc. Am.*, *57*(2), 199–226.

Cobden, L., and C. Thomas (2013), The origin of D" discontinuity reflections: a systematic study of seismic array data sets, *Geophys. J. Int.*, *194*(2), 1091–1118, doi:10.1093/gji/ggt152.

Conrad, C. P., C. Lithgow-Bertelloni, and K. E. Louden (2004), Iceland, the Farallon slab, and dynamic topography of the North Atlantic, *Geology*, *32*(3), 177, doi: 10.1130/G20137.1.

Cottaar, S., and B. Romanowicz (2012), An unsually large ULVZ at the base of the mantle near Hawaii, *Earth Planet. Sci. Lett.*, *355–356*, 213–222.

Crotwell, H. P., T. J. Owens, and J. Ritsema (1999), The TauP toolkit: flexible seismic travel-time and ray-path utilities, *Seismological Research Letters*, *70*(2), 154–160, doi:10.1785/gssrl.70.2.154.

Davaille, A., and J. Vatteville (2005), On the transient nature of mantle plumes, *Geophys. Res. Lett.*, *32*(14).

Davies, D. (1973), Seismology with large arrays, *Rep. Prog. Phys.*, *36*(10), 1233.

Dziewonski, A. M., and D. L. Anderson (1981), Preliminary reference Earth model, *Phys. Earth Planet. Inter.*, *25*(4), 297–356.

Frankel, A., and R. W. Clayton (1986), Finite difference simulations of seismic scattering: Implications for the propagation of short-period seismic waves in the crust and models of crustal heterogeneity, *J. Geophys. Res.: Solid Earth*, *91*(B6), 6465–6489.

French, S., and B. Romanowicz (2014), Whole-mantle radially anisotropic shear velocity structure from spectral-element waveform tomography, *Geophys. J. Int.*, *199*(3), 1303–1327.

French, S. W., and B. Romanowicz (2015), Broad plumes rooted at the base of the Earth's mantle beneath major hotspots, *Nature*, *525*(7567), 95–99.

Friederich, W., and J. Dalkolmo (1995), Complete synthetic seismograms for a spherically symmetric earth by a numerical computation of the Green's function in the frequency domain, *Geophys. J. Int.*, *122*(2), 537–550.

Fuchs, K., and G. Müller (1971), Computation of synthetic seismograms with the reflectivity method and comparison with observations, *Geophys. J. R. Astron. Soc.*, *23*(4), 417–433, doi:10.1111/j.1365-246X.1971.tb01834.x.

Gagnepain-Beyneix, J., P. Lognonnè, H. Chenet, D. Lombardi, and T. Spohn (2006), A seismic model of the lunar mantle and constraints on temperature and mineralogy, *Phys. Earth Planet. Inter.*, *159*(3-4), 140–166.

Garcia, R. F., J. Gagnepain-Beyneix, S. Chevrot, and P. Lognonné (2011), Very preliminary reference moon model, *Phys. Earth Planet. Inter.*, *188*(1), 96–113.

Garnero, E. J., M. M. Moore, T. Lay, and M. J. Fouch (2004), Isotropy or weak vertical transverse isotropy in D" beneath the Atlantic Ocean, *J. Geophys. Res.*, *109*, B08,308, doi:10.1029/2004JB003004.

Goins, N. R., A. M. Dainty, and M. N. Toksöz (1981), Lunar seismology: The internal structure of the Moon, *J. Geophys. Res.*, *86*(B6), 5061–5074.

Grand, S. P. (2002), Mantle shear-wave tomography and the fate of subducted slabs, *Philosophical transactions. Series A, Mathematical, physical, and engineering sciences*, *360*(1800), 2475–2491.

Grocholski, B., K. Catalli, S.-H. Shim, and V. Prakapenka (2012), Mineralogical effects on the detectability of the postperovskite boundary, *Proc. Natl. Acad. Sci. U. S. A.*, *109*(7), 2275–2279, doi:10.1073/pnas.1109204109.

Hao, C., and Z. Zheng (2010), P-Wave back-azimuth and slowness anomalies observed by an IMS seismic array LZDM, *Bull. Seismol. Soc. Am.*, *100*(2), 657–669.

He, Y., and L. Wen (2009), Structural features and shear-velocity structure of the "Pacific Anomaly", *J. Geophys. Res.: Solid Earth*, *114*(B2).

Hood, L. L., and J. H. Jones (1987), Geophysical constraints on lunar bulk composition and structure: A reassessment, *J. Geophys. Res.*, *92*(B4), E396.

Houard, S., and H.-C. Nataf (1992), Further evidence for the Lay discontinuity beneath northern Siberia and the North Atlantic from short-period P-waves recorded in France, *Phys. Earth Planet. Inter.*, *72*(3-4), 264–275, doi:10.1016/0031-9201(92)90206-B.

Huang, C., W. Leng, and Z. Wu (2015), Iron-spin transition controls structure and stability of LLSVPs in the lower mantle, *Earth Planet. Sci. Lett.*, *423*, 173–181.

Ikelle, L., S. Yung, and F. Daube (1993), 2-D random media with ellipsoidal autocorrelation functions, *Geophysics*, *58*(9), 1359–1372.

Jacobsen, S. B. (2003), How old is planet Earth?, *Science*, *300*(5625), 1513–1514.

Jahnke, G., M. S. Thorne, A. Cochard, and H. Igel (2008), Global SH-wave propagation using a parallel axisymmetric spherical finite-difference scheme: application to whole mantle scattering, *Geophys. J. Int.*, *173*(3), 815–826, doi:10.1111/j.1365-246X.2008.03744.x.

Jeffreys, H., and K. E. Bullen (1958), *Seismological tables*, Office of the British Association.

Johnson, L. R. (1969), Array measurements of P velocities in the lower mantle, *Bull. Seismol. Soc. Am.*, *59*(2), 973–1008.

Kendall, J.-M., and P. M. Shearer (1994), Lateral variations in D" thickness from long-period shear wave data, *J. Geophys. Res.*, *99*, 11,575–11,590.

Kennett, B. L. N., and E. R. Engdahl (1991), Traveltimes for global earthquake location and phase identification, *Geophys. J. Int.*, *105*(2), 429–465.

Kennett, B. L. N., E. R. Engdahl, and R. Buland (1995), Constraints on seismic velocities in the Earth from traveltimes, *Geophys. J. Int.*, *122*(1), 108–124.

Khan, A., and K. Mosegaard (2002), An inquiry into the lunar interior: A nonlinear inversion of the Apollo lunar seismic data, *J. Geophys. Res*, *107*(E6), 19–44.

Krüger, F., M. Weber, F. Scherbaum, and J. Schlittenhardt (1995), Evidence for normal and inhomogeneous lowermost mantle and core-mantle boundary structure under the Arctic and northern Canada, *Geophys. J. Int.*, *122*(122), 637–657.

Kulhánek, O., and R. Brown (1974), P-wave velocity anomalies in the earth's mantle from the Uppsala array observations, *Pure Appl. Geophys.*, *112*(3), 597–617.

Kuskov, O. L. (1997), Constitution of the Moon: 4. Composition of the mantle from seismic data, *Phys. Earth Planet. Inter.*, *102*(3-4), 239–257.

Kuskov, O. L., and V. A. Kronrod (1998), Constitution of the Moon:: 5. Constraints on composition, density, temperature, and radius of a core, *Phys. Earth Planet. Inter.*, *107*(4), 285–306.

Labrosse, S., J. W. Hernlund, and N. Coltice (2007), A crystallizing dense magma ocean at the base of the Earth's mantle, *Nature*, *450*(7171), 866–869.

Latham, G., M. Ewing, F. Press, and G. Sutton (1969), The apollo passive seismic experiment, *Science*, *165*(3890), 241–250.

Lay, T., and D. V. Helmberger (1983), The Shear-wave velocity gradient at the base of the mantle, *J. Geophys. Res.*, *88*(B10), 8160.

Lay, T., J. Hernlund, E. J. Garnero, and M. S. Thorne (2006), A post-perovskite lens and D" heat flux beneath the central pacific, *Science*, *314*(5803), 1272–1276.

Lee, C.-T. A., P. Luffi, T. Hoink, J. Li, R. Dasgupta, and J. Hernlund (2010), Upside-down differentiation and generation of a primordial lower mantle, *Nature*, *463*(7283), 930–933.

Li, C., R. D. van der Hilst, E. R. Engdahl, and S. Burdick (2008), A new global model for P wave speed variations in Earth's mantle, *Geochem., Geophys., Geosyst.*, *9*(5).

Li, L., J. P. Brodholt, S. Stackhouse, D. J. Weidner, M. Alfredsson, and G. D. Price (2005), Electronic spin state of ferric iron in Al-bearing perovskite in the lower mantle, *Geophys. Res. Lett.*, *32*(17).

Li, X., and B. Romanowicz (1996), Global mantle shear velocity model developed using nonlinear asymptotic coupling theory, *J. Geophys. Res.: Solid Earth*, *101*(B10), 22,245–22,272.

Lin, F.-C., M. P. Moschetti, and M. H. Ritzwoller (2008), Surface wave tomography of the western United States from ambient seismic noise: Rayleigh and Love wave phase velocity maps, *Geophys. J. Int.*, *173*(1), 281–298.

Lin, F.-C., V. C. Tsai, B. Schmandt, Z. Duputel, and Z. Zhan (2013), Extracting seismic core phases with array interferometry, *Geophys. Res. Lett.*, *40*(6), 1049–1053.

Lognonnè, P., J. Gagnepain-Beyneix, and H. Chenet (2003), A new seismic model of the Moon: implications for structure, thermal evolution and formation of the Moon, *Earth Planet. Sci. Lett.*, *211*(1-2), 27–44.

Lou, X., S. van der Lee, and S. Lloyd (2013), AIMBAT: A Python/Matplotlib tool for measuring teleseismic arrival times, *Seismological Research Letters*, *84*(1), 85–93.

Marquardt, H., S. Speziale, H. J. Reichmann, D. J. Frost, and F. R. Schilling (2009), Single-crystal elasticity of (Mg0.9Fe0.1)O to 81 GPa, *Earth Planet. Sci. Lett.*, *287*(3-4), 345–352.

Matzel, E., M. K. Sen, and S. P. Grand (1996), Evidence for anisotropy in the deep mantle beneath Alaska, *Geophys. Res. Lett.*, *23*(18), 2417–2420.

McNamara, A. K., E. J. Garnero, and S. Rost (2010), Tracking deep mantle reservoirs with ultra-low velocity zones, *Earth Planet. Sci. Lett.*, *299*(1-2), 1–9.

Mégnin, C., and B. Romanowicz (2000), The three-dimensional shear velocity structure of the mantle from the inversion of body, surface and higher-mode waveforms, *Geophys. J. Int.*, *143*(3), 709–728, doi:10.1046/j.1365-246X.2000.00298.x.

Meltzer, A. (2003), EarthScope: Opportunities and challenges for earth-science research and education, *The Leading Edge*, *22*(3), 268–271.

Mercier, J.-P., M. G. Bostock, P. Audet, J. B. Gaherty, E. J. Garnero, and J. Revenaugh (2008), The teleseismic signature of fossil subduction: Northwestern Canada, *J. Geophys. Res.: Solid Earth*, *113*(B4).

Miyagi, L., W. Kanitpanyacharoen, P. Kaercher, K. K. M. Lee, and H.-R. Wenk (2010), Slip systems in MgSiO3 post-perovskite: Implications for D" anisotropy, *Science*, *329*(5999), 1639–1641, doi:10.1126/science.1192465.

Moore, M. M., E. J. Garnero, T. Lay, and Q. Williams (2004), Shear wave splitting and waveform complexity for lowermost mantle structures with low-velocity lamellae and transverse isotropy, *J. Geophys. Res.*, *109*, B02,319, doi:10.1029/2003JB002546.

Muirhead, K. J., and A. L. Hales (1980), Evidence for P wave velocity discontinuities at depths greater than 650 km in the mantle, *Phys. Earth Planet. Inter.*, *23*(4), 304–313.

Murakami, M., K. Hirose, K. Kawamura, N. Sata, and Y. Ohishi (2004), Post-perovskite phase transition in MgSiO3, *Science*, *304*(5672), 855–858, doi:10.1126/science.1095932.

Nakamura, Y. (1983), Seismic velocity structure of the lunar mantle, *J. Geophys. Res.*, *88*(B1), 677–686.

Nakamura, Y. (2003), New identification of deep moonquakes in the Apollo lunar seismic data, *Phys. Earth Planet. Inter.*, *139*(3), 197–205.

Nakamura, Y. (2005), Farside deep moonquakes and deep interior of the Moon, *J. Geophys. Res.*, *110*(E1), E01,001.

Nakamura, Y., F. K. Duennebier, G. V. Latham, and H. J. Dorman (1976), Structure of the lunar mantle, *J. Geophys. Res.*, *81*(26), 4818–4824.

Nakamura, Y., G. V. Latham, and H. J. Dorman (1982), Apollo lunar seismic experimentâĂŤfinal summary, *J. Geophys. Res.: Solid Earth*, *87*(S01).

Oganov, A. R., and S. Ono (2004), Theoretical and experimental evidence for a post-perovskite phase of MgSiO3 in Earth's D" layer, *Nature*, *430*(6998), 445–448, doi:10.1038/nature02701.

Poli, P., C. Thomas, M. Campillo, and H. A. Pedersen (2015), Imaging the D" reflector with noise correlations, *Geophys. Res. Lett.*, *42*(1), 60–65.

Rawlinson, N., and B. L. N. Kennett (2004), Rapid estimation of relative and absolute delay times across a network by adaptive stacking, *Geophys. J. Int.*, *157*(1), 332–340.

Ritsema, J., A. Deuss, H. J. van Heijst, and J. H. Woodhouse (2011), S40RTS: a degree-40 shear-velocity model for the mantle from new Rayleigh wave dispersion, teleseismic traveltime and normal-mode splitting function measurements, *Geophys. J. Int.*, *184*(3), 1223–1236, doi:10.1111/j.1365-246X.2010.04884.x.

Rost, S., and C. Thomas (2009), Improving seismic resolution through array processing techniques, *Surveys in geophysics*, *30*(4-5), 271–299, doi:10.1007/s10712-009-9070-6.

Rost, S., E. J. Garnero, Q. Williams, and M. Manga (2005), Seismological constraints on a possible plume root at the core-mantle boundary, *Nature*, *435*(7042), 666–669.

Rost, S., E. J. Garnero, M. S. Thorne, and A. R. Hutko (2010), On the absence of an ultralow-velocity zone in the North Pacific, *J. Geophys. Res.: Solid Earth*, *115*(B4).

Sato, H., M. C. Fehler, and T. Maeda (2012), *Seismic wave propagation and scattering in the heterogeneous earth*, vol. 496, Springer.

Schmandt, B. (2012), Mantle transition zone shear velocity gradients beneath USArray, *Earth Planet. Sci. Lett.*, *355–356*, 119–130.

Schmandt, B., and E. Humphreys (2010), Complex subduction and small-scale convection revealed by body-wave tomography of the western United States upper mantle, *Earth Planet. Sci. Lett.*, *297*(3-4), 435–445.

Schmandt, B., and F.-C. Lin (2014), P and S wave tomography of the mantle beneath the United States, *Geophys. Res. Lett.*, *41*(18), 6342–6349.

Schubert, G., G. Masters, P. Olson, and P. Tackley (2004), Superplumes or plume clusters?, *Phys. Earth Planet. Inter.*, *146*(1âĂŞ2), 147–162.

Shearer, P. M., and P. S. Earle (2004), The global short-period wavefield modelled with a Monte Carlo seismic phonon method, *Geophys. J. Int.*, *158*(3), 1103–1117.

Simmons, N. A., A. M. Forte, L. Boschi, and S. P. Grand (2010), GyPSuM: A joint tomographic model of mantle density and seismic wave speeds, *J. Geophys. Res.: Solid Earth*, *115*, B12,310, doi:10.1029/2010JB007631.

Simmons, N. A., S. C. Myers, G. Johannesson, and E. Matzel (2012), LLNL-G3Dv3: Global P wave tomography model for improved regional and teleseismic travel time prediction, *J. Geophys. Res.: Solid Earth*, *117*(B10).

Simmons, N. A., S. C. Myers, G. Johannesson, E. Matzel, and S. P. Grand (2015), Evidence for long-lived subduction of an ancient tectonic plate beneath the southern Indian Ocean, *Geophys. Res. Lett.*, *42*(21), 9270–9278.

Solomatov, V. S. (2007), Magma oceans and primordial mantle differentiation, *Treatise on geophysics*, *9*, 91–120.

Steck, L. K., and W. A. Prothero (1993), Observations of direct P-wave slowness and azimuth anomalies for teleseisms recorded in Long Valley caldera, California, *Bull. Seismol. Soc. Am.*, *83*(5), 1391–1419.

Su, W. J., and A. M. Dziewonski (1997), Simultaneous inversion for 3-D variations in shear and bulk velocity in the mantle, *Phys. Earth Planet. Inter.*, *100*(1), 135–156.

Su, W. J., R. L. Woodward, and A. M. Dziewonski (1994), Degree 12 model of shear velocity heterogeneity in the mantle, *J. Geophys. Res.: Solid Earth*, *99*(B4), 6945–6980.

Sun, D., and D. Helmberger (2011), Upper-mantle structures beneath USArray derived from waveform complexity, *Geophys. J. Int.*, *184*(1), 416–438.

Sun, D., D. Helmberger, M. S. Miller, and J. M. Jackson (2016), Major disruption of d" beneath alaska, *J. Geophys. Res.: Solid Earth*.

Tan, E., and M. Gurnis (2005), Metastable superplumes and mantle compressibility, *Geophys. Res. Lett.*, *32*(20).

Tauzin, B., R. D. van der Hilst, G. Wittlinger, and Y. Ricard (2013), Multiple transition zone seismic discontinuities and low velocity layers below western United States, *J. Geophys. Res.: Solid Earth*, *118*(5), 2307–2322.

Thomas, C., J. Wookey, J. Brodholt, and T. Fieseler (2011), Anisotropy as cause for polarity reversals of D" reflections, *Earth Planet. Sci. Lett.*, *307*(3-4), 369–376, doi:http://dx.doi.org/10.1016/j.epsl.2011.05.011.

Thorne, M. S., E. J. Garnero, G. Jahnke, H. Igel, and A. K. McNamara (2013), Mega ultra low velocity zone and mantle flow, *Earth Planet. Sci. Lett.*, *364*, 59–67.

Tibuleac, I. M., and E. Herrin (1999), Lower mantle lateral heterogeneity beneath the Caribbean Sea, *Science*, *285*(5434), 1711–1715.

Toksöz, M. N., A. M. Dainty, S. C. Solomon, and K. R. Anderson (1974), Structure of the Moon, *Rev. Geophys.*, *12*(4), 539–567.

Tonks, W. B., and H. J. Melosh (1993), Magma ocean formation due to giant impacts, *J. Geophys. Res.: Planets*, *98*(E3), 5319–5333.

Touboul, M., T. Kleine, B. Bourdon, H. Palme, and R. Wieler (2007), Late formation and prolonged differentiation of the Moon inferred from W isotopes in lunar metals, *Nature*, *450*(7173), 1206–1209.

Valenzuela, R. W., M. E. Wysession, M. O. Neustadt, and J. L. Butler (2000), Lateral variations at the base of the mantle from profiles of digital Sdiff data, *J. Geophys. Res.: Solid Earth*, *105*(B3), 6201–6220.

Ventosa, S., and B. Romanowicz (2015), Extraction of weak PcP phases using the slant-stacklet transform âĂŞ II: constraints on lateral variations of structure near the coreâĂŞmantle boundary, *Geophys. J. Int.*, *203*(2), 1227–1245.

Wallace, M., and C. Thomas (2005), Investigating D" structure beneath the North Atlantic, *Phys. Earth Planet. Inter.*, *151*(1-2), 115–127, doi:10.1016/j.pepi.2005.02.001.

Wang, P., M. V. De Hoop, and R. D. Van Der Hilst (2008), Imaging the lowermost mantle (D") and the core-mantle boundary with SKKS coda waves, *Geophys. J. Int.*, *175*(1), 103–115.

Warren, P. H. (1985), The magma ocean concept and lunar evolution, *Annu. Rev. Earth Planet. Sci.*, *13*, 201–240.

Weber, M., and J. P. Davis (1990), Evidence of a laterally variable lower mantle structure from P- and S-waves, *Geophys. J. Int.*, *102*(1), 231–255.

Weber, M., and M. Körnig (1992), A search for anomalies in the lowermost mantle using seismic bulletins, *Phys. Earth Planet. Inter.*, *73*(1-2), 1–28, doi:10.1016/0031-9201(92)90104-4.

Weber, R. C., P. Y. Lin, E. J. Garnero, Q. Williams, and P. Lognonne (2011), Seismic detection of the lunar core, *Science*, *331*(6015), 309.

Whittaker, S., M. S. Thorne, N. C. Schmerr, and L. Miyagi (2016), Seismic array constraints on the D" discontinuity beneath Central America, *J. Geophys. Res.: Solid Earth*, *121*(1), 152–169.

Wicks, J. K., J. M. Jackson, and W. Sturhahn (2010), Very low sound velocities in iron-rich (Mg, Fe) O: Implications for the core-mantle boundary region, *Geophys. Res. Lett.*, *37*(15).

Williams, Q., J. Revenaugh, and E. Garnero (1998), A correlation between ultra-Low basal velocities in the mantle and hot spots, *Science*, *281*(5376), 546–549.

Wood, J. A. (1975), Lunar petrogenesis in a well-stirred magma ocean, in *Lunar and Planetary Science Conference Proceedings*, vol. 6, pp. 1087–1102.

Wysession, M. E., T. Lay, J. Revenaugh, Q. Williams, E. J. Garnero, R. Jeanloz, and L. H. Kellogg (1998), The D" Discontinuity and its implications, in *The Core-Mantle Boundary Region*, edited by M. Gurnis, M. E. Wysession, E. Knittle, and B. A. Buffett, pp. 273–297, American Geophysical Union, Washington, D.C.

Xu, Y., and K. D. Koper (2009), Detection of a ULVZ at the base of the mantle beneath the northwest Pacific, *Geophys. Res. Lett.*, *36*(17).

Yang, J., X. Tong, J.-F. Lin, T. Okuchi, and N. Tomioka (2015), Elasticity of ferropericlase across the spin crossover in the Earth's lower mantle, *Sci. Rep.*, *5*, 17,188.

Yao, Y. (2013), Evaluation of one-dimensional seismic models of the lunar interior, Master's thesis, The University of Utah, Salt Lake City, Utah.

Yao, Y., S. Whittaker, and M. S. Thorne (2015), D" discontinuity structure beneath the North Atlantic from Scd observations, *Geophys. Res. Lett.*, p. 2015GL063989.

Yee, T.-G., J. Rhie, and H. Tkalčić (2014), Regionally heterogeneous uppermost inner core observed with Hi-net array, *J. Geophys. Res.: Solid Earth*, *119*(10), 7823–7845.

Young, C., and T. Lay (1990), Multiple phase analysis of the shear velocity structure in the D" region beneath Alaska, *J. Geophys. Res.*, *95*(B11), 17,385–17,402.

Young, E. D., I. E. Kohl, P. H. Warren, D. C. Rubie, S. A. Jacobson, and A. Morbidelli (2016), Oxygen isotopic evidence for vigorous mixing during the moon-forming giant impact, *Science*, *351*(6272), 493–496.